Study on Evaluation of Stress-Strain Relationship of Strain-Hardening Cementitious Composite

Graduate School of Science and Technology
Degree Programs in Systems and Information Engineering
University of Tsukuba

March 2026

ZHANG HANG

Abstract

Fiber-reinforced cementitious composites (FRCCs) represent a class of advanced cement-based materials designed to overcome the brittle nature of conventional concrete by introducing distributed microcracking and improved post-cracking ductility. Among these, strain-hardening cementitious composites (SHCCs) have attracted significant research attention due to their ability to exhibit pseudo-ductile behavior under tension, characterized by multiple fine cracks and high fracture energy absorption capacity. This unique deformation mechanism arises from the interaction between fibers and the surrounding cementitious matrix, which is governed by factors such as fiber orientation, dispersion, and interfacial bond characteristics. Consequently, a comprehensive understanding of these mechanisms is essential for the reliable design and performance prediction of SHCC and related FRCC systems.

Despite considerable progress in the past three decades, several key challenges remain in accurately evaluating and modeling the tensile and flexural behavior of SHCCs. The uniaxial tension test, although the most fundamental method for determining tensile properties, is often affected by variations in such as specimen geometry, boundary conditions, and loading rates, leading to difficulties in standardization and reproducibility. Moreover, fiber orientation—strongly influenced by casting conditions, placing thickness, and rheological behavior of the fresh matrix—plays a crucial role in determining the mechanical response and bridging efficiency of SHCCs. The lack of quantitative models that incorporate both fiber dimension and orientation effects continue to limit the predictive capability of existing constitutive frameworks.

To address these issues, the present study systematically investigates the mechanisms governing fiber orientation, crack characteristics, and stress transfer in SHCCs through a combination of experimental visualization simulation, bending tests, image-based statistical analysis, and analytical modeling. The final objective is to propose a generalized tensile stress–strain constitutive model that integrates the influence of fiber dimension, orientation, and bond mechanics, thereby providing a more reliable analytical tool for the design of high-performance SHCCs.

Chapter 1 Introduction

To begin with, **Chapter 1** provides a detailed introduction to the research background of this study. It also presents a systematic review of previous studies on uniaxial tension test (UTT) methods for FRCCs, with particular emphasis on SHCCs. A statistical analysis is conducted to examine the key factors influencing the UTT, such as specimen geometry, loading rate, and boundary conditions. Although the UTT is recognized as the most fundamental approach for accurately determining the tensile properties of SHCC, this chapter highlights the existing challenges that hinder its standardized application. Furthermore, the research concerning the tensile stress–strain behavior of SHCC and the bridging law of PVA-FRCC are presented as review. Finally, the necessity and objectives of the present study, as well as the overall research framework, are clarified.

Chapter 2 Influence of placing thickness on fiber orientation and bridging law of FRCC

Chapter 2 provides a detailed investigation into the influence of different placing thicknesses on fiber orientation within FRCC. This chapter conduct a visualization simulation experiment which employed black-colored nylon fiber and transparent water glass solution which has high viscosity to simulate the dispersion in FRCC. Three different placing thicknesses, which are defined as the thickness of each layer of target cementitious matrix in the height direction, are adopted in this experiment.

Image-processes are subsequently utilized to statistically analyze the fiber orientation and dispersion within specimens cast under varying thickness conditions. The results show a smaller placing thickness leads to a greater fiber orientation intensity, which is one of the significant factors on the bridging law of FRCC. From the calculation results of the bridging law, a smaller placing thickness leads to a higher tensile stress due to the centralization of the fiber angles. Based on the simplified tri-linear stress-strain model of bridging law, section analysis is conducted to give strong evidence on that a smaller placing thickness can effectively improve the flexural performance of FRCC.

Chapter 3 Flexural characteristics of functionally layered FRCC with PVA fibers

This chapter investigates the flexural behavior and constitutive modeling of a functionally layered fiber-reinforced cementitious composite (FL-FRCC) reinforced with polyvinyl alcohol (PVA) fibers. This study aims to elucidate the influence of two-dimensional fiber orientation, induced through functional layering, on the mechanical response of FRCCs, and to develop a predictive constitutive model capable of describing tensile behavior across a broad range of fiber orientation intensities. A modified bridging-law-based tensile stress–strain model is formulated to extend the applicability of former approaches to composites exhibiting highly 2D-oriented fiber distributions.

Experimental validation is conducted through four-point bending tests on both functionally layered and homogeneous FRCC (Hmg-FRCC) specimens containing identical fiber volume fractions. The FL-FRCC specimens are fabricated by stacking multiple thin layers, each with a smaller thickness than the fiber length, thereby promoting preferential 2D in-plane fiber alignment and infinite fiber orientation in thickness direction. Sectional analyses, employing the proposed bridging law model in conjunction with Popovics' compressive strength model, are performed to simulate bending moment–curvature relationships and to assess model accuracy.

Experimental results demonstrate that the FL-FRCC specimens exhibit nearly twice the maximum bending capacity of Hmg-FRCC, accompanied by higher energy absorption up to a curvature of 0.5 m^{-1}. And the post-peak response of the FL-FRCC shows a steeper decline phase after reaching the maximum bending moment compared to that of Hmg-FRCC specimens.

The findings confirm that FL-FRCC effectively enhances fiber orientation and mechanical performance without increasing fiber volume fraction. The proposed constitutive model provides a robust analytical framework for characterizing and predicting the tensile and flexural behaviors of FL-FRCC, offering theoretical and practical contributions to the design of high-performance FRCC and structural systems.

Chapter 4 Flexural and crack characteristics of thin plate SHCC with PVA fibers

Chapter 4 investigates the crack characteristics of SHCC with PVA fibers of different dimensions through four-point bending tests on plate-shaped specimens. Image-processing techniques are employed to statistically analyze the crack width and spacing distributions, which are subsequently fitted using probabilistic models.

Previous studies on single-crack bridging behavior have typically used PVA fibers with a 2% volume fraction and a diameter of 100 μm. At this fiber content, the specimens generally exhibit strain-softening behavior. To achieve strain-hardening behavior, in addition to the commonly used PVA fibers with 2% volume fraction and diameters of 27 μm and 40 μm, the present study employed PVA fibers with a 3% volume fraction and a diameter of 100 μm. Plate-shaped specimens with dimensions of 400 mm × 100 mm × 10 mm are successfully fabricated while maintaining sufficient fluidity of the fresh mixture. Ten specimens are prepared for each fiber type.

During testing, a digital camera is positioned in front of the universal testing machine, with a mirror placed beneath the specimen to capture the crack development on the tensile surface through reflection. To ensure consistent image analysis and account for deformation during loading, reference lines are drawn at 25 mm and 50 mm from the lower edge of each specimen. Crack width and spacing along these lines are statistically analyzed using image-processing techniques.

The experimental results reveal that all three types of PVA-FRCC plates exhibited multiple fine cracks, with the majority of crack widths remaining below 0.5 mm. The number of cracks in PVA027-2% and PVA040-2% specimens is significantly higher, and the average crack spacing smaller than in PVA100-3% specimens. All specimens ultimately fail when one crack propagate through the section.

The load–mid span deflection responses indicate that for all specimen types, flexural stiffness decreases after initial cracking, followed by a subsequent load increase with increasing mid-span deflection, demonstrating strain-hardening potential. After reaching the peak load, the load gradually decreases with continued deflection; however, PVA100-3% specimens exhibit a mild reduction, maintaining load capacity until final failure.

Statistical analysis of image-processing data show that PVA040-2% specimens had a slightly greater number of cracks than PVA027-2% specimens—nearly double that of PVA100-3% specimens. In contrast, the average crack width and spacing of PVA040-2% specimens are marginally larger than those of PVA027-2% specimens but much smaller than those of PVA100-3% specimens. Both normal and log-normal probability functions are employed to fit the crack width and crack spacing data. The fitting results, supported by Kolmogorov–Smirnov (K–S) statistical tests, confirm that the log-normal distribution provides the most appropriate representation of the crack width and crack spacing.

Chapter 5　Evaluation of tensile stress-strain relationship of SHCC

Chapter 5 proposes a tensile stress–strain constitutive model for SHCCs by integrating the statistical results of crack width and crack spacing obtained from the PVA-FRCC plate specimens in Chapter 4 with the analytical models proposed in Chapters 2 and 3. The proposed model explicitly incorporates the effects of fiber dimensional characteristics and fiber orientation, thereby enabling a more comprehensive representation of the tensile behavior of SHCCs.

Based on the differential equations describing the compatibility between bond deformation and stress, this chapter derives theoretical relationships among crack spacing, effective anchorage length, and slip of fiber at ultimate stage, each characterized by fiber dimensional parameters. The derivation is founded on three key assumptions: (1) the increment of pull-out force terminates after the formation of the second crack in the target fiber; (2) the bond stress stays constant distributed within the effective anchorage length; and (3) the slip of fiber at ultimate stage is proportional to the square root of the fiber diameter. These theoretical relationships are fitted to the experimental statistical results of crack width and crack spacing obtained from the PVA-FRCC thin plate specimens presented in Chapter 4. On this basis, the relationships between crack spacing and fiber diameter for other fiber dimension types are extrapolated.

Using the derived model, the ultimate tensile strain of the SHCC material is estimated to reach approximately 4.0 % when the fiber orientation intensity tends toward infinity. Additionally, the stress–strain response is calculated for the case where the fiber orientation intensity equals one, representing a random fiber orientation, thereby demonstrating the model's applicability to both highly oriented and randomly dispersed fiber systems.

Chapter 6　Conclusions and prospects

Chapter 6 provides a comprehensive synthesis of the preceding chapters and offers a forward-looking perspective on future research directions.

Contents

Chapter 1 Introduction

1.1 Research background

1.1.1 Development of FRCC

Concrete is the most widely used construction material in civil engineering; however, its inherent brittleness and limited tensile capacity often lead to sudden cracking and poor post-cracking performance. To overcome these deficiencies, fiber-reinforced cementitious composites (FRCCs) have been developed by incorporating short discrete fibers into the cementitious matrix, thereby enhancing crack control capability, energy absorption capacity, and overall ductility. Among various types of FRCCs, strain-hardening cementitious composites (SHCCs) represent an advanced class of materials that exhibit pseudo-ductile behavior under uniaxial tension loading, characterized by the formation of multiple fine cracks with limited crack widths instead of a single localized crack.

In the 1980s, Naaman et al. [1-1] reported that the incorporation of discontinuous short fibers into cementitious matrices can significantly enhance the tensile and flexural strength, toughness, and energy absorption capacity of the resulting composites. The mechanism underlying tensile enhancement was attributed primarily to the elastic elongation of fibers after matrix cracking and the resistance mobilized during fiber pull-out. Subsequent studies demonstrated that strain-hardening behavior accompanied by multiple cracking in short-fiber-reinforced cementitious composites can only be achieved when several essential conditions are satisfied, including a sufficient number of bridging fibers across cracks, adequately high fiber–matrix interfacial bond strength, and sufficiently long embedded fiber lengths capable of sustaining the additional load induced by matrix cracking and debonding [1-2].

In the 1990s, Li and Leung [1-3], based on micromechanics, fracture mechanics, and statistical theories, conducted in-depth investigations into fiber properties, matrix characteristics, and fiber–matrix interfacial micromechanical parameters. Through this systematic research, they developed a novel class of cementitious composites exhibiting stable strain-hardening behavior accompanied by multiple cracking, which was termed Engineered Cementitious Composites (ECC). A comprehensive micromechanical framework was established to explain this behavior. In this framework, micromechanical modeling focuses on fiber-bridging behavior, particularly the transfer and redistribution of stress through fiber–matrix interfacial bonding; fracture mechanics modeling examines the initiation and propagation of matrix cracks and the debonding and slip processes experienced by fibers during pull-out; and statistical principles are employed to characterize the inherent randomness associated with fiber position and orientation at crack planes, ultimately leading to the formulation of the fiber bridging stress–crack opening displacement relationship [1-4]. Building upon this foundation, Li [1-5] further proposed a performance-driven design methodology for ECC, which aims to establish a close linkage among structural performance, macroscopic material behavior, and micromechanical properties across multiple length scales.

Since the beginning of the 21st century, extensive experimental and theoretical studies have been conducted on fiber-reinforced cementitious composites incorporating various types of short fibers [1-6~1-9]. These studies have addressed fundamental mechanical properties , durability performance, and the development of corresponding evaluation methods and analytical models, thereby substantially advancing the understanding and application of FRCCs.

1.1.2 Classification and scope of FRCC

Prior to initiating the search, it is essential to clearly define the scope of FRCC in order to appropriately delimit the search parameters and maximize the inclusion of relevant literature, thereby enhancing search efficiency and accuracy.

As defined by Naaman and Reinhardt [1-6], High-Performance Fiber-Reinforced Cementitious Composites (HPFRCC) are fiber-reinforced, cement-based materials characterized by multiple cracking and strain-hardening behavior under uniaxial tension loading. This definition aligns with the broader objective of evaluating the applicability of Ductile Fiber-Reinforced Cementitious Composites (DFRCC) in structural applications subjected to various stress conditions, particularly emphasizing their high toughness. The ductile performance of DFRCC encompasses not only the intrinsic fracture toughness of the material but also its enhanced toughness and deformability when integrated into structural systems.

The Japan Society of Civil Engineers (JSCE) committee has developed a comprehensive framework of design and construction guidelines for FRCC. Within this framework, FRCC is defined as a broad category of fiber-reinforced cement-based materials, encompassing the above mentioned HPFRCC, DFRCC, and conventional Fiber-Reinforced Concrete (FRC) [1-7]. The classification is primarily based on fiber type, compressive strength, and toughness characteristics. These guidelines also include a recommended procedure for conducting uniaxial tension tests. In this study, the terminology and scope adopted are based on the definitions provided in the above JSCE publications [1-8]. Fig. 1 illustrates the hierarchical relationship among various types of fiber-reinforced composites, as outlined in the recommendation guideline by JSCE published in 2024.

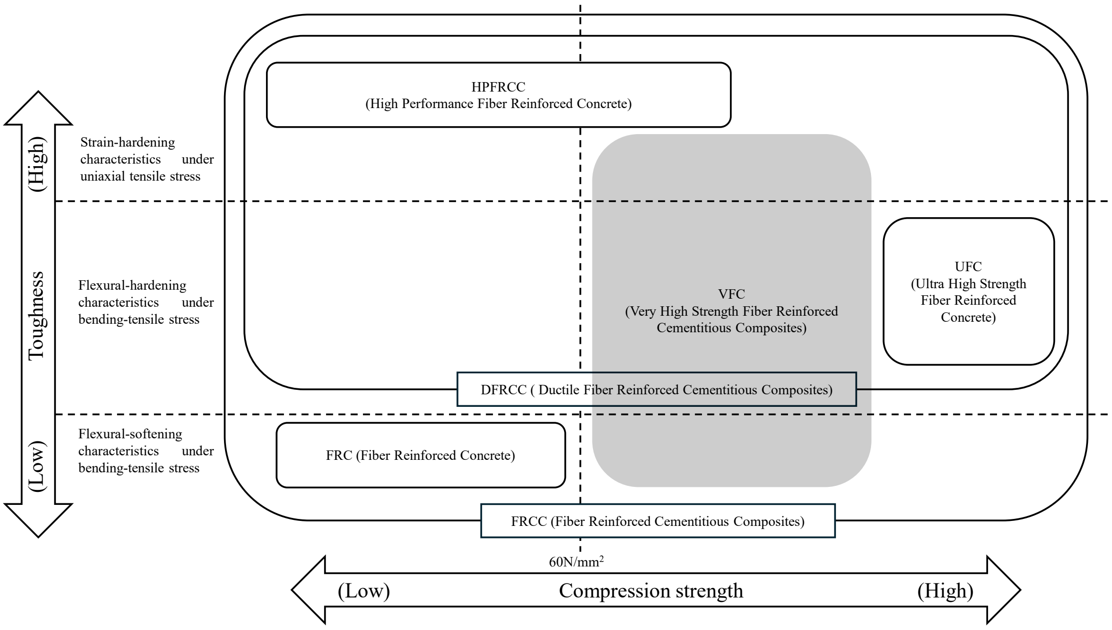

Figure 1-1 Overview of VFC application scope [1-8]

The following section provides a comprehensive review of the existing literature. Particular emphasis is placed on previous research efforts and recent advancements concerning the fundamental experimental methods used to characterize the tensile performance of FRCCs, as well as the development of bridging laws and tensile stress–strain relationships.

1.2 Research survey on tensile stress-strain relationship of SHCC

1.2.1 Tensile stress-strain relationship of SHCC

The tensile stress–strain model of strain-hardening fiber-reinforced cementitious composites (SHCC/ECC) is a constitutive framework established on the basis of underlying micromechanical mechanisms. It characterizes the tensile behavior of the material at various critical stages and provides insight into the interaction between multiple cracking propagation and fiber bridging mechanisms. Such models not only contribute to a deeper understanding of the deformation and failure processes of SHCC/ECC but also offer theoretical guidance for material design and engineering applications. Table 1-1 summarizes the tensile stress–strain models for SHCC/ECC proposed in the literature. Parameters with equivalent meanings among the models listed in the table have been unified.

References [1-15,1-16], based on extensive uniaxial tensile test (UTT) results of ECC/SHCC, divided the tensile stress–strain curve into three stages—elastic stage, strain-hardening stage, and strain-softening stage—using the matrix cracking point and the peak stress point as reference markers. They proposed a bilinear tensile stress–strain model under uniaxial loading by neglecting the softening stage. On this basis, References [1-9~1-11,1-18] adopted a trilinear model to more comprehensively describe the uniaxial tensile behavior of SHCC/ECC, including the post-peak softening stage.

Reference [1-17] further considered the stress increase within the strain-hardening stage associated with multiple crack formation, which was attributed to the slip-hardening effect of fibers, and employed a bilinear model with different slopes to describe the stress–strain response during strain hardening. The model proposed in Reference [1-12] simplified the expression of the softening stage; however, it is applicable only to PVA-ECC systems and thus has a relatively limited range of applicability. The saw-tooth model introduced in Reference [1-13] more accurately captures the actual tensile response and multiple cracking characteristics of SHCC/ECC during the strain-hardening stage. Nevertheless, it exhibits certain deviations in the low-strain region and involves relatively complex expressions, making it less convenient for practical engineering applications.

The model proposed in Reference [1-14] demonstrates better adaptability to multi-fiber systems; however, the large number of parameters involved limits its practicality in guiding material design and production. Reference [1-19] incorporated the effect of fiber volume fraction into a bilinear model; yet, as an empirical formulation, it requires further experimental validation. Finally, the bilinear model proposed in Reference [1-72] maintains the cracking stress as the stress level throughout the strain-hardening stage until the ultimate state is reached. Reference [1-60] mentions several potential stress-strain models for Dutile Fiber Reinforced Cementitious Composite (DFRCC), including elastoplastic and rigid-plastic models.

Table 1-1 Summary of tensile stress-strain model of SHCC/ECC

Ref.	Model	Advantages & disadvantages
[1-9] [1-10] [1-11] [1-18]	$\sigma=\begin{cases}E_1\varepsilon,\ 0<\varepsilon\le\varepsilon_{cr}\\ \sigma_{cr}+E_2(\varepsilon-\varepsilon_{cr}),\ \varepsilon_{cr}<\varepsilon\le\varepsilon_{peak}\\ \sigma_{peak}-E_3(\varepsilon-\varepsilon_{peak}),\ \varepsilon>\varepsilon_{peak}\end{cases}$	Applicable to various ECC/SHCC materials; require more engineering and experimental validation.
[1-12]	$\sigma=\begin{cases}E_1\varepsilon,\ 0\le\varepsilon<\varepsilon_{cr}\\ \sigma_{cr}+E_2(\varepsilon-\varepsilon_{cr}),\ \varepsilon_{cr}<\varepsilon\le\varepsilon_{peak}\\ ce^{d\varepsilon},\ \varepsilon_{peak}\le\varepsilon\le\varepsilon_u\end{cases}$	Only applicable to PVA-SHCC; better description for softening stage.
[1-13]	$\sigma=\begin{cases}E_1\varepsilon,\ 0<\varepsilon\le\varepsilon_{cr}\\ \sigma_{cr}+\dfrac{A_1}{a_1}+b_1(\varepsilon-\varepsilon_{cr}),\ \varepsilon_{cr}<\varepsilon\le\varepsilon_1\\ \sigma_1+\dfrac{A_2}{a_2}+b_2(\varepsilon-\varepsilon_1),\ \varepsilon_1\le\varepsilon\le\varepsilon_u\\ \sigma_u\dfrac{\varepsilon/\varepsilon_u}{c_1(\varepsilon/\varepsilon_u-1)^2+\varepsilon/\varepsilon_u},\ \varepsilon_1\le\varepsilon\le\varepsilon_{nu}\end{cases}$	More accurately to describe the multi-crack and strain-hardening behaviors; relatively low accuracy in low-strain stage and complex in expression with parameters and for practical applications.

[1-14]	$\sigma=\begin{cases}E_1\varepsilon,\ 0\le\varepsilon<\dfrac{\sigma_{ss}}{E_1}\\ \sigma_{ss}+k_1(\varepsilon-\dfrac{\sigma_{ss}}{E_1}),\ \dfrac{\sigma_{ss}}{E_1}<\varepsilon\le\varepsilon_u\\ k_2\sigma_u,\ \varepsilon_u\le\varepsilon\le\varepsilon_u\\ k_1=\dfrac{\sigma_u-\sigma_{ss}}{\varepsilon_u-\dfrac{\sigma_{ss}}{E_1}},\ k_2=(\dfrac{\varepsilon_u}{\varepsilon})^{4/RI_v^2}\end{cases}$	Applicable for multi-type fiber reinforced composites; complex in expression with parameters and for practical applications.
[1-15] [1-16]	$\sigma=\begin{cases}\dfrac{\sigma_{fc}}{\varepsilon_{fc}}\varepsilon,\ 0<\varepsilon\le\varepsilon_{fc}\\ \sigma_{fc}+\dfrac{\sigma_u-\sigma_{fc}}{\varepsilon_u-\varepsilon_{fc}},\ \varepsilon_{fc}<\varepsilon\le\varepsilon_u\end{cases}$	Simplification of tri-linear model; neglecting the effect of softening stage; requires more engineering and experimental validation.
[1-17]	$\sigma=\sigma_{mc}+(\sigma_u-\sigma_{mc})\dfrac{\varepsilon-\varepsilon_{mc}}{\varepsilon_u-\varepsilon_{mc}},\ \varepsilon_{mc}<\varepsilon\le\varepsilon_u$	Considering the slip-hardening effect in multi-cracking opening stage.
[1-19]	$\sigma=\begin{cases}a_1+b_1\exp(m_1V_{\mathrm{f}}),\ 0<\varepsilon\le\varepsilon_{cr}\\ a_2+b_2\exp(m_2V_{\mathrm{f}}),\ \varepsilon_{cr}<\varepsilon\le\varepsilon_u\\ \varepsilon_u=a_3+b_3\exp(m_3V_{\mathrm{f}})\end{cases}$	Same function expression with many experiment-based parameters; only considering the effect of fiber volume fraction.
[1-72]	$\sigma=\begin{cases}\dfrac{\sigma_{fc}}{\varepsilon_{fc}}\varepsilon,\ 0<\varepsilon\le\varepsilon_{fc}\\ \sigma_{fc},\ \varepsilon_{fc}<\varepsilon\le\varepsilon_u\end{cases}$	Bi-linear model. Probability for underestimate the tensile stress of SHCC

$E_1=\dfrac{\sigma_{cr}}{\varepsilon_{cr}}$, elastic tensile modulus ; $E_2=\dfrac{\sigma_{peak}-\sigma_{cr}}{\varepsilon_{peak}-\varepsilon_{cr}}$, modulus at strain-hardening stage ;

$E_3=\dfrac{\sigma_{peak}-\sigma_d}{\varepsilon_{peak}-\varepsilon_d}$, modulus at destructive stage.

σ_{cr}, cracking stress; σ_{peak}, peak stress; σ_d, destructive stress

ε_{cr}, cracking strain; ε_{peak}, strain at peak stress; ε_d, destructive strain; ε_{nu}, ultimate train

ε_1, the strain at the end of the hardened section I;

ε_u, the strain when the ultimate tensile stress is reached;

$A_1=(-\dfrac{2}{\pi})\times\sum\dfrac{\sin(2\pi kf_1(\varepsilon-\varepsilon_{cr}))}{k},\ (k=1,2,3,\cdots\infty)$

$A_2=(-\dfrac{2}{\pi})\times\sum\dfrac{\sin(2\pi kf_2(\varepsilon-\varepsilon_{cr}))}{k},\ (k=1,2,3,\cdots\infty)$, sawtooth functions

a_1, a_2, b_1, b_2, c_1, parameters of sawtooth functions.

RI_v, fiber reinforcing parameter.

σ_{fc}, initial yield stress, ε_{fc}, initial yield strain, σ_u, ultimate tensile stress, ε_u, ultimate tensile strain.

1.2.2 Theory calculation of crack spacing

For each snapping point of the model, both the stress at that point and the corresponding strain must be explicitly defined. For SHCC materials that achieve high tensile ductility through the formation of multiple cracks, the ultimate tensile strain—representative of the overall deformation capacity of the composite—is governed by the crack spacing [1-14]. In other words, the determination of crack spacing is of critical importance for building the stress-strain relationship of SHCC materials.

Aveston et al. [1-20,1-21] derived the theoretical mean crack spacing of brittle matrix composites reinforced with continuously aligned fibers under saturated cracking conditions, demonstrating that the ultimate average crack spacing should lie between s_{cr} and $2s_{\mathrm{cr}}$. The expression for s_{cr} was given as Eq. (1-1).

$$s_{\mathrm{cr}} = \frac{V_{\mathrm{m}}\sigma_{\mathrm{mu}}d_{\mathrm{f}}}{4V_{\mathrm{f}}\tau} \qquad \text{Eq. (1-1)}$$

where, d_{f} is fiber diameter, V_{m} is the matrix volume fraction, V_{f} is the fiber volume fraction, σ_{mu} is the matrix cracking strength, and τ is the interface friction. For brittle matrix composites reinforced with randomly oriented discontinuous fibers, the theoretical solution for s_{cr} can be obtained by considering the stress transfer to the crack plane through inclined short fibers, as expressed in Eq. (1-2) [1-22].

$$s_{\mathrm{cr1}} = \frac{L_{\mathrm{f}} - \sqrt{L_{\mathrm{f}}^2 - 2\pi L_{\mathrm{f}} s_{\mathrm{cr}}}}{2} \qquad \text{Eq. (1-2)}$$

where, L_f is the discontinuous fiber length, and s_{cr} is defined in Eq. (1-1).

Wu and Li [1-23] investigated the effects of fiber snubbing and fiber bundling on the multiple crack spacing of discontinuous, randomly oriented fiber-reinforced brittle matrix composites. By accounting for the snubbing effect—whereby fibers are pulled out at an inclination angle relative to the loading axis and the resulting compressive action amplifies the fiber–matrix interfacial resistance and bridging force—the original formulation in Eq. (1-2) was further refined, leading to the modified expression shown in Eq. (1-3).

$$s_{\mathrm{cr2}} = \frac{L_{\mathrm{f}} - \sqrt{L_{\mathrm{f}}^2 - 2\pi\psi L_{\mathrm{f}} s_{\mathrm{cr}}}}{2} \qquad \text{Eq. (1-3)}$$

where, $\psi = \frac{4}{\pi g}$ is the correction factor for 3-D fiber randomness, $g = 2\frac{e^{\pi f/2}+1}{4+f^2}$ is snubbing factor, f is the snubbing coefficient.

Li and Leung [1-3] established the theoretical foundation for steady-state multiple cracking and minimum crack spacing (or crack saturation) based on the fiber-bridging law. Building upon this framework, Yang et al. [1-24] developed an analytical fiber-bridging model for ECC by incorporating bidirectional fiber debonding and pull-out, matrix micro-spalling, and the Cook–Gordon effect. Subsequently, Lu and Leung [1-25] further refined the model by considering matrix strength heterogeneity, the increase in fiber-bridging stress after crack formation, and the influence of fiber rupture on stress transfer and multiple cracking behavior in SHCC. Furthermore, Lu and Leung [1-26] presented a numerical model to investigate the stress field evolution and multiple cracking behavior of ECC under tensile loading. The model incorporated micromechanical descriptions of fiber bridging, matrix cracking, and stress redistribution to simulate the initiation, propagation, and saturation of multiple cracks. By explicitly considering the interaction between crack-bridging stress and matrix fracture properties, the numerical framework captures the transition from first cracking to steady-state multiple cracking and eventual localization.

More recently, Luo et al. [1-27] presented a predictive model for the tensile properties of ECC based on a continuous crack tracking algorithm. The model explicitly simulated crack initiation, propagation, interaction, and saturation by coupling matrix fracture criteria with fiber-bridging behavior and stress redistribution. Unlike simplified approaches assuming instantaneous crack saturation, the proposed framework tracked the evolution of individual cracks throughout loading, enabling accurate prediction of crack spacing, crack width development, and the macroscopic tensile stress–strain response.

Li et al. [1-28] proposed a new generic model by incorporating chemical bonding at the fiber–matrix interface, interfacial slip-hardening behavior, and bidirectional fiber pull-out. The effectiveness of the proposed model was validated, providing a theoretical basis for significant improvements in ECC design, including steady-state crack width control and tensile performance at the ultimate limit state.

Li et al. [1-29] investigated the strain-hardening mechanism and crack control behavior of Hydraulic Engineered Cementitious Composites (HECC) through a combined theoretical and experimental approach. The study proposed a three-stage tensile strain-hardening process and introduced a novel fiber slip-out hypothesis to describe the interaction between fiber slip, crack width, crack spacing, and overall elongation. Based on force equilibrium and bond mechanics, analytical formulations were derived to predict fiber slip length, crack width, and ultimate tensile strain. Uniaxial tension experiments validated the proposed model, showing good agreement with theoretical predictions. The study further demonstrated the applicability of the model through successful large-scale implementation in a hydraulic engineering project, providing practical design guidance for HECC materials.

1.3 Previous research on bridging law of PVA-FRCC

The fiber-bridging law of fiber-reinforced cementitious composites is essentially an analytical stress–crack opening relationship derived from the fundamental principles of micromechanics, fracture mechanics, and statistical theory. In this framework, the fiber-bridging stress can be expressed as a functional relationship of Eq. (1-4) involving the matrix properties, fiber characteristics, fiber–matrix interfacial properties, and the crack opening displacement [1-30].

$$\sigma_{\mathrm{B}}(\delta) = f(V_{\mathrm{f}}, d_{\mathrm{f}}, L_{\mathrm{f}}, \sigma_{fu}, E_{\mathrm{f}}; K_{\mathrm{m}}, E_{\mathrm{m}}; G_{\mathrm{d}}, \tau_0, \beta, f, f'; \delta; \theta) \qquad \text{Eq. (1-4)}$$

where, V_{f} is fiber volume fraction (%), d_{f} is fiber diameter (mm), L_{f} is fiber length (mm), σ_{fu} is fiber tensile strength (MPa), E_{f} is fiber elastic modulus (GPa), K_{m} is fracture toughness of the cementitious matrix ($\mathrm{MPa} \cdot \sqrt{m}$), E_{m} is elastic modulus of cementitious matrix (GPa), G_{d} is chemical bond fracture energy (J/m^2), τ_0 is friction stress of fiber-matrix cross-section (MPa), β is slip-hardening coefficient, f is subbing coefficient, f' is fiber strength reduction factor, δ is pull-out displacement of fiber (mm), θ is fiber angle (rad).

In 1990, Li et al. [1-31] conducted a systematic experimental investigation into the pull-out behavior of synthetic fibers embedded in cementitious matrices, focusing on the effects of fiber inclination angle, fiber bundling, and surface treatment. The study demonstrated that inclined fibers exhibit increased pull-out resistance due to the snubbing effect, while fiber bundling alters both peak pull-out force and energy dissipation capacity. Surface treatment was shown to significantly modify interfacial bond characteristics, thereby influencing the balance between fiber pull-out and rupture. This work provided early experimental evidence that fiber orientation and interface conditions play a decisive role in governing crack-bridging capacity and laid an essential foundation for subsequent micromechanical modeling of bridging behavior.

Building upon experimental observations of fiber pull-out behavior, in 1991, Li et al. [1-32] developed a micromechanical model to describe tension-softening and bridging toughening mechanisms in short, randomly oriented fiber-reinforced brittle matrix composites. The model explicitly linked single-fiber debonding, frictional sliding, and pull-out responses to the macroscopic crack-bridging stress–crack opening relationship through statistical integration of fiber orientation and spatial distribution. This study established a theoretical pathway from microscale fiber–matrix interactions to mesoscale bridging laws, providing a rigorous analytical framework for understanding how fiber properties and interface mechanics govern post-cracking toughness and crack resistance in FRCC systems.

In 1997, Lin and Li [1-33] extended micromechanical modeling of crack bridging by introducing slip-hardening fiber–matrix interfaces. Their analytical work demonstrated that when interfacial friction increases with slip, the resulting bridging stress–crack opening relationship exhibits enhanced stability and higher energy dissipation. This behavior was shown to significantly improve crack resistance and promote steady-state crack propagation. The proposed model provided a mechanistic explanation for the superior crack-bridging performance observed in composites reinforced with hydrophilic fibers such as PVA, and highlighted the importance of interfacial design in achieving stable multiple cracking and strain-hardening behavior.

In 1998, Kanda and Li [1-34] investigated the apparent tensile strength and interfacial properties of high-strength hydrophilic fibers embedded in cementitious matrices. Through experimental analysis, they demonstrated that excessively strong fiber–matrix bonding can lead to premature fiber rupture, thereby limiting ductility and crack-bridging effectiveness. The study emphasized that optimal, rather than maximum, interfacial bond strength is required to ensure controlled fiber pull-out and enhanced energy absorption. This work provided critical insight into interface tailoring strategies for PVA fiber-reinforced cementitious composites and clarified the relationship between interfacial properties and macroscopic tensile performance.

In a continuation of their earlier work, Kanda and Li [1-35] systematically examined the combined effects of fiber tensile strength and fiber–matrix interface properties on crack-bridging behavior. The study quantitatively demonstrated how variations in interface strength shift the dominant failure mechanism from fiber pull-out to fiber rupture, thereby modifying the shape and magnitude of the bridging stress–crack opening relationship. This paper is widely regarded as a cornerstone in bridging law research for PVA-FRCC, as it directly linked microscale interfacial mechanics to mesoscale bridging performance and strain-hardening potential.

Step into 21st century, Redon et al. [1-36] focused on experimentally measuring and modifying the interfacial properties between PVA fibers and ECC matrices. Using single-fiber pull-out tests, the authors quantified interfacial bond strength and frictional parameters, and demonstrated that surface treatments could effectively reduce chemical bonding while enhancing frictional pull-out behavior. The results showed that controlled interface modification is essential for achieving stable crack bridging and multiple cracking in ECC. This study provided an important experimental bridge between interface engineering and practical bridging law design.

In 2008, Yang et al. [1-24] experimentally established the fiber-bridging constitutive law of ECC, quantifying the relationship between bridging stress and crack opening displacement and highlighting the critical role of fiber pull-out behavior, interfacial bond properties, and fiber orientation in achieving stable multiple cracking and strain-hardening behavior.

In 2016, Kanakubo et al. [1-37] investigated the influence of fiber orientation on the bridging performance of PVA-FRCC. Through experimental evaluation and analytical interpretation, the study demonstrated that enhanced fiber alignment significantly increases effective bridging fibers at the crack plane, thereby improving the magnitude and stability of the bridging law. The results clearly indicated that bridging law parameters are not intrinsic material constants but depend strongly on fiber orientation induced by casting and placement conditions. This work marked an important step toward incorporating processing effects into bridging law modeling.

A series of studies by Ozu and colleagues [1-38~1-40] extended bridging law concepts to structural-level phenomena. These works applied bridging law to evaluate size effects in bending, scatter in flexural response due to fiber distribution variability, and both tensile and shear crack-bridging behavior. Furthermore, an explicitly expressed bridging law model incorporating fiber orientation was proposed [1-41], enabling more realistic prediction of FRCC structural performance. These studies highlighted the necessity of linking crack-plane constitutive behavior with spatial variability and structural response.

Sunaga et al. [1-42] applied bridging law concepts to crack width evaluation in FRCC members interacting with deformed steel reinforcement. The study demonstrated that crack width development is governed by the combined effects of fiber bridging and steel bar force transfer, emphasizing the importance of bridging law in serviceability-oriented structural design. This work exemplified the extension of bridging law from material characterization to practical structural applications.

Curosu et al. [1-43] conducted a comprehensive experimental–analytical scale-linking study to investigate the influence of fiber orientation on crack-bridging mechanisms in strain-hardening cementitious composites (SHCC). Single-fiber pullout tests, μCT-based fiber orientation quantification, and uniaxial tension tests on miniature

SHCC specimens were systematically combined to derive orientation-dependent micromechanical parameters. These parameters were subsequently implemented into an analytical crack-bridging model to predict collective fiber-bridging laws. The study demonstrated that fiber inclination significantly affects both bond strength and in-situ fiber strength through snubbing and strength-reduction effects, and verified that micromechanical models can reliably bridge single-fiber behavior and composite-scale crack-bridging responses.

Liu et al. [1-44] proposed a novel fiber-bridging constitutive model to quantify the effects of matrix carbonation and fiber–matrix interface healing in PVA-SHCC. The study integrated environmental degradation and self-healing mechanisms into the bridging law framework, demonstrating how carbonation reduces bridging capacity while interfacial healing can partially restore crack-bridging performance. This work represents a significant advancement by extending bridging law modeling to durability-related phenomena, thereby enhancing the predictive capability of SHCC performance over long-term service conditions.

Shiferaw et al. [1-45] systematically investigated the influence of fiber dimensions on the bridging performance of PVA-FRCC. Experimental results showed that fiber diameter and length significantly affect peak bridging stress, pull-out behavior, and energy dissipation capacity. The study provided quantitative evidence that fiber geometry must be explicitly considered in bridging law formulation, supporting more generalized and parameterized models applicable to a wide range of SHCC systems.

Table 1-2 shows a summary of the bridging law of PVA-FRCC/ECC.

Collectively, these studies demonstrate the progressive evolution of bridging law research from microscale interface mechanics and single-fiber pull-out behavior to mesoscale crack-plane constitutive modeling and finally to structural-level and durability-oriented applications. The incorporation of fiber orientation, distribution variability, fiber geometry, and environmental effects has transformed the bridging law from a simplified theoretical concept into a comprehensive framework for predicting the mechanical performance and long-term behavior of PVA-based SHCC systems.

Table 1-2 Summary of the bridging law of PVA-FRCC/ECC

Authors (Year)	Main Focus	Key contribution to bridging law
Li et al. (1990)	Single fiber pull-out	Clarified effects of inclination, bundling, and surface treatment on pull-out behavior
Li et al. (1991)	Micromechanical modeling	Linked single-fiber pull-out to crack-bridging σ–w relationship
Lin & Li (1997)	Slip-hardening interface	Demonstrated enhanced bridging stability due to slip-hardening interfaces
Kanda & Li (1998)	Interface properties	Showed excessive interface strength leads to fiber rupture
Kanda & Li (1999)	Fiber strength & interface	Quantified effect of pull-out vs rupture on σ–w shape
Redon et al. (2001)	Interface modification	Measured and optimized PVA–ECC interface for stable bridging
Yang et al. (2008)	Bridging constitutive law	Two-way pullout and Cook-Gordon effect
Kanakubo et al. (2016)	Fiber orientation	Demonstrated strong fiber orientation dependence of σ–w relationship
Ozu et al. (2018)	Orientation-based model	Proposed σ–w model incorporating fiber orientation
Sunaga et al. (2020)	Crack width evaluation	Applied bridging law to serviceability design
Curosu et al. (2022)	Fiber orientation	Influence of fiber orientation on the bridging performance of different types of SHCC
Liu et al. (2023)	Durability & healing	Extended σ–w to carbonation and interface healing effects
Shiferaw et al. (2024)	Fiber dimensions	Quantified effect of fiber geometry on σ–w relationship

1.4 Research survey on uniaxial tension tests

Currently, several experimental methods are employed to evaluate the tensile response of fiber-reinforced cementitious composites (FRCC), including uniaxial tension test (UTT), three-point and four-point bending tests, split tensile tests, Brazilian disc splitting tests, and dynamic impact tensile tests. Among these, the uniaxial tension test is the only method capable of determining the true tensile strength under uniform uniaxial tension and directly capturing the constitutive tensile properties of FRCC [1-46]. This method enables the generation of a complete tensile stress–strain curve encompassing all deformation stages—pre-cracking, post-cracking, and strain-softening—thereby facilitating the observation of strain-hardening behavior and quantification of energy absorption during failure [1-47].

Despite its advantages, UTT presents significant operational challenges. The accuracy and reliability of the results are highly sensitive to the test setup, particularly the boundary conditions and mechanical alignment. As noted by Van et al. [1-48], key technical difficulties include precise specimen alignment, fabrication tolerances, effective gripping mechanisms, and the mitigation of secondary bending effects, all of which can compromise the integrity of the test. Furthermore, the lack of standardized testing protocols across laboratories exacerbates issues of repeatability and comparability, limiting the generalizability of findings.

This following section presents a review conducted aiming to identify and synthesize the key influencing factors of uniaxial tension tests used to investigate the tensile behavior of FRCC.

1.4.1 Searching strategy

Figure 1-2 gives an overview of the entire research methodology in this paper. The database Web of Science is adopted in this study, which is recognized as one of the most reputable and publisher-independent global citation platforms, and known for its comprehensive indexing of high-quality publications in the field of civil engineering. Given that search terms in the database operate as exact matches rather than conceptually backward-compatible queries, using broader terms such as FRCC does not necessarily retrieve studies categorized under more specific subtypes like ECC, despite ECC being a subset of FRCC as defined in Section 1.1.2. To ensure comprehensive coverage aligned with the research topic and scope, the search terms “tensi* test”, and those subdividing materials mentioned in Section 1.1.2 were applied using the field tags for title (TI) and author keywords (AK). The wildcard term “tensi*” was employed to capture variations such as “tension” and “tensile”, recognizing that some studies refer to use “tensile tests” rather than “tension tests”. Using a single, unmodified term would risk excluding relevant studies that meet the inclusion criteria. To refine the search, subject areas such as “concrete”, “textile”, “asphalt”, “polymer”, and “rock” were excluded through the use of the Boolean operator “NOT” within the same field tags. All search operations were executed simultaneously by utilizing the advanced search function in the Web of Science database, integrating field tags and logical operators. The publication date was customized to include records from 1980/01/01 to 2025/06/01. Subsequently, the initial 470 search results were further refined to enhance relevance using the filtering criteria available within the database. The document types were restricted to journal articles and proceeding papers, while the subject categories "Construction and Building Technology" and "Civil Engineering" were selected within the Web of Science classification system. Additionally, non-English publications were excluded. As a result, a total of 213 relevant articles were identified. The search link can be found in [1-49]. Among the retrieved results, some publications may fall outside the scope of the current research topic. While the uniaxial tension test is recognized as a fundamental and direct method for evaluating the tensile characteristics of cementitious composite materials, many studies either incorporate it as a comparative benchmark or validation alongside other tests—such as water permeability, freeze-thaw cycle resistance, numerical analysis—or do not explicitly reference it in their titles or abstracts. Consequently, to improve the accuracy of the screening process, relevant studies meeting the inclusion criteria were manually selected based on the titles, abstracts and full text retrieved from the Web of Science database. Eventually, 81 studies are selected.

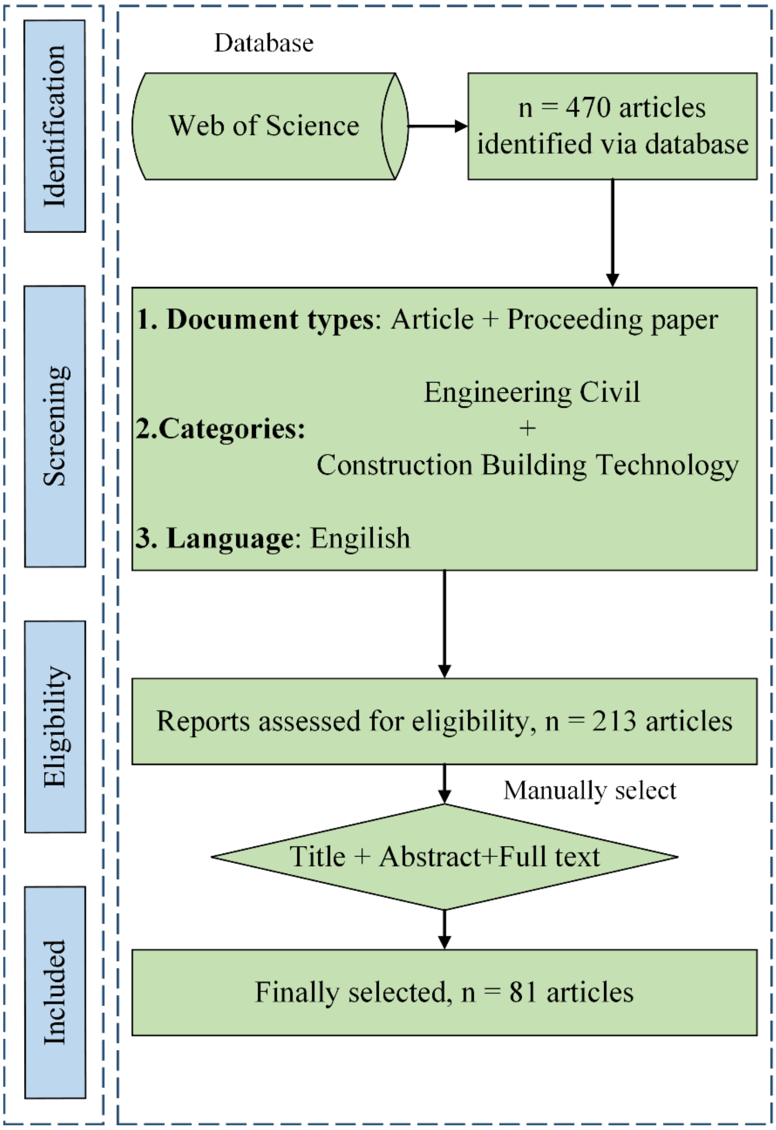

Figure 1-2 Research methodology

1.4.2 Search results

Figure 1-3 presents the statistical distribution of publishers associated with the 81 studies included in the review. The analysis reveals that Elsevier accounts for the majority of publications, contributing 48 out of 81 studies (approximately 59.3%). Springer Nature and the American Concrete Institute (ACI) follow with 14 and 7 publications, respectively. The remaining publishers each contributed fewer than five studies.

Figure 1-4 illustrates the distribution of publication years among the studies included in this review. A noticeable increase in the number of studies on uniaxial tension test of fiber-reinforced cementitious composites (FRCC) is observed after 2010, reflecting a growing global interest in the mechanical characterization and application of FRCC materials. This upward trend suggests that FRCC has gained recognition as a promising material in structural engineering, prompting more in-depth investigations into its tensile behavior and contributing to its broader adoption in practice.

Despite this growth, the absence of a unified international standard for conducting uniaxial tension tests on FRCC remains a challenge. Laboratories worldwide have adopted diverse specimen geometries, boundary conditions, and loading protocols, leading to variability in test outcomes and limiting cross-study comparability. In response, this study systematically categorizes and analyzes the specimen types and experimental setups reported in the literature, aiming to provide a consolidated reference framework.

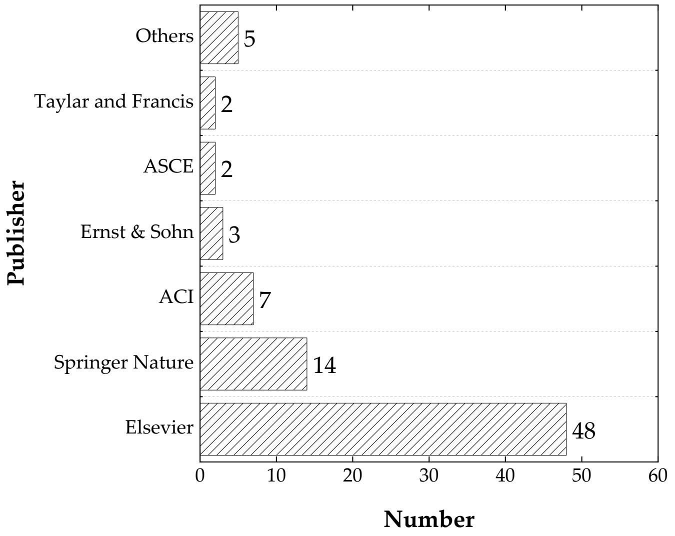

Figure 1-3 Statistic of publisher.

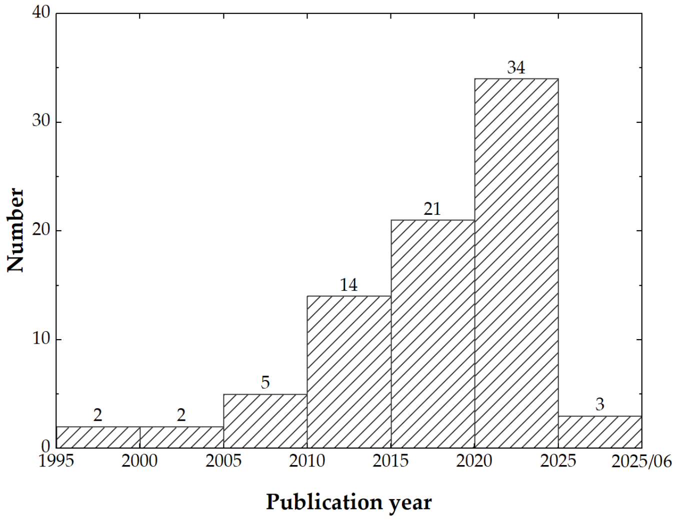

Figure 1-4 Statistic of publication year.

1.4.3 Influence factors in uniaxial tension test

1.4.3.1 Geometric of the specimens

Specimen geometry is considered to be one of the most basic and critical factors affecting the results of uniaxial tension tests of FRCC, including the shape and size of the specimen. The specimen geometry also affects other uniaxial tension test settings such as gauge length, boundary conditions and clamping. Currently, the primary geometries employed for uniaxial tension test of FRCC include dog-bone specimens (also referred to as dumbbell-shaped in some studies), modified dog-bone variants, prisms, and cylinders. During the hardening process, micro-defects generally exist in FRCC specimens such as interfacial transition zone (ITZ), which serve as stress concentrators and initial physical eccentricity which could not be avoided [1-50]. Under uniaxial tension loading, these defects serve as initiation sites for microcracks. As the microcrack width increases beyond a critical threshold, their growth contributes to a progressive reduction in tensile stiffness. Subsequently, a portion of the microcracks undergo branching and further localize into discrete macrocracks, interspersed with a limited number of narrower cracks [1-51]. Consequently, uncontrolled cracks may occur outside the designated gauge region during testing. Additionally, for prismatic and cylinder specimens, when steel loading splint plates are bonded to the specimen, mismatches in Young’s modulus and Poisson’s ratio between different materials of steel and cementitious composite can induce stress concentrations at the interface. These localized stresses frequently result in “bond failure”, characterized by the detachment or failure of the cementitious layer adjacent to the adhesive interface [1-52]. To mitigate this issue, some studies have introduced artificial notches at the center of the gauge region to localize crack initiation and facilitate crack observation, which aim to study and measure the relationship between the crack bridging stress and crack opening of a single crack [1-53,1-54]. For steel fiber reinforced concrete (SFRC), the Rilem TC 162-TDF [1-55] recommended using notched cylindrical specimens with a length and diameter of 150 mm to conduct uniaxial tension tests to determine the stress-crack opening relationship. However, artificial notch may limit the ability to monitor crack evolution, as stress concentrations at the notch often lead to immediate through-cracking, while other regions of the specimen remain unaffected.

Barragán et al. [1-54] investigated the tensile behavior of cylindrical notched specimens incorporating steel fibers and reported that specimen slenderness—defined as the ratio of length to diameter—does not exert a significant influence on the overall tensile response. This finding suggests that geometric scaling in terms of slenderness may be less critical when evaluating the tensile performance of fiber-reinforced composites under controlled loading conditions. Furthermore, their study examined the role of notch depth in modulating peak stress values. While the notch depth was found to have only a limited effect on the peak tensile stress, a deeper notch tended to correspond with an increase in the maximum stress observed during testing.

In dog-bone-shaped specimens, crack initiation is ordinarily anticipated within the reduced gauge section; however, because the reinforcing fibers span longitudinally through this neck region, it does not in practice constitute the weakest section of the specimen [1-56]. During testing, the specimen ends are secured by clamps, inducing pronounced stress concentrations at the junction between the central prismatic gauge length and the enlarged end regions [1-56,1-57]. Consequently, failure predominantly arises from clamp-induced stress concentrations and the attendant multiaxial stress state. Therefore, tensile specimens must be meticulously engineered to mitigate premature failure in the clamping zones and to ensure controlled crack initiation within the prescribed region of interest [1-58]. To prevent failure in the load introduction region and to ensure a defined gauge length for monitoring crack opening, Look et al. [1-59] applied a shape optimization strategy to mechanical structures based on a biological growth law derived from bionics. Using a computer-aided optimization method, they designed a dog-bone-shaped specimen by gradually reducing the cross-section area through the stretching triangle technique, thereby minimizing stress concentrations and avoiding failure due to peak stress.

Kanakubo [1-60] emphasized that smaller specimen dimensions and higher specific surface areas significantly influence the tensile characteristics measured in uniaxial tests.

Wille et al. [1-47] emphasized that top-bonded specimens lacking an enlarged cross-section area at the ends are unsuitable for investigating strain-hardening behavior, as they may not provide adequate anchorage for fiber engagement during tensile loading. In a related study, Douglas and Billington [1-61] examined the influence of loading rate on the tensile response of engineered cementitious composites (ECC) and observed that the random three-dimensional orientation of fibers in cylindrical specimens, combined with vertical casting, led to premature stress drops following initial cracking and limited strain-hardening across all displacement rates. These findings suggest that prismatic and cylindrical specimen geometries may not reliably capture the multiple cracking patterns characteristic of strain-hardening cementitious composites (SHCC). Consequently, the use of dog-bone-shaped specimens or geometries specifically designed to promote uniform stress distribution and fiber orientation is recommended for accurate assessment of tensile strain-hardening behavior.

Huang et al. [1-53] introduced notched dog-bone specimens to investigate the relationship between crack bridging stress and crack opening across a single crack, as Paegle and Fisher [1-47] noticed that the basic tensile characteristics of FRCC should be obtained from an individual crack. However, the notched dog-bone-shaped specimen is not suitable for uniaxial tension tests of SHCC, as these materials exhibit multiple cracking behavior.

1.4.3.2 Boundary condition

Boundary condition is another significant influence factor in uniaxial tension test, which is regarded to influence the tensile response including tensile strength, stress-strain response and crack pattern. In uniaxial tension tests, three primary boundary conditions are commonly employed: pin–pin, pin–fix, and fix–fix. These conditions are primarily dictated by the interface between the loading apparatus and the specimen clamping system, which in turn governs the transmission of the applied force. This study categorizes the boundary conditions used in selected experimental studies.

The classification is based on either explicit description provided by the original authors or visual inspection of the experimental setups in the manuscripts. Where such information is absent, the boundary condition is designated as unknown.

Heravi [1-62] investigated the strain rate sensitivity and mechanical behavior of strain-hardening cementitious composites reinforced with polyethylene (PE) fibers under both dynamic and quasi-static tension loading. In their setup, specimens were adhesively bonded to steel rings affixed to the loading platform using a fast-curing adhesive, thereby ensuring rigid, non-rotating boundary conditions at both ends. These fixed boundaries facilitate stable propagation of matrix discontinuities and virtual cracks under uniform tensile deformation [1-63,1-64].

It has been reported that short specimens subjected to fixed boundary conditions have been shown to achieve higher peak stresses and fracture energy, accompanied by symmetric crack propagation, in contrast to those subjected to rotating boundaries. In both configurations, crack initiation at one edge introduces eccentric loading. Under fix-end conditions, a counteracting moment develops on the uncracked side, promoting symmetric fracture. In contrast, rotating boundaries inhibit the formation of such moments, resulting in unilateral crack propagation due to reduced energy requirements [1-65~1-68]. For notched fiber-reinforced concrete (FRC) specimens tested in uniaxial tension with fixed platens, asymmetric crack growth may lead to crack plane rotation, influenced by the material inherent heterogeneity and imperfections in the loading system [1-69]. Therefore, Luo et al [1-70] believed that if the additional bending moment is within the controllable range and acceptable, fixed boundaries would be a reliable solution to obtain the natural tensile behavior of the specimen.

Rokugo et al. [1-71] investigated the uniaxial tensile behavior of strain-hardening cementitious composites (SHCC) using a boundary condition in which the specimen's lower end was rigidly fixed to a steel pedestal, while the upper end was hinged and connected to a force rod, which is considered as the pin-fix boundary condition. This configuration aligns with the testing method for fiber-reinforced cementitious composites (FRCC) recommended by the Japan Society of Civil

Engineers (JSCE) for evaluating multiple cracking behavior [1-72]. Amin et al. [1-73] identified the pin-fix end condition as a practical compromise among various uniaxial tension test configurations, offering improved alignment and reduced eccentricity during loading. This setup was found to be particularly suitable for uniaxial tension testing of steel fiber-reinforced concrete (SFRC), as it minimizes stress concentrations and promotes uniform load transfer across the specimen. Compared to other end conditions, such as rigid or pinned grips, the fixed rotating configuration better accommodates minor misalignments and helps preserve the integrity of the fiber-matrix interaction during tension loading, thereby enhancing the reliability of measured strain-hardening and cracking behavior. Figure 1-5 shows the details of Australia standard AS5100.5 and DR AS3600 uniaxial tension test specimen for SFRC which adopt the pin-fix boundary condition.

The pin–pin boundary condition facilitates proper specimen alignment and promote uniform deformation prior to crack initiation. A representative experimental setup utilizing this configuration is depicted in Figure 1-9a, demonstrating its prevalence and practicality in uniaxial tension test protocols, which can be achieved by installing universal joints at both ends between the specimen and the loading device. Huang et al [1-53] pointed out that, in static tests, such setup efficiently transfers the applied axial load from the loading device to the specimen without inducing bending effects, resulting in the sequential formation of multiple cracks as the load increases. However, under cyclic loading conditions, the behavior of an individual crack becomes significantly influenced by secondary bending moments, particularly when rotatable boundary conditions are present. These secondary bending moments arise from the non-uniform stiffness distribution across the crack plane, which is attributed to the heterogeneous spatial distribution of bridging fibers. Zhang et al. [1-51] developed an enhanced fixture by threading the tie rod directly into the specimen's end plate and mating it with a bespoke spherical joint on the testing-machine grip. This modification effectively eliminates the secondary bending moments introduced by conventional clamping devices and guarantees true axial alignment of the applied load.

Most of the selected studies adopt fixed–fixed boundary conditions in uniaxial tension tests of FRCC to ensure stable axial alignment and minimize eccentric loading. The dominance of this configuration may also reflect its effectiveness in promoting uniform stress distribution and facilitating the observation of strain-hardening and multiple cracking behavior. However, the relatively limited use of alternative boundary conditions highlights the need for further comparative studies to evaluate their influence on tensile response and to establish standardized testing protocols for FRCC materials. Figure 1-6 shows the comparison between boundary conditions of uniaxial tension tests.

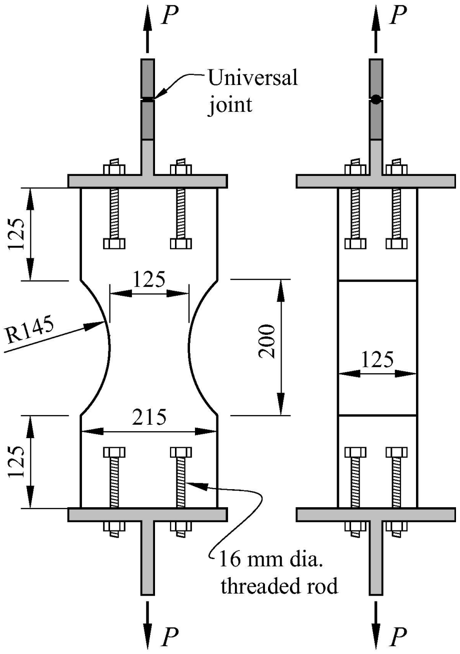

Figure 1-5 Details of AS5100.5 and DR AS3600 uniaxial tension test specimen for SFRC [1-73] (pin-fix).

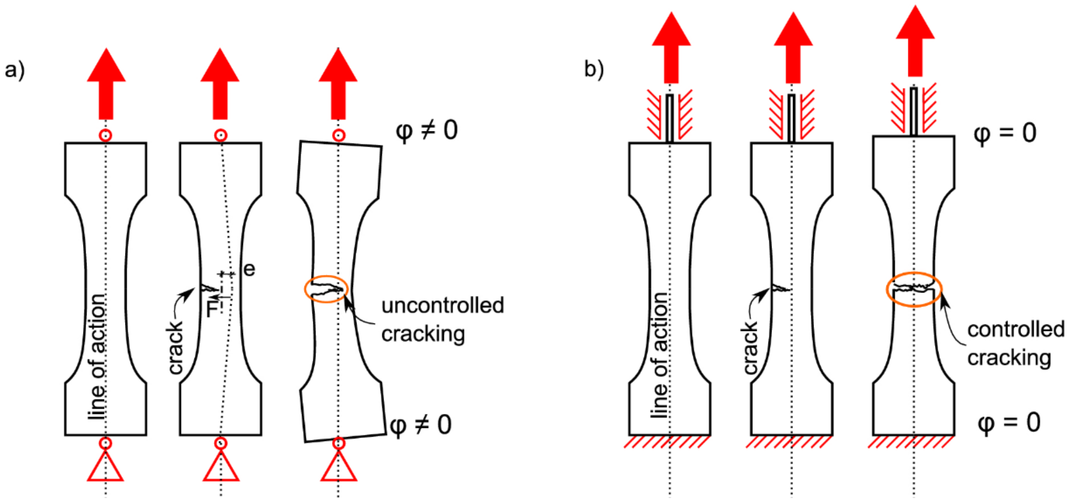

Figure 1-6 Comparison between boundary conditions of uniaxial tension tests; (a) double-sided hinged support and (b) double-sided fixed support. [1-74]

1.4.3.3 Loading rate

The loading rate is a critical parameter influencing the uniaxial tension behavior of fiber-reinforced cementitious composites (FRCC) and should be carefully considered in experimental design. In most FRCC uniaxial tension tests, displacement-controlled quasi-static loading is commonly employed. Strain rates below approximately 10^{-1}/s are generally classified as static or quasi-static, while those exceeding 1/s are considered dynamic [1-75]. Among the 81 studies reviewed in Section 1.4.1, excluding 12 that did not specify the loading rate and 4 that utilized load-controlled methods, the majority adopted static or quasi-static displacement-controlled loading. However, the specific loading rates varied considerably across studies.

Douglas and Billington [1-61] investigated the tensile response of high-performance fiber-reinforced cementitious composites (HPFRCC) and engineered cementitious composites (ECC) using cylindrical specimens under strain rates ranging from quasi-static to seismic levels (0.2 s^{-1}) and found that increased strain rates significantly influenced both tensile strength and strain capacity.

Furthermore, some studies employed multi-stage displacement-controlled loading protocols, wherein the loading rate was increased after reaching a predefined displacement threshold. This approach was intended to enhance the visibility of multiple cracking behavior and better capture the transition from elastic to strain-hardening phases. These findings underscore the importance of standardizing loading rate definitions and methodologies in FRCC uniaxial tension testing to ensure consistent characterization of strain-hardening and cracking phenomena.

1.4.3.4 Gauge section

The gauge length is typically determined by the geometry of the specimen and is intended to encompass the region where cracking is expected to occur. As noted by Benson and Karihaloo [1-76], an excessively long gauge length may lead to rebound effects due to the sudden release of stored elastic energy from regions outside the fracture process zone, potentially compromising the accuracy of the stress–strain response. Conversely, if the gauge length is too short, the fracture process zone may extend beyond the measured region, resulting in a loss of experimental control and unreliable data. Therefore, careful selection of the gauge length is essential to ensure that the fracture process is fully captured within the measurement zone, particularly in materials exhibiting strain localization or multiple cracking behavior. This consideration is especially critical in strain-hardening materials, where the spatial distribution of damage significantly influences the mechanical response.

1.4.3.5 Stiffness of loading device

The stiffness of the testing apparatus—including both the clamping and loading components—is a critical yet often overlooked factor influencing the accuracy and reliability of uniaxial tension tests. Its importance is frequently underestimated due to the difficulty in establishing quantifiable design criteria. Insufficient axial or flexural stiffness in the loading system can result in non-uniform stress distribution during testing, thereby affecting the initiation point, propagation path, and rate of crack development. Moreover, system flexibility introduces additional deformation, causing the measured crack opening displacement to include contributions from the clamp or loading frame, which compromises data accuracy [1-77,1-78]. For materials exhibiting multiple cracking behavior or subjected to cyclic loading (as discussed in Section 1.4.4.3), the progressive formation of cracks leads to a continuous evolution in the specimen's stiffness. This phenomenon is evidenced by variations in the slope of the load descending within the strain-hardening stage of the stress–strain curve, corresponding to the initiation of new cracks. In such cases, a loading system with inadequate stiffness may lead to significant variability in test results, destabilizing the stress path and reducing repeatability [1-79]. Even when round robin tests are conducted in accordance with the same standardized guidelines, variations in the stiffness of the testing apparatus can lead to significant discrepancies in the results obtained across different laboratories [1-80].

To address this issue, RILEM TC 162-TDF [1-55] proposed a quantitative criterion: the maximum difference between individual sensor readings at the end of the test should not exceed ten times the average displacement. In line with this recommendation, Fu et al. [1-81] developed a testing apparatus incorporating FRP bars and steel frames to enhance system stiffness and prevent premature specimen failure during loading, as Figure 1-7 shown.

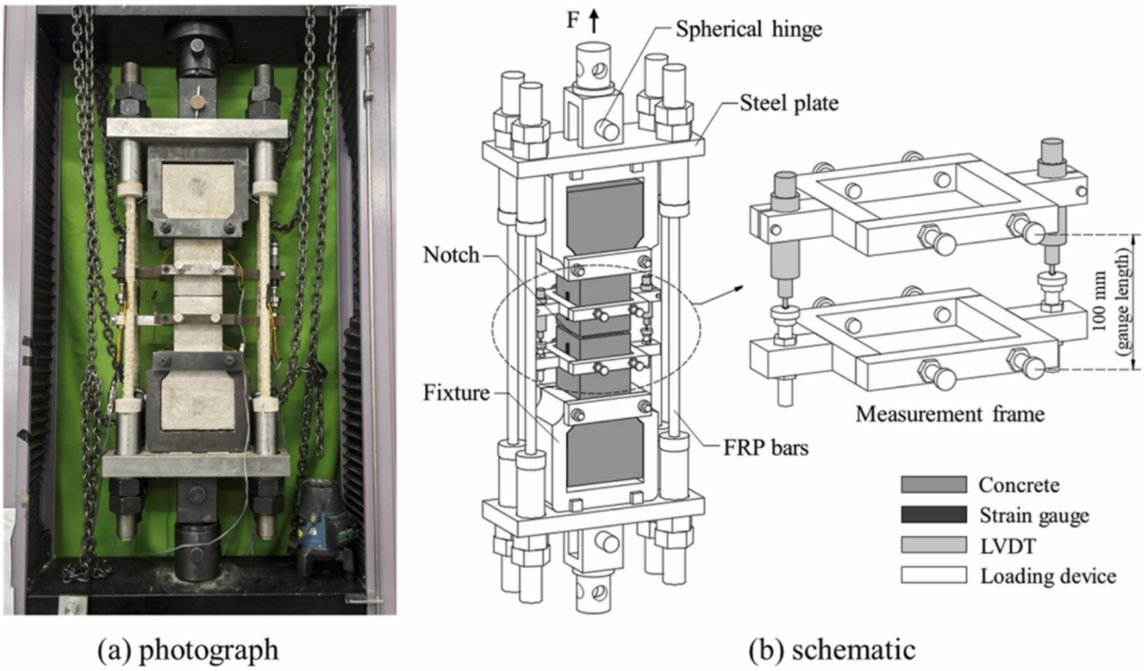

(a) photograph (b) schematic

Figure 1-7 Uniaxial tension test setup [1-81].

1.4.3.6 Measurement of DIC

The initiation and propagation of matrix discontinuities within the strain-hardening regime of fiber-reinforced cementitious composites (FRCC) are typically imperceptible to the naked eye and remain undetectable by conventional sensing technologies. However, these microstructural changes can be effectively captured through strain field analysis using Digital Image Correlation (DIC) techniques [1-63]. DIC offers a non-contact, full-field measurement approach that enables the visualization and quantification of surface deformations, making it particularly suitable for detecting fine crack patterns and evaluating tensile behavior in FRCC specimens.

To ensure accurate and reliable measurements, it is recommended that a DIC system equipped with high-speed, high-resolution optical imaging capabilities camera and advanced analysis software be employed during testing. This setup facilitates the acquisition of detailed statistical data, including crack widths and crack spacings, which are essential for characterizing the mechanical performance of FRCC under uniaxial tension loading.

Prior to DIC analysis, specimens are prepared by applying a white matte base coat to minimize light reflections and enhance image contrast. Subsequently, a fine, non-repetitive black speckle pattern—composed of approximately circular spots—is applied to the surface to enable precise tracking of strain fields during deformation [1-82~1-84]. This speckle pattern serves as a reference grid for the DIC software, allowing for high-fidelity mapping of displacement and strain across the specimen surface.

This study makes a statistic of whether Digital Image Correlation (DIC) was employed in the 81 publications identified through the Section 1.4.1 screening process. Researches that did not explicitly indicate the use of DIC were conservatively categorized as "not used." The statistical results reveal that 17 studies—accounting for over one-fifth of the total—utilized DIC systems to capture strain distribution and crack evolution during uniaxial tension test. The remaining studies relied predominantly on conventional displacement measurement techniques such as Linear Variable Differential Transformers (LVDTs) or extensometers. Notably, all publications incorporating DIC were released post-2010 and demonstrate a progressive increase in frequency in recent years. This trend underscores the growing significance of DIC in the accurate characterization of FRCC tensile behavior, driven by both the advancement of imaging technologies and the expanding scope of research in fracture mechanics and strain localization phenomena.

1.4.3.7 Clamping

The clamping method, along with the boundary conditions and the stiffness of the testing apparatus, plays an important role in influencing the outcomes of uniaxial tension tests. Improper alignment or inadequate fixture design can introduce unintended bending moments, leading to inaccurate stress–strain measurements and premature failure. Therefore, prior to testing, it is essential to ensure that the centers of the clamping device, specimen, and loading axis are precisely aligned along a common axis to minimize initial misalignment effects. Figure 1-8 shows examples of end shapes for uniaxial tension tests.

This section introduces two commonly employed clamping techniques identified across the 81 studies screened in Section 1.4.1, highlighting their mechanical implications and suitability for achieving uniform axial stress distribution.

The anchor clamp serves as the interface between the testing machine and the test specimen, functioning primarily to secure and align the specimen while ensuring uniform transmission of the tension load. It incorporates articulating joints in two planes parallel to the loading direction to eliminate the introduction of shear forces within the specimen [1-85].

Soft-clamp loading is typically implemented by interposing a rubber layer between the specimen and the grips of the testing apparatus. In this configuration, load transfer occurs via Coulomb friction at the interface. Once the static friction threshold is surpassed, slippage of the specimen may ensue, potentially leading to the formation of cracks within the clamping region [1-86].

Kwan et al. [1-57] addressed the issue of stress concentration at the junction between the prismatic section and enlarged ends of dog-bone-shaped specimens by proposing a side-glued steel plate loading method. This approach applies axial tension through steel plates glued to each end of the specimen, promoting a more uniform stress distribution. Numerical analysis confirmed the superiority of this method over conventional clamping methods by effectively minimizing stress concentrations and preventing premature failure.

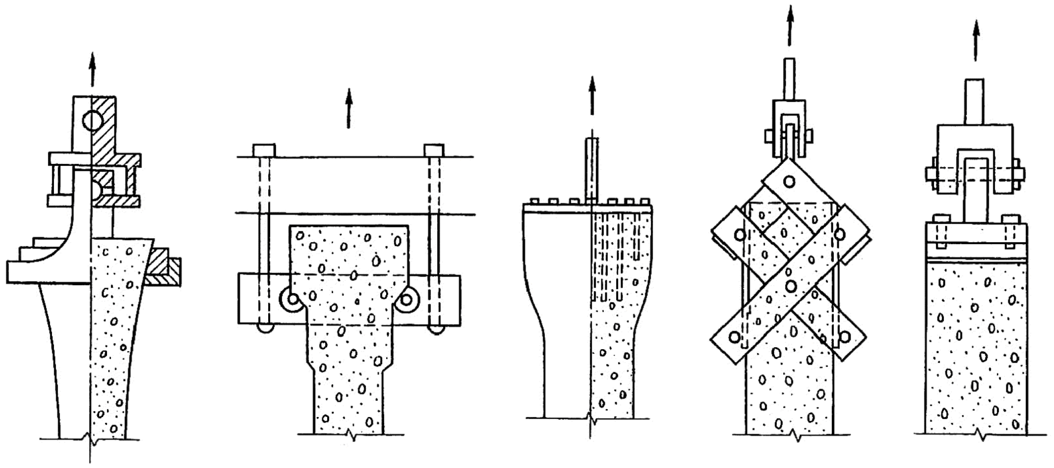

(a) (b) (c) (d) (e)

Figure 1-8 Examples of end shapes for uniaxial tension tests [1-60].

1.4.4 Summary

The following conclusions are drawn:

(1) Specimen Geometry: The predominant specimen types used in UTT are dog-bone, prismatic, and cylindrical geometries. To localize crack initiation, artificial notches are often introduced in the gauge section. dog-bone specimens can promote uniform stress distribution and facilitate observation of strain-hardening behavior.

(2) Boundary Conditions: UTT setups typically utilize three boundary conditions: fix–fix, pin–pin, and pin–fix. Fix–fix configurations lead to an ability to ensure stable axial alignment and minimize eccentric loading. However, this setup is sensitive to misalignment, which can introduce unintended bending moments and premature cracking. Pin–pin conditions, while easier to implement and effective in transferring axial loads without bending, may amplify local stiffness variations post-cracking. Therefore, boundary condition selection should be guided by the specific objectives of the test, particularly when evaluating strain-hardening and multiple cracking behavior.

(3) Loading Rate: Most studies employed displacement-controlled quasi-static loading, though the specific rates varied widely, reflecting the absence of a standardized protocol. It was observed that increasing the strain rate significantly affects both tensile strength and strain capacity, underscoring the need for consistent definitions and methodologies in rate-dependent testing.

(4) Gauge Length and Device Stiffness: These parameters exhibit a coupled influence on uniaxial tension test outcomes, interacting with other factors such as specimen geometry and boundary conditions. Their combined effect must be considered to ensure accurate interpretation of tensile behavior.

(5) Digital Image Correlation (DIC): DIC has emerged as a powerful non-contact, full-field measurement technique capable of visualizing and quantifying surface deformations. It is particularly effective in detecting fine crack patterns and

evaluating tensile behavior in FRCC specimens. The increasing adoption of DIC in recent years highlights its advantages over traditional strain gauges, including reduced measurement error and enhanced spatial resolution.

(6) Coupled Effects of Test Parameters: The influence of individual test parameters cannot be considered in isolation. Instead, their interactions must be evaluated holistically to design appropriate test configurations. A comprehensive understanding of these coupled effects is essential for accurately characterizing the tensile response of FRCC materials.

Considering the complexity and limited controllability of the factors affecting uniaxial tension tests, four-point bending tests are employed in this study to examine the mechanical characteristics of SHCC.

1.5 Research significance and outline of thesis

The superior tensile performance of SHCCs originates from the effective interaction between fibers and the surrounding matrix. After matrix cracking, tensile stress is transferred across crack through fiber bridging, allowing the composite to sustain increasing deformation while maintaining load-carrying capacity. This multiple-cracking mechanism leads to a significant improvement in tensile strain capacity and fracture energy compared to conventional concrete. As a result, SHCCs have attracted extensive research interest over the past decades and have shown great potential for applications in structural members, repair and strengthening systems, and durability-critical infrastructure.

In addition to testing challenges mentioned in section 1.4, fiber orientation plays a critical role in governing the mechanical response of SHCCs. Fiber orientation is strongly influenced by casting conditions, placing thickness, layer configuration, and the rheological properties of the fresh matrix etc. One-direction fiber alignment can significantly enhance bridging efficiency, leading to higher tensile strength and improved strain-hardening behavior without increasing fiber volume fraction. Conversely, unfavorable fiber orientation may deteriorate tensile performance and promote premature localization. Therefore, a quantitative understanding of fiber orientation and its influence on bridging behavior is essential for the rational design and performance prediction of SHCC materials.

Existing constitutive models for SHCCs have provided valuable insights into tensile stress–strain behavior; however, many of these models either assume idealized fiber distributions or do not explicitly account for the combined effects of fiber dimension, orientation, and bond mechanics. Furthermore, the relationship between experimentally observable crack characteristics—such as crack width and crack spacing—and the macroscopic tensile stress–strain response has not yet been fully established in a unified analytical framework.

In view of these issues, the present study aims to systematically investigate the mechanisms governing fiber orientation, crack development, and deformation capacity in SHCCs through a combination of visualization simulation, four-point bending tests on thin plate specimens, image-based statistical analysis of crack characteristics, and analytical modeling. By integrating fiber dimension, orientation intensity, and bond mechanics into a unified constitutive formulation, this research seeks to propose a generalized tensile stress–strain model capable of more reliably describing the deformation and load-carrying behavior of SHCCs. The outcomes of this study are expected to contribute to both the fundamental understanding of SHCC behavior and the practical design of high-performance fiber-reinforced cementitious materials.

Figure 1-8 shows the technical flowchart of this thesis. This thesis consists of six chapters.

Chapter 1 presents a comprehensive literature review on the tensile stress–strain behavior of SHCC, the fiber-bridging law of PVA fiber-reinforced cementitious composites (PVA-FRCC), and uniaxial tensile testing methods.

Chapter 2 evaluates the influence of placing thickness on fiber orientation distribution and bridging behavior based on visualization-based simulation experiments.

Chapter 3 builds upon the fiber orientation simulation results obtained in Chapter 2. By extending existing explicit fiber-bridging laws, a modified bridging law corresponding to the idealized case of infinite fiber orientation intensity is proposed.

Functionally layered FRCC specimens are then developed, and their mechanical performance is investigated through four-point bending tests.

Chapter 4 aims to obtain statistical crack characteristics of SHCC specimens at the ultimate state. Four-point bending tests are conducted on thin plate SHCC specimens, and statistical fitting methods are employed to quantitatively analyze the mathematical distributions of crack width and crack spacing.

Chapter 5 introduces three fundamental assumptions based on the second-order differential equation governing fiber–matrix bond–slip behavior and the crack characteristic statistics obtained in Chapter 4. On this basis, an explicit tensile stress–strain constitutive model for SHCC incorporating PVA fibers of different dimensions is derived and calibrated.

Chapter 6 summarizes the main findings of the preceding chapters and presents perspectives for future research.

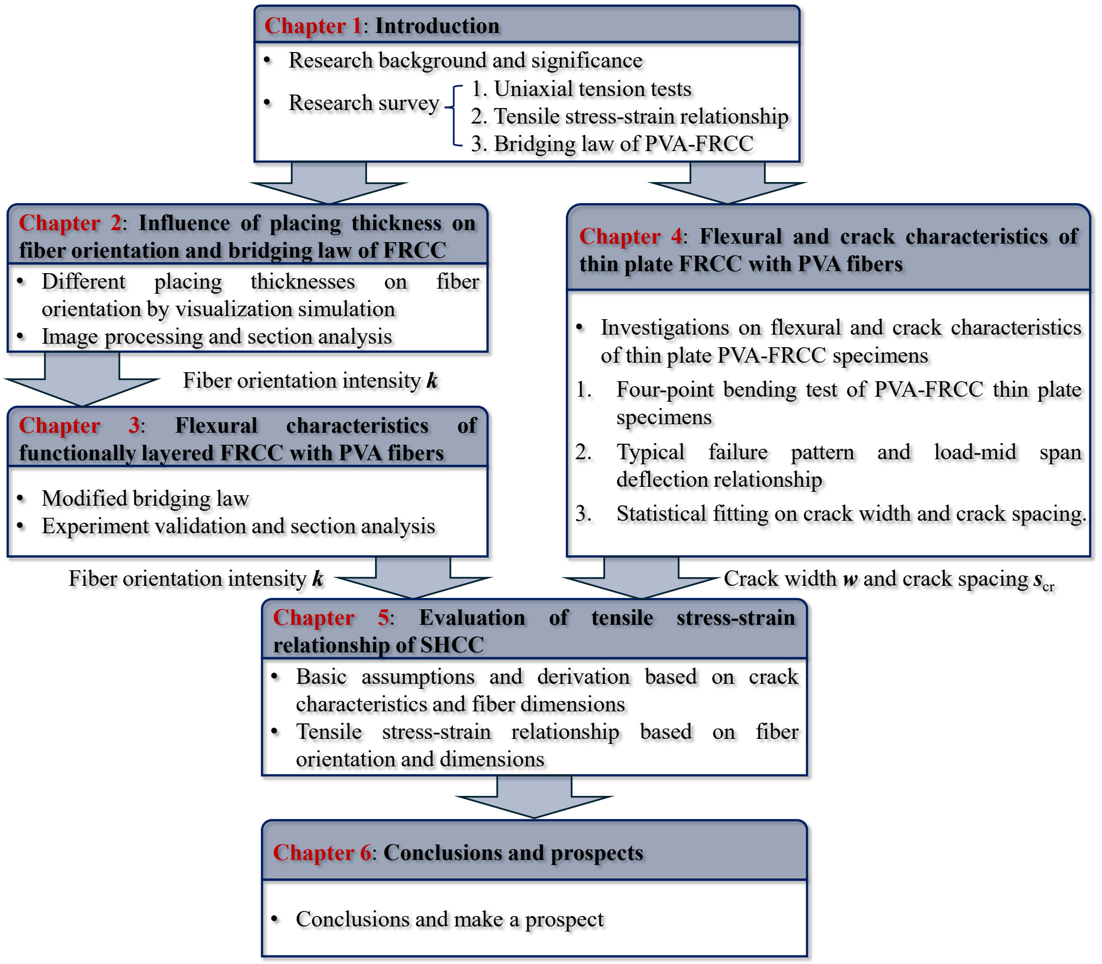

Figure 1-8 The technical flowchart of this thesis

Reference

[1-1] Naaman, A. E., & Gopalaratnam, V. S. (1983). Impact properties of steel fibre reinforced concrete in bending. International journal of cement composites and lightweight concrete, 5(4), 225-233.

[1-2] Delvasto, S., Naaman, A. E., & Throne, J. L. (1986). Effect of pressure after casting on high strength fibre reinforced mortar. International Journal of Cement Composites and Lightweight Concrete, 8(3), 181-190.

[1-3] Li, V. C., & Leung, C. K. (1992). Steady-state and multiple cracking of short random fiber composites. Journal of engineering mechanics, 118(11), 2246-2264.

[1-4] Li, V. C. (1998). ECC for repair and retrofit in concrete structures. Fracture Mechanics of Concrete Structures, FRAMCOS-3 Proceedings, 1715-1726.

[1-5] Li, V. C., Wang, S., & Wu, C. (2001). Tensile strain-hardening behavior of polyvinyl alcohol engineered cementitious composite (PVA-ECC). Materials Journal, 98(6), 483-492.

[1-6] Naaman, A. E., & Reinhardt, H. W. (1996). Characterization of high performance fiber reinforced cement composites—HPFRCC. In High performance fiber reinforced cement composites (Vol. 2, pp. 1-24).

[1-7] Rokugo, K. (Ed.). (2008). Recommendations for design and construction of high performance fiber reinforced cement composites with multiple fine cracks (HPFRCC). Japan Society of Civil Engineers, Concrete Committee.

[1-8] Uchida, H. (Ed.). (2024). Recommendations for Design and Construction of Very High Strength Fiber Reinforced Cementitious Composite Structures (Draft). Japan Society of Civil Engineers (JSCE).

[1-9] Yang, J., Deng, M., Wang, Y., & Zhang, Y. (2024). Uniaxial tensile test of high-strength high-ductility concrete (HSHDC): Mechanical response and toughness evaluation. Journal of Building Engineering, 89, 109332.

[1-10] Zhao, D., Wang, C., Li, K., Zhang, P., Cong, L., & Chen, D. (2022). An experimental and analytical study on a damage constitutive model of engineered cementitious composites under uniaxial tension. Materials, 15(17), 6063.

[1-11] Yu, H., Yang, D., Xiao, Y., Luo, Q., Qu, F., Zhu, D., ... & Zhang, Y. (2025). Experimental study on the constitutive model and energy evolution law of PE-ECC under uniaxial tension. Construction and Building Materials, 487, 142068.

[1-12] Zhang, T., Li, X., Zhang, L., & Huang K. (2023) Study on the uniaxial tensile constitutive model describing strain hardening and multiple cracking of ECC under uniaxial tension. Material Reports, 37(Z1), 22110282. (in Chinese)

[1-13] Li, L., Chen, H., Yu, H., Ma, H., Fan, H., Chen, X., & Gao, Y. (2024). A sawtooth constitutive model describing strain hardening and multiple cracking of ECC under uniaxial tension. Reviews on Advanced Materials Science, 63(1), 20240048.

[1-14] Hou, J., Bai, J., Mou, H., & Xiang, Z. (2024). Tensile properties and constitutive model of cost-effective multiscale hybrid fiber reinforced strain hardening cementitious composites. Frontiers in Materials, 11, 1378089.

[1-15] Maalej, M., & Li, V. C. (1994). Flexural/tensile-strength ratio in engineered cementitious composites. Journal of Materials in Civil Engineering, 6(4), 513-528.

[1-16] Kanda, T., Lin, Z., & Li, V. C. (2000). Tensile stress-strain modeling of pseudostrain hardening cementitious composites. Journal of Materials in Civil Engineering, 12(2), 147-156.

[1-17] Xiang-rong, CAI. The basic mechanical performance and strain hardening process theoretical analysis of ultra high toughness cementitious composites (Doctoral dissertation, Dalian: School of Civil Engineering, Dalian University of Technology, 2009: 48-91.(in Chinese)).

[1-18] Han, T. S., Feenstra, P. H., & Billington, S. L. (2003). Simulation of highly ductile fiber-reinforced cement-based composite components under cyclic loading. Structural Journal, 100(6), 749-757.

[1-19] Zhang, C., & Yang, X. (2019). Bilinear elastoplastic constitutive model with polyvinyl alcohol content for strain-hardening cementitious composite. Construction and Building Materials, 209, 388-394.

[1-20] Aveston, J. (1971). Single and multiple fracture. The properties of fiber composites, 15-26.

[1-21] Aveston, J., & Kelly, A. (1973). Theory of multiple fracture of fibrous composites. Journal of Materials Science, 8(3), 352-362.

[1-22] Aveston, J. (1974). Fibre reinforced cements-scientific foundations for specifications. In National Physical Laboratory Conference Proceedings, Composite-Standards testing and design (pp. 93-103).

[1-23] Wu, H. C., & Li, V. C. (1992). Snubbing and bundling effects on multiple crack spacing of discontinuous random fiber-reinforced brittle matrix composites. Journal of the American Ceramic Society, 75(12), 3487-3489.

[1-24] Yang, E. H., Wang, S., Yang, Y., & Li, V. C. (2008). Fiber-bridging constitutive law of engineered cementitious composites. Journal of advanced concrete technology, 6(1), 181-193.

[1-25] Lu, C., & Leung, C. K. (2016). A new model for the cracking process and tensile ductility of strain hardening cementitious composites (SHCC). Cement and Concrete Research, 79, 353-365.

[1-26] Lu, C., Leung, C. K., & Li, V. C. (2017). Numerical model on the stress field and multiple cracking behavior of engineered cementitious composites (ECC). Construction and Building Materials, 133, 118-127.

[1-27] Luo, Q., Zhang, J., Lu, Z., Wang, F., Zhang, Y., Liu, Z., & Jiang, J. (2023). A prediction model of the tensile properties of engineered cementitious composites (ECC) based on the continuous crack tracking algorithm. Journal of Building Engineering, 79, 107903.

[1-28] Li, J., Weng, J., Chen, Z., & Yang, E. H. (2021). A generic model to determine crack spacing of short and randomly oriented polymeric fiber-reinforced strain-hardening cementitious composites (SHCC). Cement and Concrete Composites, 118, 103919.

[1-29] Li, J., Shi, Y., Zhang, X., Wang, Y., Chen, C., Wu, C., & Zhu, D. (2025). Strain-hardening mechanism and crack control of hydraulic engineered cementitious composites (HECC): A theoretical and experimental study. Case Studies in Construction Materials, e05376.

[1-30] Chen T. (2004). Production and properties of cementitious composites with high-strength and high modulus PVA fiber reinforcement [Master's thesis]. Hefei University of Technology. (in Chinese) https://kns.cnki.net/KCMS/detail/detail.aspx?dbname=CMFD9904&filename=2004084436.nh

[1-31] Li, V. C., Wang, Y., & Backer, S. (1990). Effect of inclining angle, bundling and surface treatment on synthetic fibre pull-out from a cement matrix. Composites, 21(2), 132-140.

[1-32] Li, V. C., Wang, Y., & Backer, S. (1991). A micromechanical model of tension-softening and bridging toughening of short random fiber reinforced brittle matrix composites. Journal of the Mechanics and Physics of Solids, 39(5), 607-625.

[1-33] Lin, Z., & Li, V. C. (1997). Crack bridging in fiber reinforced cementitious composites with slip-hardening interfaces. Journal of the Mechanics and Physics of Solids, 45(5), 763-787.

[1-34] Kanda, T., & Li, V. C. (1998). Interface property and apparent strength of high-strength hydrophilic fiber in cement matrix. Journal of materials in civil engineering, 10(1), 5-13.

[1-35] Kanda, T., & Li, V. C. (1999). Effect of fiber strength and fiber-matrix interface on crack bridging in cement composites. Journal of Engineering mechanics, 125(3), 290-299.

[1-36] Redon, C., Li, V. C., Wu, C., Hoshiro, H., Saito, T., & Ogawa, A. (2001). Measuring and modifying interface properties of PVA fibers in ECC matrix. Journal of materials in civil engineering, 13(6), 399-406.

[1-37] Kanakubo, T., Miyaguchi, M., & Asano, K. (2016). Influence of Fiber Orientation on Bridging Performance of Polyvinyl Alcohol Fiber-Reinforced Cementitious Composite. ACI Materials Journal, 113(2).

[1-38] Ozu, Y., Watanabe, K., Yasojima, A., & Kanakubo, T. (2016). Evaluation of size effect in bending characteristics of DFRCC based on bridging law. In 7th International Conference of Asian Concrete Federation (Vol. 3).

[1-39] Kanakubo, T., Watanabe, K., & Ozu, Y. (2017, September). Simulation of scattering of bending characteristics of FRCC based on bridging law considering fiber distribution. - In International Conference on Strain-Hardening Cement-Based Composites (pp. 509-517). Dordrecht: Springer Netherlands.

[1-40] Ozu, Y., Yamada, H., Yasojima, A., Kanakubo, T. (2017). Evaluation of shear and tensile bridging characteristics of PVA fibers based on bridging law, Strain-Hardening Cement-Based Composites, SHCC4, RILEM Bookseries 15, pp.88-96, 2017.

[1-41] Ozu, Y., Miyaguchi, M., & Kanakubo, T. (2018). Modeling of bridging law for PVA fiber-reinforced cementitious composite considering fiber orientation. J. Civ. Eng. Archit, 12, 651-661.

[1-42] Sunaga, D., Namiki, K., & Kanakubo, T. (2020). Crack width evaluation of fiber-reinforced cementitious composite considering interaction between deformed steel rebar. Construction and Building Materials, 261, 119968.

[1-43] Curosu, I., Muja, E., Ismailov, M., Ahmed, A. H., Liebscher, M., & Mechtcherine, V. (2022). An experimental-analytical scale-linking study on the crack-bridging mechanisms in different types of SHCC in dependence on fiber orientation. Cement and Concrete Research, 152, 106650.

[1-44] Liu, Y., Wu, B., & Qiu, J. (2023). A new fiber-bridging constitutive model for quantifying the matrix carbonation and fiber-to-matrix interface healing in PVA fiber-reinforced SHCC. Construction and Building Materials, 399, 132548.

[1-45] Shiferaw, H. N., Abrha, S. F., Kanakubo, T., Sivasubramanian, M. V., & Singh, S. B. (2024). Influence of fiber dimensions on bridging performance of polyvinyl alcohol fiber-reinforced cementitious composite (PVA-FRCC). Fibers, 12(8), 70.

[1-46] Jakubovskis, R., Kupliauskas, R., Rimkus, A., & Gribniak, V. (2018). Application of FE approach to deformation analysis of RC elements under direct tension. Struct. Eng. Mech, 68(3), 345-358.

[1-47] Wille, K., El-Tawil, S., & Naaman, A. E. (2014). Properties of strain hardening ultra high performance fiber reinforced concrete (UHP-FRC) under direct tensile loading. Cement and Concrete Composites, 48, 53-66.

[1-48] Van Mier, J. G. M., & Van Vliet, M. R. A. (2002). Uniaxial tension test for the determination of fracture parameters of concrete: state of the art. Engineering Fracture Mechanics, 69(2), 235-247.

[1-49] https://www.webofscience.com/wos/woscc/summary/870aa9f6-a626-45df-8beb-581738ba1671-016da1daaa/item-title-ascending/1

[1-50] Van Mier, J.G.M. and Van Vliet, M.R.A. (2003), "Influence of microstructure of concrete on size/scale effects in tensile fracture", Eng. Fract. Mech., 70(16), 2281-2306.

[1-51] Zhang, Z., Shao, X. D., & Zhu, P. (2020). Direct tensile behaviors of steel-bar reinforced ultra-high performance fiber reinforced concrete: Effects of steel fibers and steel rebars. Construction and Building Materials, 243, 118054.

[1-52] Benson, S. D. P., & Karihaloo, B. L. (2005). CARDIFRC®–Development and mechanical properties. Part III: Uniaxial tensile response and other mechanical properties. Magazine of Concrete Research, 57(8), 433-443.

[1-53] Huang, T., Zhang, Y. X., Lo, S. R., & Lee, C. K. (2017). Experimental study on crack bridging in engineered cementitious composites under fatigue tensile loading. Construction and Building Materials, 154, 167-175.

[1-54] Barragán, B. E., Gettu, R., Zerbino, R. L., & Martín, M. A. (2001). The uniaxial tensile test for steel fibre reinforced concrete.

[1-55] T.C. Rilem, "162-TDF (2001) Test and design methods for steel fibre reinforced concrete-Uni-axial tension test for steel fibre reinforced concrete," Mater Struct, vol. 34, no. 235, pp. 3–6.

[1-56] Broukalova, I. (2011). Behaviour of a Member with Combined Reinforcement in Tension. In T. Dvorsky, A. Kohoutkova, & V. Vytlacilova (Eds.), FIBRE CONCRETE 2011: TECHNOLOGY, DESIGN, APPLICATION (pp. 321-+). Czech Technical Univ Prague.

[1-57] Kwan, A. K. H., & Chu, S. H. (2018). Direct tension behaviour of steel fibre reinforced concrete measured by a new test method. Engineering Structures, 176, 324-336.

[1-58] Paegle, I., & Fischer, G. (2013). Evaluation of test methods used to characterize fiber reinforced cementitious composites. In International Conference „Innovative Materials, Structures and Technologies" 2013 (pp. 122-128).

[1-59] Look, K., & Mark, P. (2022). Steel fiber reinforced concrete tensile testing with eliminated lateral wall effect. Structural Concrete, 23(6), 3483-3496.

[1-60] Kanakubo, T. (2006). Tensile characteristics evaluation method for ductile fiber-reinforced cementitious composites. Journal of Advanced Concrete Technology, 4(1), 3-17.

[1-61] Douglas, K. S., & Billington, S. L. (2011). Strain rate dependence of HPFRCC cylinders in monotonic tension. Materials and structures, 44(1), 391-404.

[1-62] Heravi, A. A., Curosu, I., & Mechtcherine, V. (2020). A gravity-driven split Hopkinson tension bar for investigating quasi-ductile and strain-hardening cement-based composites under tensile impact loading. Cement and Concrete Composites, 105, 103430.

[1-63] Shen, X., & Brühwiler, E. (2020). Influence of local fiber distribution on tensile behavior of strain hardening UHPFRC using NDT and DIC. Cement and Concrete Research, 132, 106042.

[1-64] Tu, L., Zhao, H., Tan, C., Cao, J., Yi, D., & Qiu, M. (2025). Prediction of tensile strain capacity of ultra-high performance concrete based on crack characteristics. Construction and[] Rokugo, K., Uchida, Y., Moriyama, M., & Lim, S. (2007, June). Direct tensile behavior and size effect of strain-hardening fiber-reinforced cement-based composites (SHCC). In Proceedings of the 6th International Conference on Fracture Mechanics of Concrete and Concrete Structures, Catania, Italy, Jun (pp. 17-22).

[1-65] Cattaneo S, Rosati G (1999) Effect of different boundary conditions in direct tensile tests: experimental results. Mag Concr Res 51:365–374. https://doi.org/10.1680/macr.1999.51.5.365

[1-66] Cattaneo S, Rosati G, Banthia N (2009) A simple model to explain the effect of different boundary conditions in direct tensile tests. Constr Build Mater 23(1):129–137. https://doi.org/10.1016/j.conbuildmat.2008.01.013

[1-67] Vervuurt A, Van Mier JGM (1994) Experimental and numerical analysis of boundary effects in uniaxial tensile tests. WIT Trans Eng Sci. https://doi.org/10.1007/s10338-021-00304-1

[1-68] Samanthula, R., Gettu, R., Paul, S. et al. Effect of the end conditions on the response of glass textile reinforced cementitious composites under uniaxial tension. Mater Struct 57, 140 (2024). https://doi.org/10.1617/s11527-024-02413-y

[1-69] Barragán BE, Gettu R, Martín MA, Zerbino RL (2003) Uniaxial tension test for steel fibre reinforced concrete - a parametric study. Cem Concr Compos 25:767–777. https://doi.org/10.1016/S0958-9465(02)00096-3

[1-70] Luo, X., Zhang, S., Li, A., Yang, X., & Liang, Z. (2023). Steel rebar effect on tensile and cracking behavior of UHPFRC based on direct tensile tests and digital image correlation. Cement and Concrete Composites, 137, 104940.

[1-71] Rokugo, K., Uchida, Y., Moriyama, M., & Lim, S. (2007, June). Direct tensile behavior

and size effect of strain-hardening fiber-reinforced cement-based composites (SHCC). In Proceedings of the 6th International Conference on Fracture Mechanics of Concrete and Concrete Structures, Catania, Italy, Jun (pp. 17-22).

[1-72] Yokota, H., Rokugo, K., & Sakata, N. (2008, June). JSCE recommendations for design and construction of high performance fiber reinforced cement composite with multiple fine cracks. In High performance fiber reinforced cement composites (Vol. 2, pp. 761-770). Springer Tokyo, Japan.

[1-73] Amin, A., Markić, T., Gilbert, R. I., & Kaufmann, W. (2018). Effect of the boundary conditions on the Australian uniaxial tension test for softening steel fibre reinforced concrete. Construction and Building Materials, 184, 215-228.

[1-74] Faustmann, S., Kronau, M., & Fischer, O. (2024). Direct tensile tests on steel fiber reinforced concrete with focus on wall effect and fiber orientation. Materials and Structures, 57(8), 185.

[1-75] Gary, G. (2014). Testing with bars from dynamic to quasi-static. In Constitutive Relations under Impact Loadings: Experiments, Theoretical and Numerical Aspects (pp. 1-58). Vienna: Springer Vienna.

[1-76] Benson, S. D. P., & Karihaloo, B. L. (2005). CARDIFRC®–Development and mechanical properties. Part III: Uniaxial tensile response and other mechanical properties. Magazine of Concrete Research, 57(8), 433-443.

[1-77] Pereira, E. N. B., Fischer, G., Barros, J. A., & Lepech, M. (2010). Crack formation and tensile stress-crack opening behavior of fiber reinforced cementitious composites (FRCC).

[1-78] Mudadu, A., Tiberti, G., Germano, F., Plizzari, G. A., & Morbi, A. (2018). The effect of fiber orientation on the post-cracking behavior of steel fiber reinforced concrete under bending and uniaxial tensile tests. Cement and concrete composites, 93, 274-288.

[1-79] Roth, M. J., Eamon, C. D., Slawson, T. R., Tonyan, T. D., & Dubey, A. (2010). Ultra-High-Strength, Glass Fiber-Reinforced Concrete: Mechanical Behavior and Numerical Modeling. ACI materials journal, 107(2)

[1-80] Buratti, N., & Mazzotti, C. (2016, December). Creep testing methodologies and results interpretation. In Creep Behaviour in Cracked Sections of Fibre Reinforced Concrete: Proceedings of the International RILEM Workshop FRC-CREEP 2016 (pp. 13-24). Dordrecht: Springer Netherlands.

[1-81] Fu, B., Wei, Z. H., Xu, G. T., Zou, Q. Q., Yang, J. L., & Yu, T. (2025). Tensile behavior of concrete reinforced with macro fibers processed from waste GFRP composites. Construction and Building Materials, 460, 139617.

[1-82] Jones, E. M., & Iadicola, M. A. (2018). A good practices guide for digital image correlation. International Digital Image Correlation Society, 10, 1-110.

[1-83] Jun, P., & Mechtcherine, V. (2010). Behaviour of strain-hardening cement-based composites (SHCC) under monotonic and cyclic tensile loading: part 1–experimental investigations. Cement and Concrete Composites, 32(10), 801-809.

[1-84] Liu, F., Ding, W., & Qiao, Y. (2020). Experimental investigation on the tensile behavior of hybrid steel-PVA fiber reinforced concrete containing fly ash and slag powder. Construction and Building Materials, 241, 118000.

[1-85] Orosz, K., Blanksvärd, T., Täljsten, B., & Fischer, G. (2013). Crack development and deformation behaviour of CFRP-reinforced mortars. Nordic Concrete Research, 48, 49-69.

[1-86] Samanthula, R., Gettu, R., Paul, S. et al. Effect of the end conditions on the response of glass textile reinforced cementitious composites under uniaxial tension. Mater Struct 57, 140 (2024). https://doi.org/10.1617/s11527-024-02413-y

Chapter 2 Influence of placing thickness on fiber orientation and bridging law of FRCC

2.1 Introduction

Fiber reinforced cementitious composite (FRCC) is a kind of hydraulic cementitious material in which a certain volume fraction of short fibers such as PVA or steel fiber is mixed into mortar or concrete. In recent years, many studies on FRCC have been carried out because the tensile and bending performance of cementitious composite can be improved by the bridging fibers after first cracking, which provides a good tensile strain or deflection hardening and ductile performance. Some previous studies reported that this enhancement by bridging fiber is strongly affected by the fiber orientation intensity in the matrix [2-1]. The fiber orientation intensity is influenced by a lot of factors such as casting directions, flow and formwork geometry [2-2]. This study mainly focuses on the effect of different placing thicknesses on fiber orientation and bridging law of FRCC using the visualization simulation which is introduced as following chapter.

2.2 Visualization simulation of placing thickness on fiber orientation

2.2.1 Materials and simulation method for test

The black-colored nylon fiber is used for visualization simulation to observe each fiber angle easily. The dimensions of nylon fiber used in this study are listed in Table 2-1. In order to visualize the orientation distribution of fibers in the molds made by acrylic plates, a transparent sodium silicate solution which has high viscosity and usually called water glass is adopted as the matrix. The placing thickness here is defined as the thickness of each layer of target cementitious matrix in the height direction (z-axis direction in Figure 2-1 when casting. For example, in Figure 2-1, in order to make the experiment comparable, when the thickness was chosen to be 10 mm, the specimen should be casted 10 layers along the height direction and placing thickness of 33 mm should be 3 layers since the standard cross-section is chosen to be 100 × 100 mm. The volume fraction of nylon fiber is set to be 0.05% to distinguish each fiber easily.

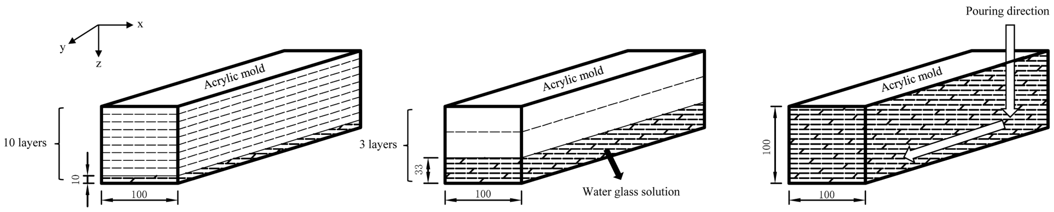

Figure 2-1 The instruction of different placing thickness in visualization simulation (unit: mm)

Table 2-1 Dimension of nylon fiber

Density (g/cm^3)	Length (mm)	Diameter (mm)	Tensile strength (MPa)
1.14	12	0.24	65

The water glass solution containing nylon fibers is poured into three identical molds along the horizontal casting direction as shown in Figure 2-1. Due to the compatibility of the solution, the pouring is stopped when the placing thickness of the water glass solution reached 10 mm, 33 mm and 100 mm respectively in the molds, and the fiber angle distribution of the remaining layers was considered to be the same as this bottom layer. The rheology of mortar matrix before mixing the fiber has been inspected using the flow time based on the test method for flowability of grout measured by the funnel. The flow time of water glass is controlled by adding pure water and the solution temperature in an effort to attain the same flow time of the target mortar matrix. After pouring, the x-y and x-z plane photos of the specimens are taken by digital camera.

2.2.2 Image processing and statistics of fiber distribution

Image analysis is conducted to obtain the fiber distribution as following procedures. Firstly, the photo captured by the camera is cropped to include the central part of 100 × 100 mm region as shown in Figure 2-2a. Secondly, the photo is converted to black and white after a threshold was determined (Figure 2-2b). Thirdly, an approximation line is placed at the location of each fiber. (Figure 2-2c) Finally, the projected lengths of the approximation line in the horizontal and vertical directions are recorded to calculate the angle of the fiber. The fiber angle is defined as the angle between the approximation line and the x-axis and ranges from − 90 to +90°. The relative frequency of fiber angle in every 5° can be calculated.

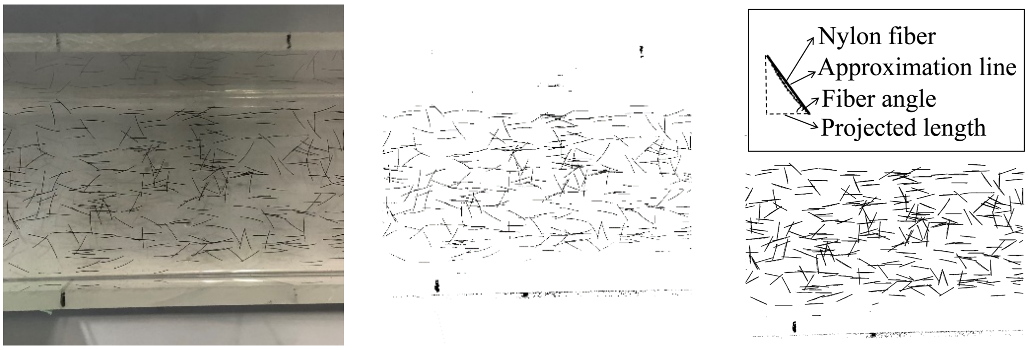

(a) (b) (c)

Figure 2-2 Process of image analysis (10 mm thickness – x-y plane)

After the image analysis and fiber angle calculation, the quantitative statistics of fiber orientation distribution was conducted. Kanakubo et al. [2-2] has proposed a probability density function (PDF) using the elliptic function. The fiber orientation distribution is determined by the orientation intensity k (ratio of the two radii of elliptic function) and principal angle θ_r (argument of one radius of elliptic function), which can be both calculated by the elliptic function. The histogram of fiber angle and calculation result of orientation intensity k and principal angle θ_r on x-z/x-y plane of each placing thickness are shown in Figure 2-3.

Figure 2-3a shows that, as for x-z plane, the relative frequency of placing thickness of 10mm and 33mm on the range of fiber angle around 0° (y-axis direction) are much larger which means the fiber angles are mostly around this range. The orientation intensity k of placing thickness of 10 mm and 33 mm are much larger than that of placing thickness of 100 mm, which indicates the fibers show a great directional orientation toward the principal orientation angle for the former two placing thicknesses. As for x-y plane in Figure 2-3b, except that the condition of the placing thickness of 10 mm is the same as the previous, the relative frequency distribution of the placing thickness of 33 mm and 100 mm is relatively average and the k values are close to 1.0, which means that the fiber angles of these two specimens are close to randomly distributed.

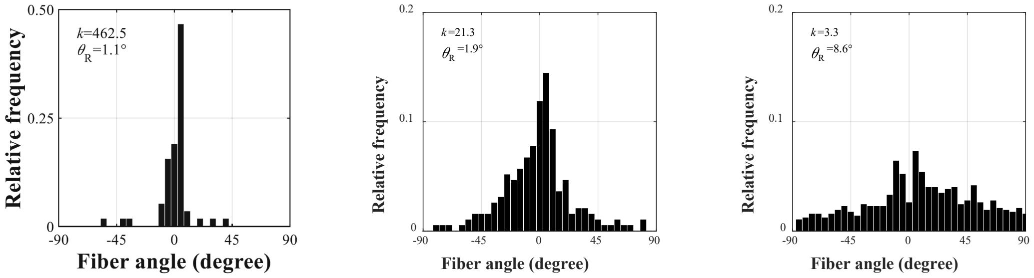

10 mm 33 mm 100 mm

(a) x-z plane

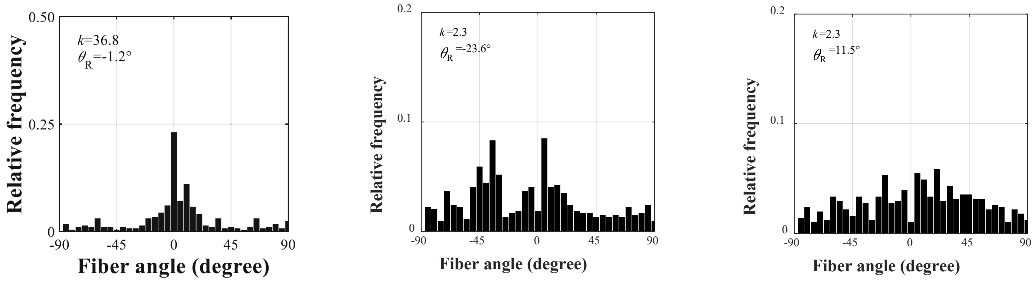

10 mm 33 mm 100 mm

(b) x-y plane

Figure 2-3 All fiber angle histogram

2.3 Image processing and statistics of fiber distribution

2.3.1 Calculation of bridging law

In this section, the calculation of bridging law and section analysis using the models of bridging law are conducted. The target FRCC is PVA-FRCC investigated in the previous study with the fiber volume fraction of 2% [2-1]. The fiber orientation intensity employed in the calculation is assumed to be the same values obtained from the visualization simulation in the former section for each target thickness. And in this chapter, due to the fiber orientation intensity k of x-z plane is over 100, the specimen of placing thickness of 10 mm is not considered in the calculation. The bridging law is described by the relationship of tensile stress and crack-width. Kanakubo et al. [2-2] proposed a tri-linear model of the individual fiber for bridging law considering the effect of fiber orientation, which uses the characteristic points in calculating bridging laws considering the corresponding phenomena of the individual fiber pullout properties. The values and instructions of characteristic points in calculating bridging laws are listed in Table 2-2 and the calculation result of bridging law is shown in Figure 2-4.

Table 2-2 Parameters for calculation of bridging law [2-1]

Calculation parameter	**Input value**
Fiber length, l_f	12 mm
Fiber volume fraction, V_f	2.0%
Fiber diameter, d_f	0.10 mm
Snubbing coefficient, f	0.5
Fiber effective strength	569 MPa
First peak load, P_a	1.5 N
Crack width at P_a, w_a	0.2 mm
Maximum load, P_{max}	3.0 N
Crack width at P_{max}, w_{max}	0.45 mm
Fiber strength reduction factor, f'	0.3

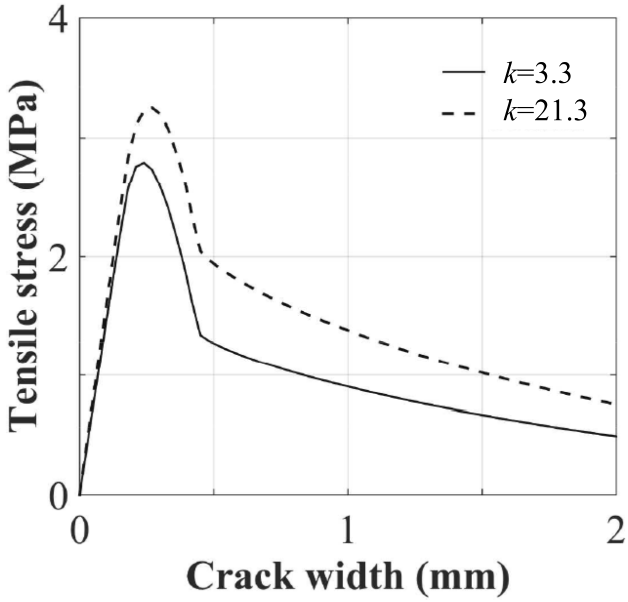

Figure 2-4 Calculated bridging law of different orientation intensity

Figure 2-4 shows that the bridging law of different orientation intensity all contain a stress rising branch up to the maximum at first, followed by a softening branch with a larger absolute value of the slope and finally a gentle softening branch that tends to zero. As for the value of maximum tensile stress, the bridging law for the orientation intensity of 3.3 is larger than that for the orientation intensity of 21.3.

2.3.2 Section analysis

The section analysis based on the tri-linear model of bridging law is conducted to evaluate the bending performance of the specimens using three placing thicknesses for same cross-section (100 mm × 100 mm). Figure 2-5 shows the whole model of stress-strain relationship including the compression side. The stress-strain model of the compression side is assumed to be a parabola model and the tensile side is the tri-linear model which is derived from bridging law model divided by the target length (=100 mm). The section analysis also complies with the plane-cross section assumption. The section analysis is approached by an approximate method as the following steps. Firstly, the cross-section is divided into a finite number of identical elongated elements from the height direction and an arbitrary curvature was given. Secondly, the strain of each element in cross-section is calculated from linear distribution of strain and stress of each element can be obtained from the stress-strain model in Figure 2-5. Finally, neutral axis satisfying equilibrium condition and bending moment is obtained. The values of parameters in the model are expressed as a function of the orientation intensity k to simplify the modeling of the bridging law used for section analysis, which are listed in Table 2-3 as Ozu et al. [2-1] proposed. For simplification, the k value of each specimen used for calculation is the average k value of the x-z plane and x-y plane.

As revealed in Figure 2-6, the bending moments of all orientation intensity first increase and then decrease with the increase of curvature. For the maximum bending moment, the value of the specimen with a orientation intensity of 21.3 mm is the largest, followed by the orientation intensity of 3.3. That is, a larger orientation intensity and smaller placing thickness can effectively improve the flexural performance of FRCC.

Table 2-3 Parameters for section analysis [2-1]

Calculation parameter	**Input value**
Compressive strength, σ_c	35 MPa
Tensile stress at first snapping point, σ_{cr}	$2.0 \times k^{0.30}$ MPa
Tensile stress at second snapping point, σ_t	$0.60 \times k^{0.73}$ MPa
Compressive strain at σ_c, ε_c	0.005
Tensile strain at first snapping point, ε_{cr}	$0.20 \times k^{0.18}/100$ mm
Tensile strain at second snapping point, ε_t	0.0045
Tensile strain at zero stress, ε_u	0.06

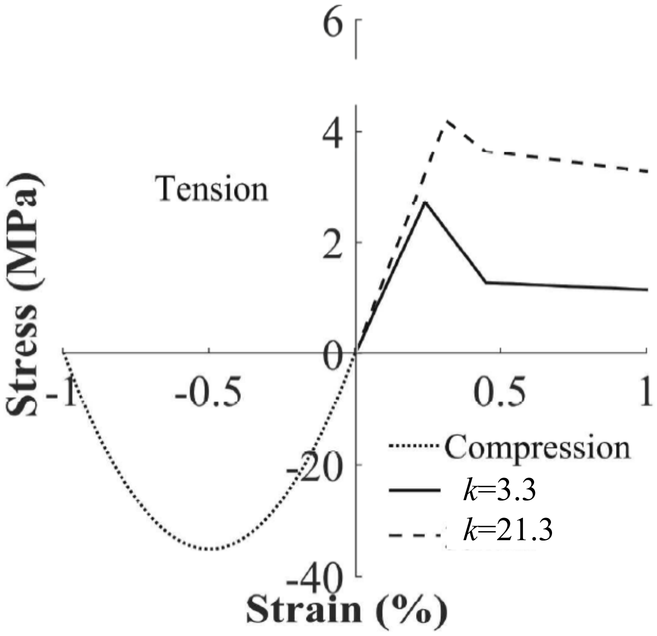

Figure 2-5 The stress-strain model used for cross-section analysis

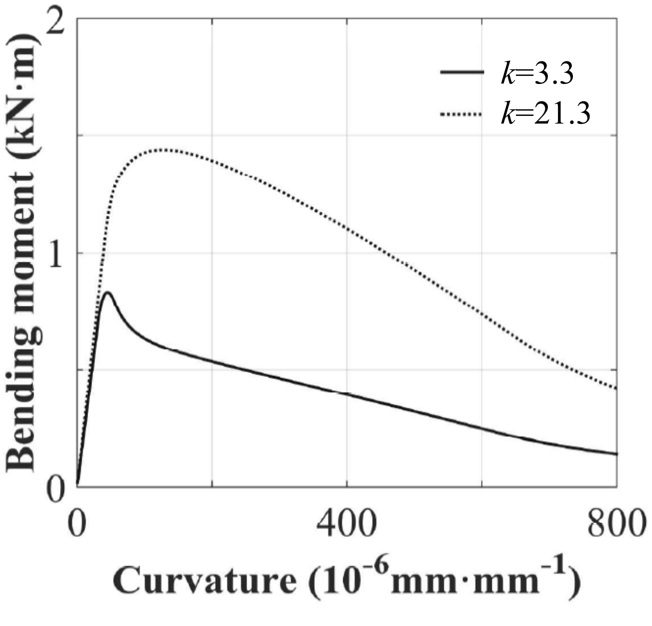

Figure 2-6 Bending moment – curvature for different orientation intensity

2.4 Summary

In this study, the visualization simulation using the water glass is conducted to evaluate the influence of placing thickness on fiber orientation distribution and bridging law. The image analysis shows that a smaller placing thickness leads to a greater fiber orientation intensity, which is one of the significant factors on the bridging law of FRCC. From the calculation results of the bridging law, a smaller placing thickness leads to a higher tensile stress due to the centralization of the fiber angles. Based on the simplified tri-linear stress-strain model of bridging law, section analysis was conducted to give strong evidence on that a smaller placing thickness can effectively improve the flexural performance of FRCC.

Reference

[2-1] Ozu, Y., Miyaguchi, M., Kanakubo, T.: Modeling of bridging law for PVA fiber-reinforced cementitious composite considering fiber orientation. J. Civil Eng. Archit. 12(9), 651–661 (2018)

[2-2] Kanakubo, T., Miyaguchi, M., Asano, K.: Influence of fiber orientation on bridging performance of polyvinyl alcohol fiber-reinforced cementitious composite. ACI Mater. J. 113(2), 131–141 (2016)

Chapter 3 Flexural Characteristics of Functionally Layered FRCC with PVA Fibers

3.1 Introduction

Conventional fiber-reinforced cementitious composites (FRCCs), which adopt a certain volume fraction of synthetic or metallic fibers in cementitious-based materials, have been widely employed in various infrastructure and building facilities such as tunnel lining, bridge decks, and wall panels [3-1,3-2]. Since the crack bridging performance of the mixed fibers can effectively enhance the flexural and durability performance whilst improving the inherent brittleness of the cementitious structure after the first crack development [3-3,3-4], a number of researches [3-5~3-8] have been devoted to assess and evaluate the mechanical properties of FRCCs.

It is reported that multiple factors, which include the casting directions, flow, fiber orientation, and formwork geometry, etc. [3-9], affect the strain or deflection hardening and ductile performance. Fiber orientation and distribution, which can directly affect the bridging performance of FRCCs, are considered to be two of the most significant influential factors due to the high viscosity and self-consolidating properties of the cementitious matrix. Krenchel [3-10] attempted to apply a coupled parameter of the orientation and distribution of the fibers from a wider perspective than mere particular cases, which allows for a better understanding of the fracture results. Laranjeira [3-11] proposed a parametric study and engineered expressions based on the mechanical pull-out properties and orientations of the steel fibers. It should be pointed out that the fiber orientation changes at random from 2-D to 3-D due to the dimensions of the specimen [3-12]. Kanakubo et al. (2016) [3-13] introduced an elliptic function to quantitatively evaluate the fiber o-rientation intensity, which reflects the orientation tendency of fibers, and investigated the influence of casting direction on fiber orientation distribution. Duque and Graybeal [3-14] discussed and validated the anisotropy in the fiber orientation distribution and the tensile mechanical properties as a consequence of the casting process and the flow pattern. They proposed a fiber orientation factor considering the fiber orientation distribution impact on the design methodologies for ultra-high performance fiber reinforced concrete (UHPFRC). Kang and Kim [3-15] used the image analysis process and bending tests to confirm that the fiber orientation distribution has a strong impact on the deflection hardening behavior in bending using the measured fiber orientation distributions for two different flexural performances.

Functionally layered materials, including functionally graded materials, are new types of composite materials that improve the deficiency of individual material properties and take full advantage of each material by a specific process. These kinds of composite materials have undergone a series of materials and emerging structural developments after the concept introduction for industrial applications such as in the aerospace, automotive, and biomedical fields [3-16~3-18]. Some studies [3-19~3-23] have applied the concept of a functional gradient to the field of cementitious structures in order to maximize the rational application of the mechanical properties while reducing costs and the emission of greenhouse gases. Torelli and Lees [3-24] proposed an original fresh-on-fresh casting method to generate functionally layered concrete sections composed of an external U-shaped durability layer of low porosity concrete and a rectangular lightweight bulk core section, which aimed at minimizing the use of cement and to reduce the self-weight of precast concrete beams. Dias et al. (2010) [3-25] employed the thermogravimetric analysis to assess fiber distribution and four-point bending tests to evaluate the mechanical performance of both conventional and graded composites. Lai et al. (2021) [3-26] focused on the effect of high-speed penetration to explosion resistance of the functionally graded cementitious composite and proposed the improved empirical formulas for penetration, explosion, and the coupling of penetration and explosion, respectively. Bao et al. (2023) [3-27] optimized the design of functionally graded ultra-high performance cementitious composite (FGUHPCC) by using a numerical simulation program named RFPA3D and investigated the flexural behavior of FGUHPCC. Kanakubo and Koba [3-28] investigated the flexural characteristics of functionally graded fiber-reinforced cementitious composite (FG-FRCC) concerning the fiber volume fraction varying in layers and the layered effect in bending specimens.

The layered FRCC, in which the fibers tend to show a 2-D orientation, has the possibility to maximize the bridging effect of the fibers, and leads to the higher tensile performance and durability of the FRCC. It is considered that the 2-D orientation of fibers can be generated easily if the thickness of the layer becomes smaller than the length of dispersed fibers. The main purpose of this study is to try to fabricate the functionally layered fiber-reinforced cementitious composite (FL-FRCC) and investigate its characteristics through evaluating the bending test and the section analysis. To perform the section analysis, a tensile stress–strain model is required. This study also aims to propose a tensile stress–strain model of FRCC with wider applicability based on the bridging law (tensile stress–crack width relationship) and fiber orientation. The bridging law of 2-D oriented FRCC can be represented by the proposed model. The target fibers are polyvinyl alcohol (PVA) fibers, in which the bridging law has been studied by authors [3-13]. This previous study has described the effect of fiber orientation on the bridging law using the fiber orientation intensity, k. The random orientation of fibers is given by $k = 1$. When the value of k is larger than 1, fibers tend to orient toward the principal direction. In the case of a completely one-directional orientation, k is represented by infinite. In the range of k from 0.5 to 6, good adaptability has been confirmed between the calculated bridging law and the uniaxial tension test results in this previous study.

3.2 Modification of the Bridging Law for PVA-FRCC

The authors have conducted a previous study on a visualization simulation experiment using a water–glass solution [3-29]. This previous research mainly focused on the influence of the placing thickness on fiber orientation distribution and the bridging law, which leads to the conclusion that a smaller placing thickness can effectively improve the bending performance of the FRCC. Figure 3-1 shows examples of the visualization simulation in the case of a 10 mm placing thickness. The black nylon fibers are 12 mm in length and 0.24 mm in diameter, which can be easily identified in the transparent water glass where a solution is applied in the visualization simulation experiment. It has been recognized that the fibers strongly tend to orientate in the axial direction (y-axis) in the y–z plane. The histograms for a placing thickness of 10 mm were generated by image progress and statistical counting, as shown in Figure 3-2. The values for the fiber orientation intensity, k, shown in the figures exhibit the results of the regression analysis in the histograms. In this case, the fiber orientation with a placing thickness of 10 mm can be simplified as a 2-D issue, which is considered to be consistent with the situation that nearly all the fibers in the y–z plane in the matrix are in the same orientation.

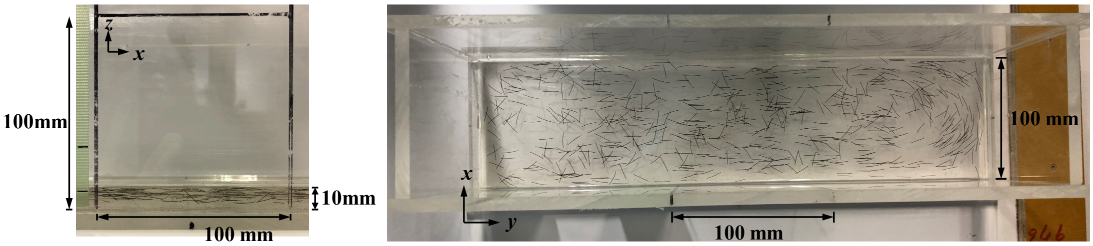

Figure 3-1 Photos of the water–glass simulation, side and up view, with a 10 mm placing thickness [3-29].

Ozu et al. (2018) [3-30] has proposed a tri-linear model, described by Eq. (3-1), that gives the bridging law considering fiber orientation expressed by the function of the fiber orientation intensity, k, based on the calculated bridging law shown in Figure 3-3a. Figure 3-3b illustrates the proposed tri-linear model of the bridging law characterized by the parameters in Eq. (3-1) The proposed model has been built for the range of k from 0 to 10. Using this model extrapolated, the values of tensile stresses become infinite as the value of k becomes infinite. This fact results in the Ozu-proposed model not being able to be adopted for FRCCs with a 10 mm placing thickness, in which the value of k is large enough.

$$\begin{aligned} \sigma_{\max} &= 2.0 \cdot k^{0.30} \\ \sigma_2 &= 0.60 \cdot k^{0.73} \\ \delta_{\max} &= 0.20 \cdot k^{0.18} \end{aligned} \qquad \text{Eq. (3-1)}$$

where, $\sigma_{\max}$: maximum tensile stress, MPa; σ_2 : tensile stress at second snapping point, MPa; $\delta_{\max}$: crack width at $\sigma_{\max}$, mm.

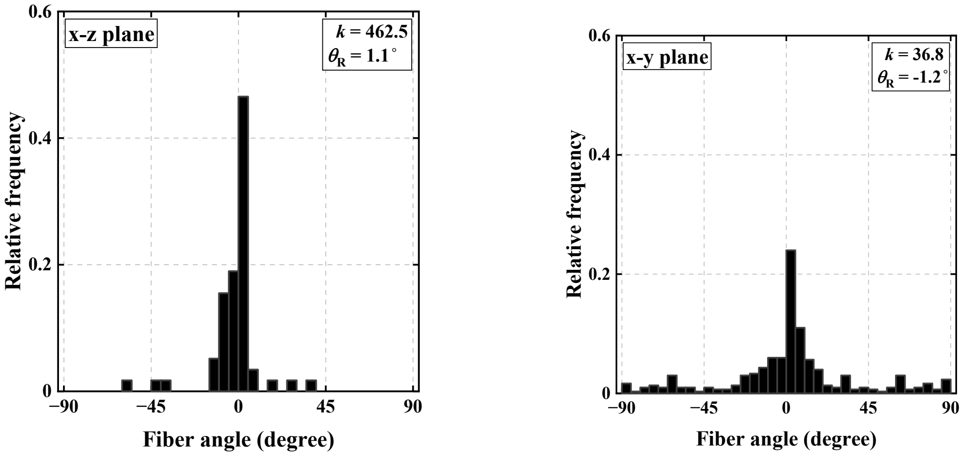

(a) (b)

Figure 3-2 Fiber angle histograms with a placing thickness of 10 mm [3-29]: (**a**) x-z plane; (**b**) x-y plane.

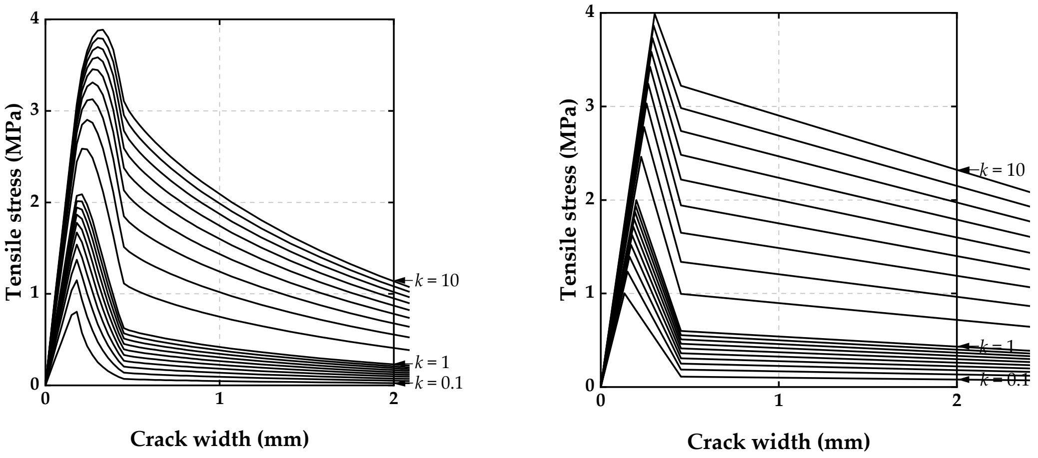

(**a**) (**b**)

Figure 3-3 Calculation result and tri-linear model of the bridging law for PVA-FRCC [3-30]: (**a**) Calculation result; (**b**) Tri-linear model.

The proposed model has been derived by the calculation results of the bridging law, i.e., the summation of the pullout load of all individual fibers crossing the crack [3-13]. This calculation method can give the maximum bridging force if all the fibers in the matrix are in the same orientation. In the previous study [3-13], the maximum pullout load of the individual fiber is given as 3.0 N in the case of target PVA fibers (0.1 mm diameter and 12 mm length). Thus, the maximum tensile stress in the case of a volume fraction of 2% can be given by following Eq. (3-2):

$$\sigma_{\mathrm{max}} = \frac{\sum P_{\mathrm{max}}}{A_{\mathrm{m}}} = \frac{N_{\mathrm{f}} \cdot P_{\mathrm{max}}}{A_{m}} = V_{\mathrm{f}} \cdot \frac{A_{\mathrm{m}}}{A_{\mathrm{f}}} \cdot \frac{P_{\mathrm{max}}}{A_{\mathrm{m}}} = \frac{V_{\mathrm{f}}}{A_{\mathrm{f}}} \cdot P_{\mathrm{max}} = 7.6\ \mathrm{MPa} \qquad \text{Eq. (3-2)}$$

where V_{f} is the fiber volume fraction, 2%; N_{f} is the total number of fibers; A_{f} is the sectional area of the fiber, 0.007854 mm^2; A_{m} is the cross-sectional area of the matrix; and P_{max} is the maximum pullout load of an individual fiber, 3.0 N.

The crack width at the maximum pullout load of an individual fiber is given as 0.45 mm [3-13]. If all the fibers in the matrix are in the same orientation, the crack width at the maximum tensile stress can be given at the same crack width.

Based on the above-mentioned considerations and the same input value as in a previous study [3-29], tri-linear models of maximum tensile stress and crack width at maximum tensile stress are asymptotically approaching 7.6 MPa and 0.45 mm, respectively, when *k* is infinite. Based on the regression analysis with the calculation results, the following formulas are proposed, as shown in Figure 3-4.

$$\begin{aligned} \sigma_{\max} &= -5.4/(k^{0.14}) + 7.6 \\ \sigma_2 &= -6.6/(k^{0.12}) + 7.6 \\ \delta_{\max} &= -1/(k^{0.74} + 3.1) + 0.45 \end{aligned} \qquad \text{Eq. (3-3)}$$

where, $\sigma_{\max}$, σ_2, and $\delta_{\max}$ all refer to the same meaning as in Eq. (3-1).

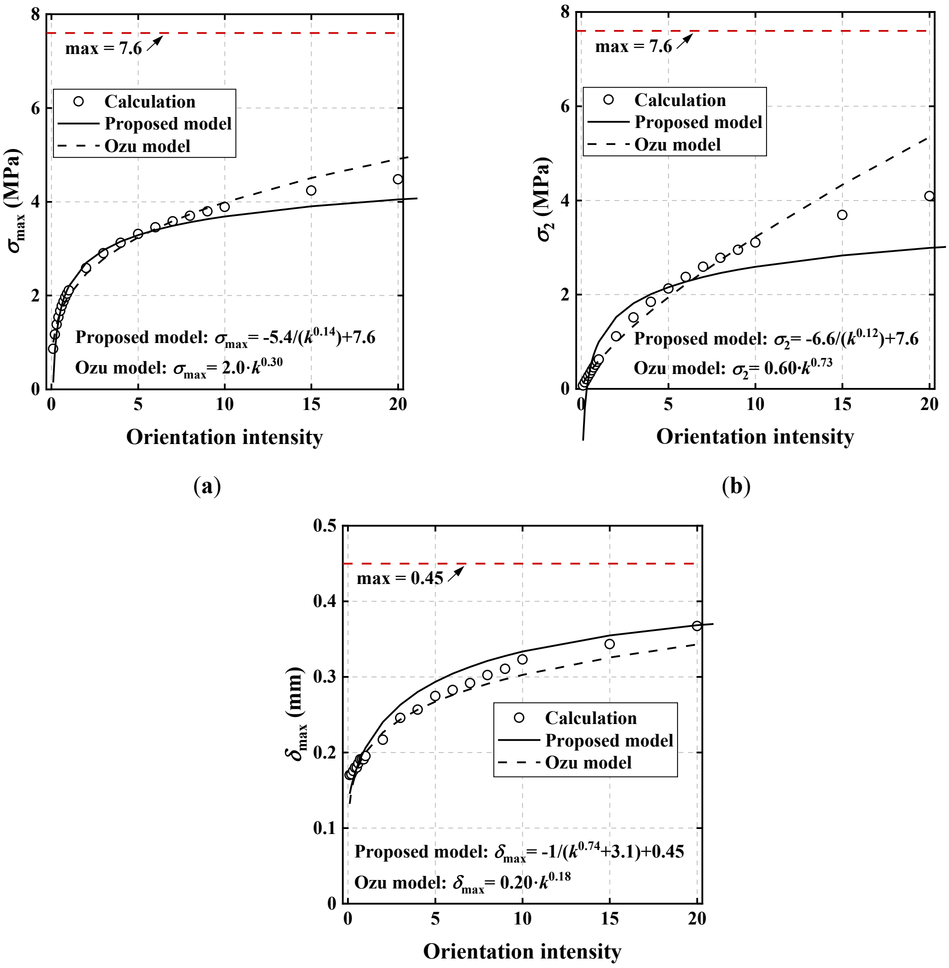

(a)

(b)

(c)

Figure 3-4. Comparison of tensile stresses and crack width in proposed model and Ozu model: (**a**) $\sigma_{\max} - k$; (**b**) $\sigma_2 - k$; (**c**) $\delta_{\max} - k$.

The comparison of the proposed model and previously studied model (Ozu model) [3-30] are shown in Figure 3-5; in the case of a fiber orientation intensity of 2.8 and 250, those are the averaged fiber orientation intensity values between the y–z and x–y planes for a 100 mm placing thickness and a 10 mm one, respectively [3-29].

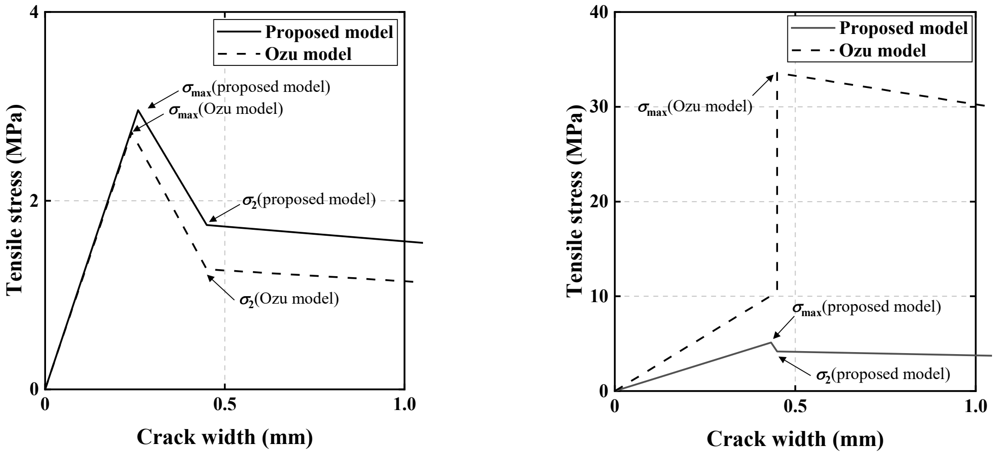

(**a**) $k = 2.8$ (**b**) $k = 250$

Figure 3-5 Comparison of proposed model and the Ozu model: (**a**) $k = 2.8$; (**b**) $k = 250$.

As Figure 3-4 revealed, the fitting result based on the proposed model is slightly better than the Ozu model when the fiber orientation intensity ranges from 0 to 20. As for Figure 3-5, in the case where the fiber orientation intensity, *k,* is 2.8, both the tensile stress–strain relationship derived from the proposed model and the Ozu model are nearly the same, which is consistent with the former fitting effect. However, in the case where the fiber orientation intensity is 250, the proposed model can still effectively describe the relationship between tensile stress and crack width, while the results of Ozu's model lead to a large discrepancy with the actual cognition relationship. By comparing the described results of the models, it can be considered that the proposed model can more accurately describe the bridging law of the fiber orientation intensity and has a wider application range from 0 to infinite.

3.3 Experiment Program

In FL-FRCC, the thickness of each layer is smaller than the fiber length and the fibers tend to show a 2-D orientation, creating a possibility to maximize the bridging effect of the fibers, which leads to a higher tensile performance. In order to verify this consideration, FL-FRCC specimens and homogeneous (Hmg-FRCC) specimens are designed and fabricated per the following instructions.

3.3.1 Materials

The mechanical properties of the PVA fibers utilized in this study are listed in Table 3-1, which are the same with those used in previous studies [3-13,3-29,3-30]. The mixture proportion of FRCC is listed in Table 3-2 and the fiber volume fraction of both

FL-FRCC specimens and Hmg-FRCC specimens are set to 2%. Both the FL-FRCC and Hmg-FRCC specimens follow the same fabrication order as below. Firstly, early-strength cement, fly ash, sand and drying shrinkage reducing agent are added in at one time and mixed for 60 s. Secondly, water and a high-range water reducing agent are added in the mixer. After 180 s of mixing, the first flow time test based on the test method for the flowability of grout for prestressing tendons (JSCE-F 531) [3-31] is then carried out to measure the rheology of the matrix. The second flow time test is conducted after the addition of thickener to increase the viscosity and fluidity of the matrix. The results of the two flow time tests are 15.3 s and 54.5 s, respectively. In order to fully mix the PVA fibers, half of the fibers are added to the mixer for the first mixing of 30 s, and the other half of the fibers are then added to the mixer for 120 s of mixing. Finally, the air content of the FRCC is measured, which result refers to 3.9%.

Table 3-1 Mechanical properties of the PVA fiber applied in this study

Type	Diameter (mm)	Length (mm)	Tensile strength (MPa)	Elastic modulus (GPa)
PVA	0.10	12	1200	28

Table 3-2 Mixture proportion of the FRCC

Water to binder ratio	Sand by binder ratio	Unit weight (kg/m^3)				
		Water	Cement	Fly ash	Sand	PVA fiber
0.39	0.50	380	678	291	484	26

3.3.2 Specimen

The specimen type overview is listed in Table 3-3. Each 400 × 100 × 10 mm FL-FRCC-plate is poured in the same direction. One side of the mold is raised 12 mm to ensure that the FRCC is poured in the same direction under the gravity effect, as shown in Figure 3-6. Individual FL-FRCC plates are cured for two weeks at room environment, and the execution works for the bonding of plates are carried out. Considering the adhesive thicknesses of the layers, every nine of plates are bonded together with epoxy adhesive to make the total height of the whole FL-FRCC specimen around 100 mm. The epoxy adhesive used in this study is made by Mitsubishi Chemical Infratec Co., Ltd. The main properties of the epoxy adhesive provided by the maker are listed in Table 3-4. The main agent and hardener of the epoxy resin are fully mixed at a weight ratio of 2:1. Clamps and a guider are used to tie up and retain the holistic shape and height of the specimen consistent with homogeneous specimen until the epoxy adhesive is tightly bonded with each layer, as shown in Figure 3-7. The spilled epoxy adhesive is scraped off to keep the specimen surface flat. After the fixed formation of the whole FL-FRCC specimen, the height of the specimen was measured, as shown in Figure 3-8, and the results are listed in Table 3-5.

Table 3-3 Specimen type overview.

Specimen type	Dimensions L × W × H (mm)	Number of specimens
FL-FRCC	400 × 100 × 10 × 9 layers	3
Hmg-FRCC	400 × 100 × 100	5

Figure 3-6 Casting of FRCC plates.

Table 3-4 Properties of epoxy adhesive.

	Specific gravity (Hardened product)	Viscosity	Concrete adhesive strength * (N/mm^2)
Test value	1.92	Putty-liked	3.2

* Tested followed “Testing Methods for Paints (JIS K 5400)” [3-32].

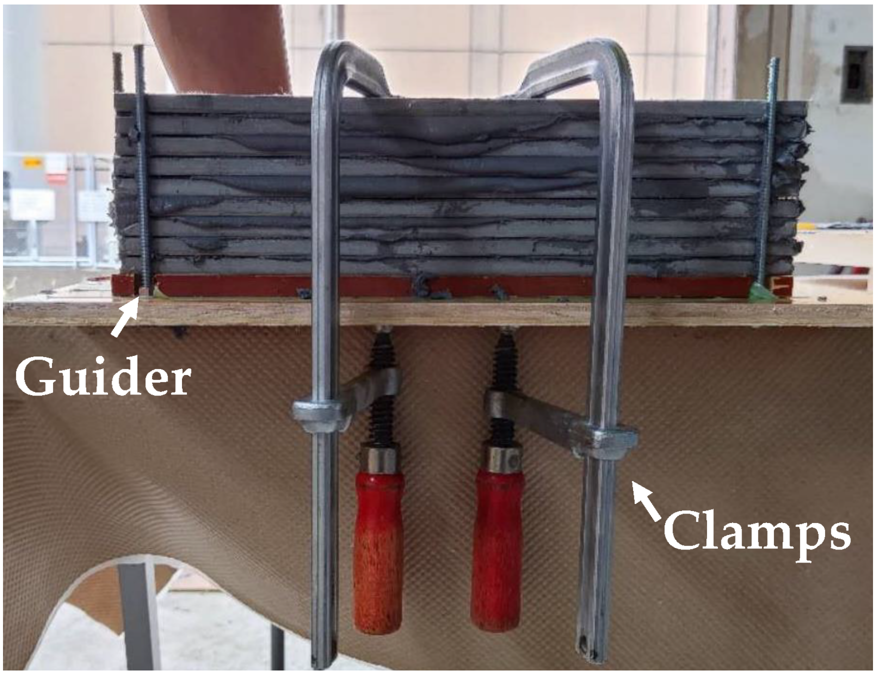

Figure 3-7 Clamps and guider applied to retain the holistic shape.

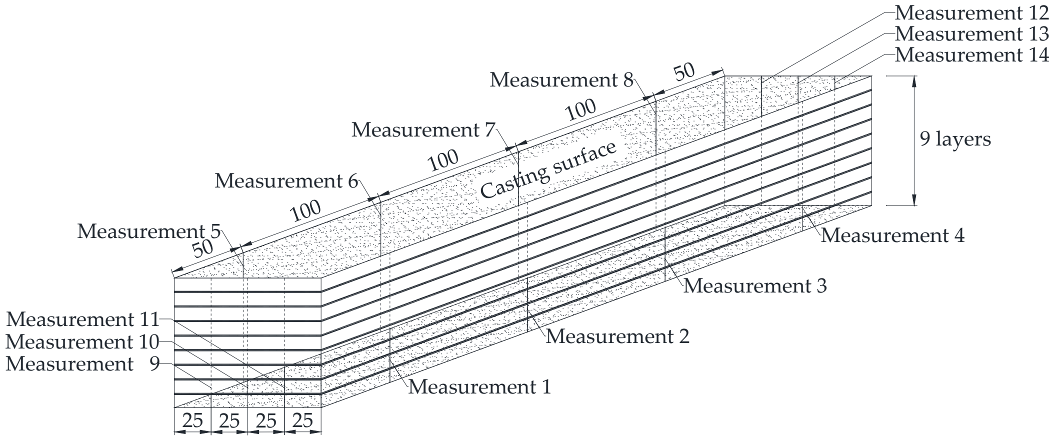

Figure 3-8 Height measuring points of the FL-FRCC specimen.

Table 3-5 Height measuring results of the FL-FRCC specimen.

Specimen No.	Height at measuring point (mm)							Average
	1 8	2 9	3 10	4 11	5 12	6 13	7 14	
1	103.2	100.8	99.2	97.8	105.1	101.6	101.7	100.9
	99.1	97.1	98.0	99.2	104.2	103.1	103.0	
2	100.4	100.7	100.8	99.7	100.2	99.7	101.7	100.0
	99.6	98.8	99.0	99.0	100.0	100.0	100.0	
3	101.8	101.8	101.6	101.3	101.4	101.6	101.8	101.8
	102.6	102.4	102.3	102.6	102.0	101.8	100.5	

Four-point bending tests are conducted to obtain the relationship of the bending moment and curvature following ISO 21914:2019 [3-33] using the universal loading machine. The π-type linear variable displacement transducers (LVDT) are respectively set at 15 mm from the edge of the specimen. All the FL-FRCC and Hmg-FRCC specimens are set on the test platform of the loading machine with the same placing method where the casting surface is kept upside, as shown in Figure 3-9. For compressive strength, Φ100 mm × 200 mm cylinder test pieces are prepared and tested according to the instruction of ISO 1920-4:2020 [3-34]. The result of the average compressive strength is 55.6 MPa.

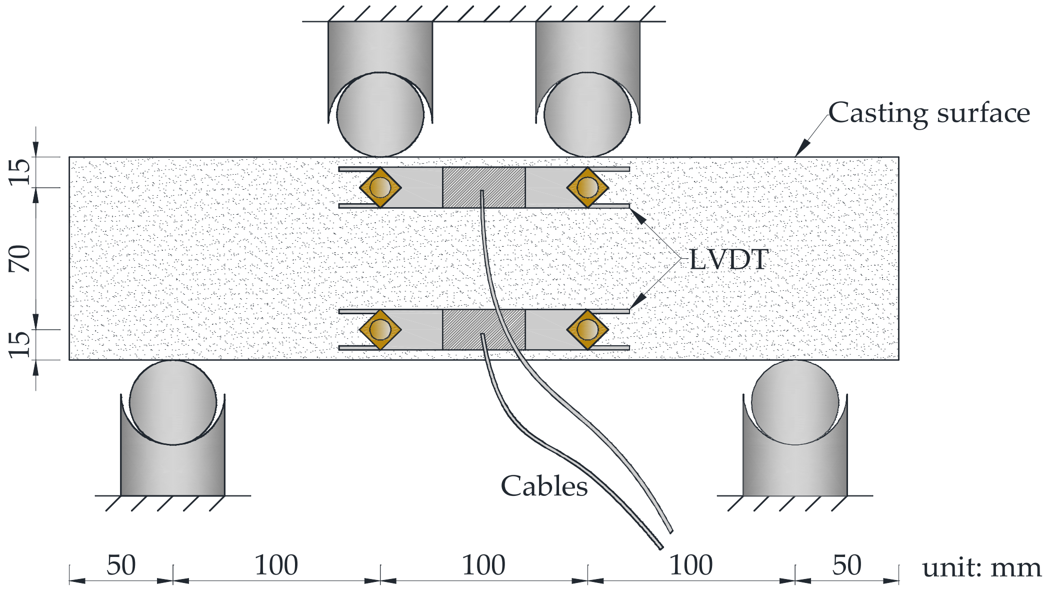

Figure 3-9 Four-point loading configuration.

3.4 Experiment Results

3.4.1 Failure Pattern

Figure 3-10 shows the typical crack development results of the FL-FRCC specimens and Hmg-FRCC specimens after loading. It can be learned from Figure 3-10 that only one crack developed in the middle area of each of the FL-FRCC and Hmg-FRCC specimens. Numerous PVA fibers can be seen on the ruptured section of both specimens.

FL-FRCC	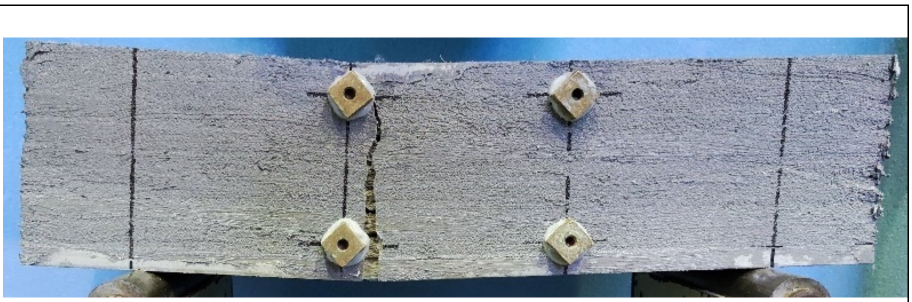
Hmg-FRCC	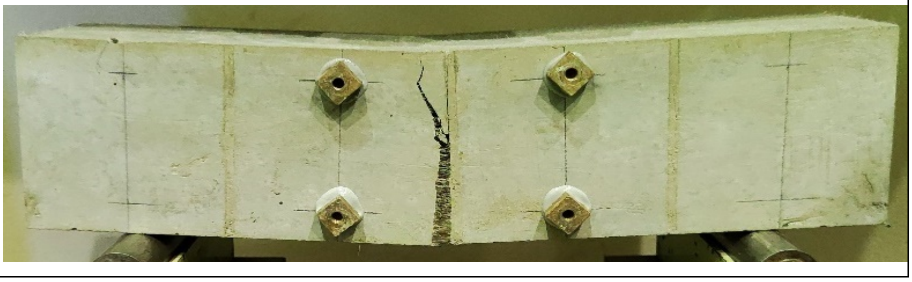

Figure 3-10 Typical failure type of the specimens after loading

3.4.2 Bending Moment: A Curvature Relationship

The relationship between the bending moment and curvature is shown in Figure 3-11. The initial crack of each Hmg-FRCC specimen is observed before it reaches the maximum bending moment. For FL-FRCC specimens, the initial crack of each specimen is observed before reaching the maximum bending moment, but very soon, the FL-FRCC specimens reach the maximum bending moment. For Hmg-FRCC specimens, after reaching the maximum value, the bending moment decreases with the increase in the curvature. This bending moment–curvature relationship tendency also applies to FL-FRCC specimens. However, the curves of FL-FRCC specimens all show a steeper decline phase after reaching the maximum bending moment, which indicated a relative brittleness in this kind of FL-FRCC specimen, while the curve of Hmg-FRCC specimens decreases more slowly with the increase in the curvature. The maximum bending moments of specimens are listed in Table 3-6. The average maximum bending moment of FL-FRCC specimens is 1.62 MPa, which is almost two times that of Hmg-FRCC specimens. This fact indicates that the FL-FRCC specimens could have a larger bending capacity.

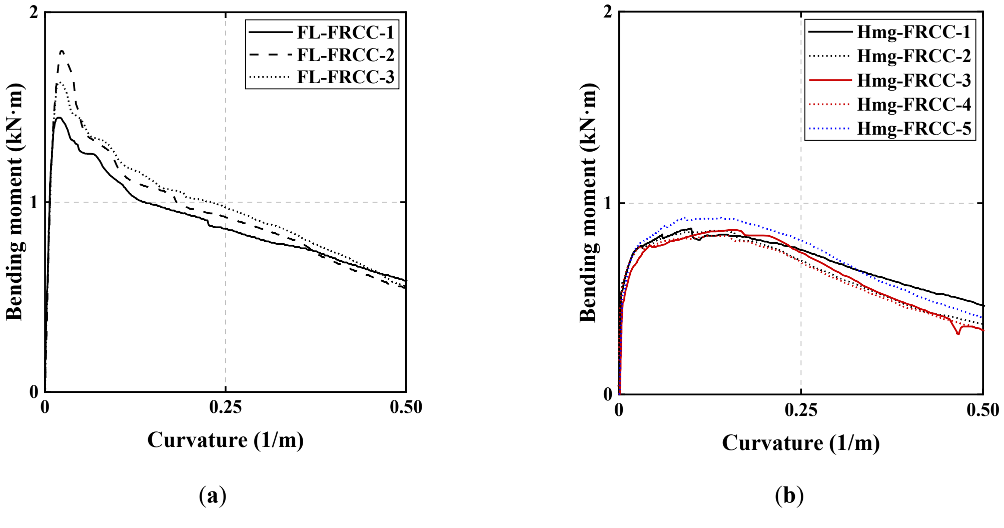

Figure 3-11 Bending moment–curvature curves of the FL-FRCC and Hmg-FRCC specimens: (**a**) FL-FRCC; (**b**) Hmg-FRCC.

Table 3-6 List of maximum bending moments.

Specimen type	**Experiment**				**Section analysis**		**Ratio of experiment to analysis**
	Max. bending moment $_{e}M_{\max}$ **(kN·m)**		**Curvature at** $_{e}M_{\max}$ **(1/m)**	**Absorbed energy (N·m)**	**Max bending moment** $_{a}M_{\max}$ **(kN·m)**	**Curvature at** $_{a}M_{\max}$ **(1/m)**	$_{e}M_{\max} / {}_{a}M_{\mathrm{m}}$
	Avg.	**STDV**	**Avg.**	**Avg.**			
FL-FRCC	1.62	0.176	0.022	47.3	1.66	0.136	0.98
Hmg-FRCC	0.87	0.036	0.119	41.6	0.94	0.048	0.93

3.4.3 Comparison of the Section Analysis and Experiment Results

Section analysis based on the proposed bridging law is conducted to compare with the experiment results. The stress–strain model used in the analysis is shown in Figure 3-12. The proposed bridging law, given by Eq. (3-3) and shown in Figure 3-5, is converted to a tensile stress–strain model as that the crack width is divided by the gauge length of LVDTs, which is equal to the length of the constant moment region. Popovics [3-35] introduced the complete stress–strain models of concrete and mortar, which provided a better fitting effect compared to the experiment, as expressed by Eq. (3-4). Popovics' model is also applied in the compression side of stress–strain model in the section analysis of this study. The compressive strength and strain at the maximum stress are decided as the average results obtained by the compression test described in Section 3.3.2. The coefficient *n* is obtained by the fitting calculation of the compression test results, as shown in Figure 3-13.

$$\frac{\sigma}{\sigma_{\max}} = \frac{\varepsilon}{\varepsilon_{\max}} \cdot \frac{n}{(n-1) + (\varepsilon / \varepsilon_{\max})^{n}} \qquad \text{Eq. (3-4)}$$

where $\sigma_{\max}$ is the compressive strength of the specimen; $\varepsilon_{\max}$ is the strain at maximum stress; and *n* is the coefficient.

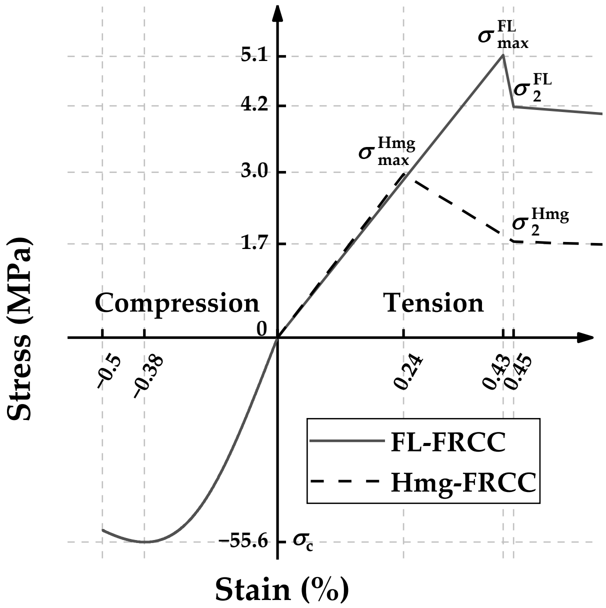

Figure 3-12 Stress–strain models of FL-FRCC and Hmg-FRCC for the section analysis.

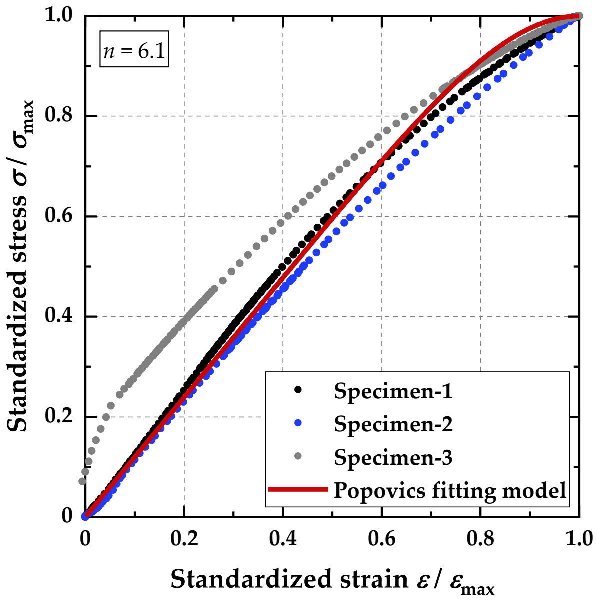

Figure 3-13 Comparison of Popovics' model and the compression test results.

Table 3-6 lists the results of the section analysis comparing the experiment results. It can be seen from the results of the section analysis that the maximum bending moment of FL-FRCC specimens is 1.66 MPa, which is 1.77 times that of Hmg-FRCC specimens. For both FL-FRCC and Hmg-FRCC specimens, it is considered that the section analysis results show a good consistency with the experiment results since the ratio of experiment to analysis is around 1.00, in which the deviation is no more than 10%, especially for FL-FRCC specimens. This fact also verifies that the proposed bridging law in Section 3.2 considers the infinite orientation intensity and shows good adaptability with FL-FRCC specimens.

Curvatures at the maximum bending moment calculated by the section analysis do not show good adaptability with the ones obtained by the experiment. The reasons for that are considered to be that the layered FRCC would cause a chain of fractures in each adjacent layer in the case of FL-FRCC specimens. In the case of Hmg-FRCC specimens, the wide constant moment region around the maximum bending moment leads to the scattering of the curvature at the maximum. On the other hand, the absorbed energy generally refers to the ability of materials to absorb the post-crack energy and can be calculated from the bending moment–rotation angle relationship. In this study, the absorbed energy was calculated from 0 to 0.05 of the rotation angles (equal to a curvature of 0 to 0.50 m^{-1}) and the results are listed in Table 3-6. The experiment results show that the absorbed energy of FL-FRCC specimens is 1.14 times larger than that of Hmg-FRCC specimens, which indicates that FL-FRCC specimens have a larger bending capacity but also an increased relative brittleness compared to the Hmg-FRCC specimens.

The stress distributions in the cross-section at the maximum bending moment are shown in Figure 3-14. For Hmg-FRCC specimens, the maximum bending moment would occur while the tensile stress reaches the maximum at about one-fourth of the cross-section height from the tension edge. As for FL-FRCC specimens, the tensile stress reaches the maximum at approximately half of the cross-section height from the compression edge; thus, it is considered that FL-FRCC specimens can effectively apply the bending capacity of the whole specimen.

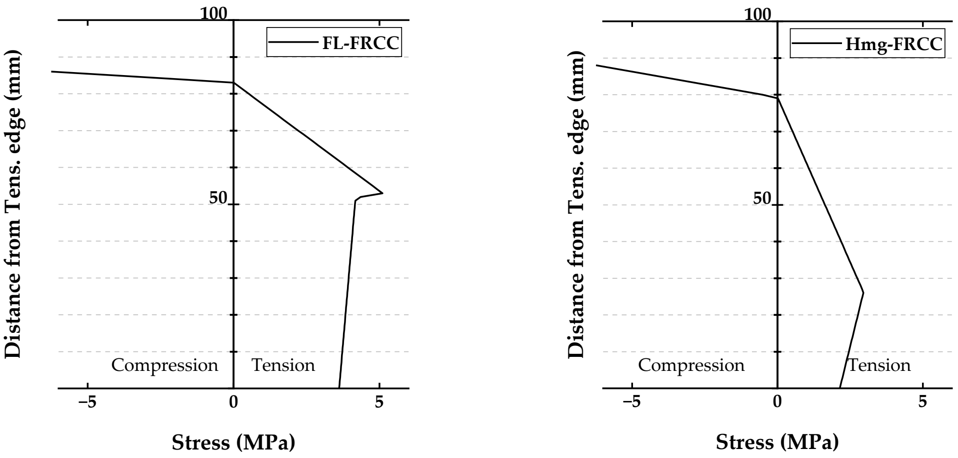

(**a**) (**b**)

Figure 3-14 Stress distribution in the section analysis: (**a**) FL-FRCC; (**b**) Hmg-FRCC.

3.5 Conclusions

Based on the proposed stress–strain model considering the bridging law and the results of the bending tests and section analysis conducted to investigate the flexural characteristics of the FL-FRCC, the following conclusions can be drawn:

(1) Based on the previous visualization simulation results, a bridging law model is proposed with a wider range of fiber orientation intensity applications, including the situation of being infinite. Compared to the Ozu model, the proposed model has proven to have a better fitting and predicting effect;

(2) FL-FRCC specimens, in which the thickness of each layer is smaller than the fiber length and the mixed fibers tend to show a 2-D orientation, are fabricated. Bending tests were conducted and the results show that the average maximum bending moment of FL-FRCC specimens is nearly twice that of the Hmg-FRCC specimens. The bending moment-curvature curves of FL-FRCC specimens shows a steeper decline phase after reaching the maximum bending moment compared to that of Hmg-FRCC specimens. And the absorbed energy of FL-FRCC specimens is also larger than that of Hmg-FRCC specimens. These facts suggest the FL-FRCC specimens can lead to a larger bending capacity and also the relative brittleness compared to the Hmg-FRCC specimens;

(3) Section analysis based on the proposed stress–strain model was conducted. The ratio of the experiment to analysis ranged from 0.93 to 0.98, which can lead to the conclusion that the section analysis shows a good adaptability with the experiment result. Curvatures at the maximum bending moment calculated by the section analysis do not show good adaptability with the ones obtained by the experiment. The reasons for that are considered to be that the layered FRCC would cause a chain of fractures in each adjacent layer in the case of FL-FRCC specimens. In the case of Hmg-FRCC specimens, the wide constant moment region around the maximum bending moment leads to the scattering of the curvature at the maximum;

(4) For FL-FRCC specimens, the tensile stress reaches the maximum at approximately half of the cross-section height from the compression edge; it is considered that FL-FRCC specimens can effectively apply the bending capacity of the whole specimen compared to the Hmg-FRCC specimens.

Reference

[3-1] Li, V. C. (2019). Engineered cementitious composites (ECC): bendable concrete for sustainable and resilient infrastructure. Springer.

[3-2] Rokugo, K., Kanda, T., Kanakubo, T., Fukuyama, H., Uchida, Y., Suwada, H., & Slowik, V. (2013). Strain Hardening Cement Composites: Structural Design and Performance: State-of-the-Art Report of the RILEM Technical Committee 208-HFC, SC3 (pp. 59-66). Berlin/Heidelberg, Germany: Springer.

[3-3] Li, V. C. (2003). On engineered cementitious composites (ECC) a review of the material and its applications. Journal of advanced concrete technology, 1(3), 215-230.

[3-4] Li, V. C. (2007). Progress and applications of engineered cementitious composites.

[3-5] Balaguri, P. N., & Shah, S. P. (1992). Fiber Reinforced Cement Composites, McGrawHill. Inc, Singapore.

[3-6] Zollo, R. F. (1984). Collated fibrillated polypropylene fibers in FRC. Special Publication, 81, 397-410.

[3-7] Naaman, A. E. (1996). High performance fiber reinforced cement composites 2 (HPFRCC 2). In Proceedings of the Second International RILEM Workshop, E&FN SPON..

[3-8] Li, V. C. (2002). Large volume, high ‐ performance applications of fibers in civil engineering. Journal of Applied Polymer Science, 83(3), 660-686.

[3-9] Laranjeira, F., Aguado, A., Molins, C., Grünewald, S., Walraven, J., & Cavalaro, S. (2012). Framework to predict the orientation of fibers in FRC: A novel philosophy. Cement and Concrete Research, 42(6), 752-768.

[3-10] Krenchel, H. (1975). Fibre spacing and specific fibre surface. Fibre reinforced cement and concrete, 1975, 69-79.

[3-11] Laranjeira de Oliveira, F. (2010). Design-oriented constitutive model for steel fiber reinforced concrete. Universitat Politècnica de Catalunya.

[3-12] Li, V. C., & Wang, S. (2003). On high performance fiber reinforced cementitious composites.

[3-13] Kanakubo, T., Miyaguchi, M., & Asano, K. (2016). Influence of Fiber Orientation on Bridging Performance of Polyvinyl Alcohol Fiber-Reinforced Cementitious Composite. ACI Materials Journal, 113(2).

[3-14] Duque, L. F. M., Varga, I., & Graybeal, B. A. (2016, July). Fiber reinforcement influence on the tensile response of UHPFRC. In First International Interactive Symposium on UHPC-2016, Des Moines, IOWA, USA.

[3-15] Kang, S. T., & Kim, J. K. (2012). Investigation on the flexural behavior of UHPCC considering the effect of fiber orientation distribution. Construction and Building Materials, 28(1), 57-65.

[3-16] Gupta, A., & Talha, M. (2015). Recent development in modeling and analysis of functionally graded materials and structures. Progress in Aerospace Sciences, 79, 1-14.

[3-17] Pompe, W., Worch, H., Epple, M., Friess, W., Gelinsky, M., Greil, P., ... & Schulte, K. J. M. S. (2003). Functionally graded materials for biomedical applications. Materials Science and Engineering: A, 362(1-2), 40-60.

[3-18] El-Galy, I. M., Saleh, B. I., & Ahmed, M. H. (2019). Functionally graded materials classifications and development trends from industrial point of view. SN Applied Sciences, 1(11), 1378.

[3-19] Zhou, F., Zhou, R., Du, Y., & Wang, Y. (2022). Flexural behavior of layered CTRC-ECC reinforced cementitious composite plates. Journal of Building Engineering, 62, 105283.

[3-20] Yuan, H., Fu, X. H., Fan, Y. C., Fu, B., & Zou, Q. Q. (2022). Flexural performance of layered macro fiber reinforced concrete beams. Construction and Building Materials, 357, 129314.

[3-21] Rydval, M., Čítek, D., Kolisko, J., Nenadálová, Š., & Bittner, T. (2017). Functionally layered thin slabs made from UHPC and ECC composites. Solid State Phenomena, 259,

90-96.

[3-22] Akshaya, S. L., Prakash, A., & Bharati Raj, J. (2020, May). Applications of functionally graded materials in structural engineering—a review. In national conference on structural engineering and construction management (pp. 553-566). Cham: Springer International Publishing.

[3-23] Liu, Q., Zhang, H., Hong, P., & Han, S. (2020, June). A brief review on the fabrication and mechanical behavior of functionally graded concrete materials. In IOP Conference Series: Earth and Environmental Science (Vol. 525, No. 1, p. 012142). IOP Publishing.

[3-24] Torelli, G., & Lees, J. M. (2020). Interface bond strength of lightweight low-cement functionally layered concrete elements. Construction and Building Materials, 249, 118614.

[3-25] Dias, C. M. R., Savastano Jr, H., & John, V. M. (2010). Exploring the potential of functionally graded materials concept for the development of fiber cement. Construction and Building Materials, 24(2), 140-146.

[3-26] Lai, J., Zhou, J., Yin, X., & Zheng, X. (2021). Dynamic behavior of functional graded cementitious composite under the coupling of high speed penetration and explosion. Composite Structures, 274, 114326.

[3-27] Bao, S., Zhang, Y., Liu, H., Zeng, K., & Zhang, W. (2023). Optimization design of functionally graded ultra‐high performance cementitious composite on flexural behavior. Structural Concrete, 24(2), 2245-2259.

[3-28] Kanakubo, T., Koba, T., & Yamada, K. (2021). Flexural characteristics of functionally graded fiber-reinforced cementitious composite with polyvinyl alcohol fiber. Journal of Composites Science, 5(4), 94.

[3-29] Zhang, H., & Kanakubo, T. (2022, September). Influence of Placing Thickness on Fiber Orientation and Bridging Law of FRCC. In International Conference on Strain-Hardening Cement-Based Composites (pp. 91-97). Cham: Springer International Publishing.

[3-30] Ozu, Y., Miyaguchi, M., & Kanakubo, T. (2018). Modeling of bridging law for PVA fiber-reinforced cementitious composite considering fiber orientation. J. Civ. Eng. Archit, 12, 651-661.

[3-31] JSCE-F 531-2013; Standard Specifications for Concrete Structures — 2013, Test Methods and Specifications. Japan Society of Civil Engineers: Tokyo, Japan, 2013, pp. 281-282. (in Japanese)

[3-32] JIS K 5400; Testing Methods for Paints. Japanese Industrial Standard. Japanese Standards Association (JSA): Tokyo, Japan, 1990. (in Japannese)

[3-33] ISO 21914: 2019; Test Methods for Fibre-Reinforced Cementitious Composites—Bending Moment—Curvature Curve by Four-Point Bending Test. ISO: Geneva, Switzerland, 2019.

[3-34] ISO 1920-4: 2020; Testing of Concrete—Part 4: Strength of Hardened Concrete. ISO: Geneva, Switzerland, 2020.

[3-35] Popovics, S. (1973). A numerical approach to the complete stress-strain curve of concrete. Cement and concrete research, 3(5), 583-599.

Chapter 4 Flexural and crack characteristics of thin plate SHCC with PVA fibers

4.1 Introduction

For SHCCs exhibiting multiple-cracking behavior, crack characteristics—including crack number, crack width, and crack spacing—are the key indicators for evaluating their deformation capacity. Before the initial cracking, the deformation of SHCCs is governed primarily by the elastic deformation of the cementitious matrix. Following cracking of the matrix, the load-transfer mechanism is progressively dominated by the bridging effect of the embedded fibers. Up to the ultimate stage, the tensile stress across the crack is mainly sustained by the fibers bridging the cracks and by the bond stress developed between the fibers and the surrounding matrix, whereas the tensile strain is decided by the combined effects of crack width and crack spacing, which will be detailly illustrated in Chapter 5. Consequently, accurate determination of the tensile stress and the corresponding tensile strain at the ultimate stage is essential for the reliable assessment of the deformation capacity of SHCCs.

Compared to the recommended rectangle cross-section bending specimen by ISO21914 [4-1], thinner specimen is reported to exhibit multi-crack behavior more easily and larger strain capacity at the ultimate stage [4-2]. On the one hand, it is validated by Lu and Leung [4-3] that the thickness of ECC specimen leads to a great influence on the ductility performance since the analytical simulation results showed the ultimate strain capacity of over 100 mm thickness specimen sharply decreased at maximum load stage compared to that of laboratory scale thickness specimen (10-15 mm) while the maximum load had relatively low change. And the degradation of ductility continued as the thickness increased. Rokogo et al. [4-4] drew a conclusion from uniaxial tension tests that thinner specimens can lead to larger ultimate strain capacity and more cracks. Kim et al. [4-5] conducted flexural and tensile tests and made a conclusion that reducing the specimen size can effectively enhance both strength and deflection capacity for steel fiber reinforced concrete. In the uniaxial tension tests on

UHS-ECC conducted by Zhu et al. [4-6], it was observed that a reduction in specimen thickness resulted in an increase in tensile strength, whereas the tensile strain capacity remained essentially unchanged. The previous visualization simulation experiment of different placing thicknesses in Chapter 2 showed that thinner specimen exhibited 2-D tendency than the homogeneous one which will result in lager bridging strength. On the other hand, for specimens exhibiting 2-D orientation, the effective anchorage area of each fiber is more completely developed at both ends with the matrix which limits the development of cracks and the probability that single fiber crosses more cracks can be enhanced [4-7,4-8], thereby increasing the efficiency of stress transfer and improving overall fiber utilization after cracking. Furthermore, thinner specimens lead to shorter crack penetration path, which consequently reduces the fracture energy released by each crack during propagation and making it easier to reach stable multi-crack situation condition [4-9].

As discussed in Chapter 1, although UTTs can directly capture the tensile properties of the material, no unified testing standard for the uniaxial tension characterization of SHCC has yet been established. Moreover, UTTs impose stringent requirements on the testing apparatus, alignment, gripping system, and specimen geometry. In contrast, the specimens used in this study have relatively small thickness, and the maximum mid-span deflection at the ultimate stage reached approximately one-quarter of the specimen length. Under such conditions, the cracks formed on the bottom surface of the pure bending region can be reasonably regarded as tensile-stress-dominated, with negligible shear effects. Pan et al. [4-20] conducted four-point bending tests on thin plate ECC specimens and UTTs using both oil-coated and uncoated PVA fibers with different fiber volume fractions. The tensile strain capacity was subsequently evaluated by inverse analysis methods proposed by Cai and Xu [4-21] and by Qian and Li [4-22]. The results indicated that, for ECC specimens with a fiber volume fraction of 2%, the tensile strain capacity obtained from the inverse analysis based on four-point bending tests was in good agreement with that measured directly from UTTs. This finding demonstrates that the four-point bending test provides an effective experimental approach for estimating the tensile strain capacity of ECC/SHCC specimens. For these reasons, four-point bending tests were adopted in this study to evaluate the cracking characteristics of SHCC.

In order to investigate the crack characteristics of SHCC with PVA fiber of different fiber dimensions, this study applied four point bending test and thin-plate type specimen dimension of 400 mm × 100 mm × 10 mm, which was 1/10 thickness of the conventional bending specimen. The fiber orientation intensity in vertical thickness direction can be regarded as infinity, which was the same as 10 mm visualization simulation specimen in Chapter 2.

4.2 Materials and experiment set-up

4.2.1 Materials and specimen dimension

Three types of PVA short fibers provided by Kuraray Co. Ltd. were adopted in this experiment program and the mechanical properties are listed in Table 4-1. 100 μm-diameter PVA fiber with 2% volume fraction was generally used to investigate the single-crack bridging characteristics [4-10,4-11]. In previous studies [4-12,4-13], a volume fraction of 3% with 100 μm-diameter and 2% with 27/40 μm-diameter PVA fiber specimens showed a typical multi-crack behavior in failure pattern, which was one of the necessary conditions for SHCC, and had a good rheological property and fiber dispersibility. Therefore, the same fiber types and corresponding volume fraction as previous study were utilized in this experiment program. The mix proportion of the SHCC is shown in Table 4-2. For naming, number followed the "PVA" like "027", "040" and "100" represented the diameter, "2%" and "3%" for volume fraction of each series. 10 specimens were prepared for the bending test and 3 specimens used Φ100mm-200mm cylinder for the compressive test of each series.

Table 4-1 Mechanical properties of PVA fiber

Type	**Diameter (μm)**	**Length (mm)**	**Tensile strength (MPa)**	**Elastic modulus (GPa)**	**Volume fraction**
PVA027	27	6	1800	45	2%
PVA040	40	12	1560	41	2%
PVA100	100	12	1200	28	3%

Table 4-2 Mix proportion of FRCC ($V_f = 2\%$)

W/B ratio	Sand by binder ratio	Unit weight (kg/m^3)				
		Water	Cement	Fly ash	Sand	PVA fiber
0.39	0.50	380	678	291	484	26

Table 4-3 Compression test results

Specimen type	Avg. compression strength (MPa)	Young's modulus (GPa)
PVA027-2%	45.5	15.0
PVA040-2%	32.3	12.6
PVA100-3%	53.4	21.1

4.2.2 Four-point bending experiment set-up

A four-point bending test generally followed by ISO 21914 [4-1] was conducted. Before loading, three red lines were drawn on 100 mm × 100 mm pure bending area of bottom surface at 15 mm, 50 mm, and 75 mm distance respectively from the side where the displacement transducers are set as the schematic figure shown in Figure 4-1. In addition, the red line of 75 mm from the edge of π-type displacement transducer side would gradually disappear in digital camera vision field during loading because of the vertical displacement of specimen, the remaining two red lines were used to identify the crack width and crack spacing where they intersect. Figure 4-2 shows the experiment set-up. A precision of 1 N load cell was applied in loading. The digital camera was set in front of the loading stand to take photos for an interval of every 5 seconds and kept the shooting angle unchanged during the experiment. To allow the digital camera to capture the crack developments in the target area on the bottom side of the specimen, a mirror was set directly beneath the specimen. Three linear variable displacement transducers (LVDTs) are set at mid-span and the supports to measure the deflections. The mid-span deflection is calculated by subtracting the average displacement measured by the LVDTs at the supports from the displacement measured at the mid-span. The system time of the test recorder and digital camera was calibrated to be consistent before loading. Due to the detachment of the nuts securing the π-type displacement transducers during loading in two of the PVA100-3% specimens, only eight valid specimens were obtained for this series.

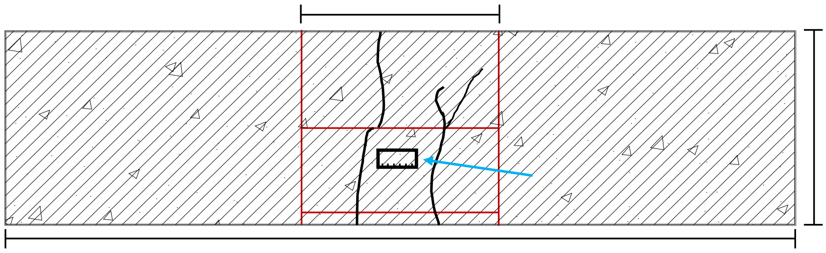

Figure 4-1 Specimen preparation

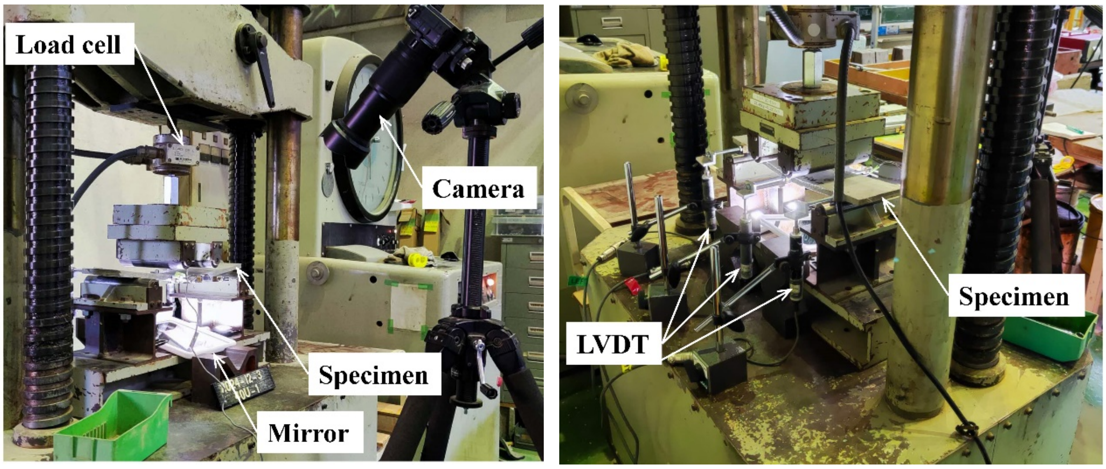

(a) Front view (b) Back view

Figure 4-2 Four-point bending test set-up

4.3 Experiment results

4.3.1 Typical crack pattern

The photos of mid-span deflection of 5 mm and 10 mm, maximum load stage and the ultimate stage were selected. The definition of the ultimate stage will be explained in section 4.3.2. By matching the time recorded by the recorder and digital camera respectively, specimen photos of crack development corresponding to each stage were selected.

Figure 4-3 shows the typical crack patterns of each series at 5 mm mid-span deflection. At this stage, multiple cracks could be clearly observed on the tensile surfaces of specimens from all three series; however, no pronounced differences in crack width or crack spacing were evident by visual inspection among the different series.

Figure 4-4 shows the typical crack patterns of each series at 10 mm mid-span deflection. At this stage, in comparison with the crack morphology at mid-span deflection of 5 mm, the existing cracks continued to propagate, with the widths further increased, while new cracks were continuously generated at the same time. Relative to the PVA100-3% series, the PVA027-2% and PVA040-2% series exhibited a greater number of cracks accompanied by smaller crack spacing.

Figure 4-5 shows the typical crack patterns of each series at the maximum load stage. At this stage, compared with the crack morphologies observed in the preceding two stages, both the number of cracks and the crack widths increased further. The PVA027-2% and PVA040-2% series specimens developed significantly more cracks than the PVA100-3% series, whereas their corresponding crack spacing was markedly smaller.

Figure 4-6 shows the typical crack patterns of each series at the ultimate stage. It could be observed that numbers of cracks developed on the surface of each series specimens, most of which width are less than 0.5 mm recognized by eyes and crack scale placed on the specimen, which confirms all these three types of PVA-FRCC thin plate specimens show a multiple-crack characteristic. For PVA027-2% and PVA040-2% specimens, the numbers of cracks that could be observed are significantly larger than that of PVA100-3% specimens, and most of the crack widths and crack spacings were smaller than those of the PVA100-3% specimens. For all specimens, as one of the cracks continued to open and the mid-span deflection increased, the specimens eventually reached the failure state and there would not be any new crack generated in this stage.

Specimen No.	Crack pattern
PVA027-2%-7	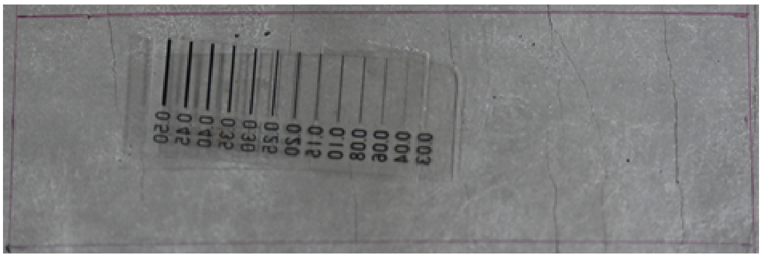
PVA040-2%-4	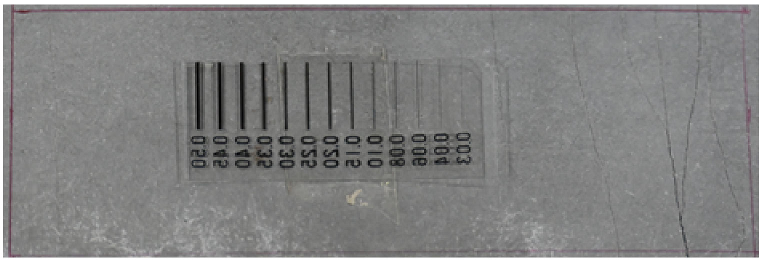
PVA100-3%-3	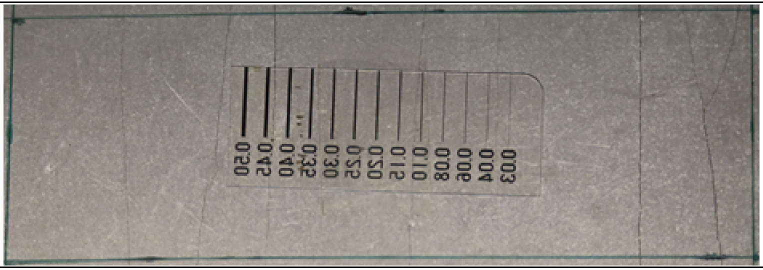

Figure 4-3 The typical crack patterns at deflection = 5 mm.

Specimen No.	Crack pattern
PVA027-2%-7	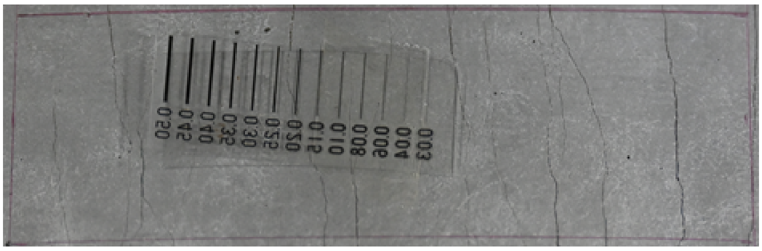
PVA040-2%-4	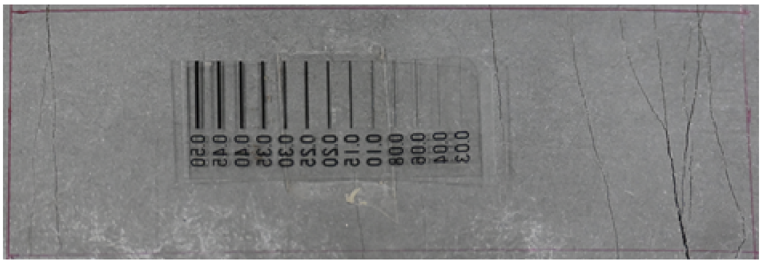
PVA100-3%-3	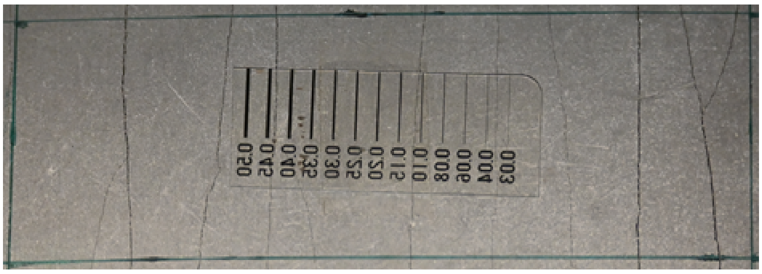

Figure 4-4 The typical crack patterns at deflection = 10 mm.

Specimen No.	Crack pattern
PVA027-2%-7	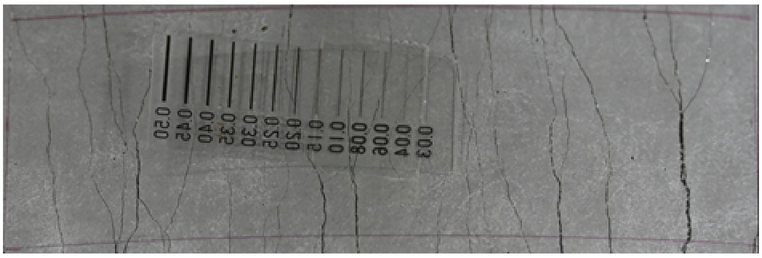
PVA040-2%-4	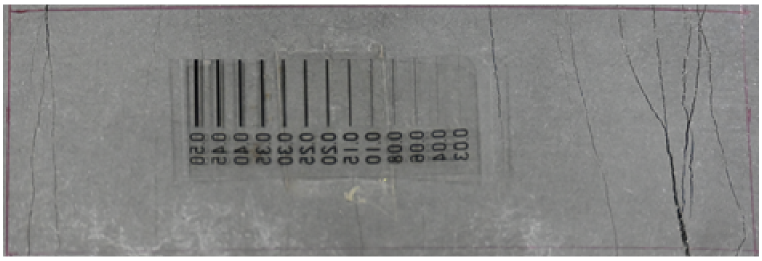
PVA100-3%-3	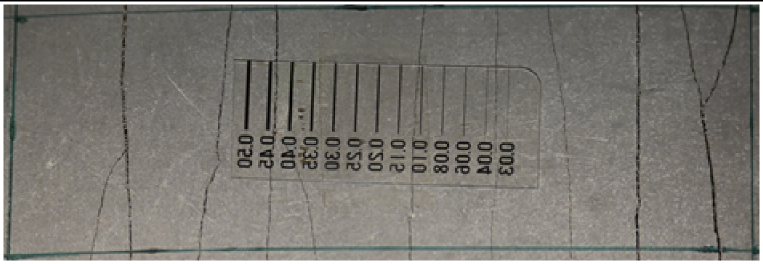

Figure 4-5 The typical crack patterns at the max. load stage

Specimen No.	Crack pattern
PVA027-2%-7	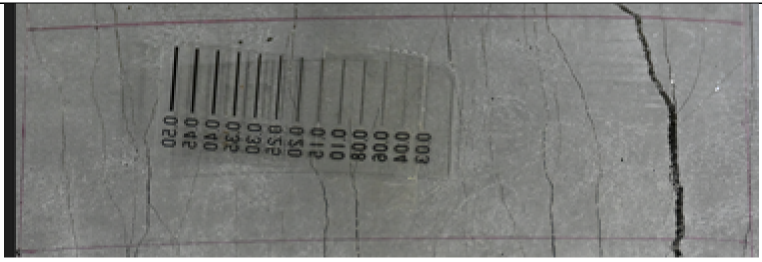
PVA040-2%-4	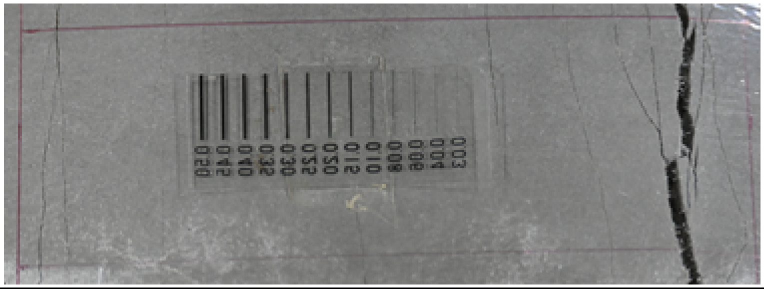
PVA100-3%-3	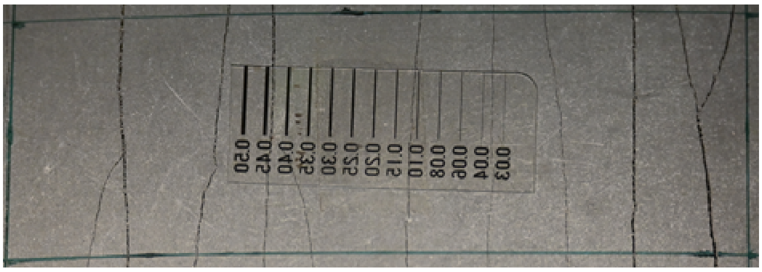

Figure 4-6 The typical crack patterns at the ultimate stage.

4.3.2 Load-mid-span deflection relationship

Figure 4-7 shows the load-mid-span deflection responses of the three series of specimens. During loading, it was observed that the first crack—which may not be identifiable by visual inspection—had already initiated at a certain location while the specimen was still located in the nominally elastic ascending phase of the curve. The opening of the initial crack formed once because the strain capacity of single crack exceeded the maximum tensile strain of the weakest section in matrix, which the fiber content of SHCC had limited influence on this stage [4-14]. Prior to crack initiation, SHCC specimens exhibited linear-elastic behavior with no permanent deformation.

For all specimen series, following the appearance of the first load reduction associated with crack initiation, then the load gradually increased again with continued growth of mid-span deflection. This response demonstrates a typical deflection-hardening behavior and indicates the potential development of strain-hardening characteristics. During this stage, fiber bridging governed the load-transfer mechanism across the crack, enabling the development of the existing cracks and opening of additional cracks at the same time while sustaining load capacity. The formation of successive cracks and the associated enhancement in load were attributed to the sufficient tensile strength of fibers and bond strength between the fibers and the matrix, which allowed stable fiber pull-out resistance.

After reaching the maximum load, the PVA027-2% and PVA040-2% specimens exhibited a creeper reduction in load as deflection continued to increase, whereas the PVA100-3% specimens showed a comparatively slower post-peak load decrease prior to final failure. As described in previous section 4.3.1 crack pattern analysis, in most situations, the post-peak softening phase after reaching the maximum load until failure corresponds to the progressive widening of a dominant crack without the new opening of additional cracks. In certain cases, new cracks could be still observed to develop during the descending phase after reaching the maximum load. Consequently, defining the ultimate stage solely based on the attainment of maximum load and the corresponding deflection may lead to an underestimation of the deformation capacity of SHCC thin-plate specimens.

Reference [4-15] defines the ultimate stress as 80% of the peak tensile stress obtained from the uniaxial tension tests, and the corresponding strain is taken as the ultimate strain. Although reference [4-19] mentioned a concept of *final strain stage* and reference [] defined as *destructive strain*, few detailed definitions or explicit explanations of this stage was provided. Apart from these, few studies or existing standards provide a detailed and explicit definition of the ultimate stage for SHCC. Therefore, in this study, the ultimate stage is defined not by the maximum crack mouth opening of the main crack or solely by the attainment of maximum load, but rather by the cessation of new crack formation on the tensile surface. Specifically, within the load–mid-span deflection curve, the ultimate stage is identified as the interval between 1) the point immediately preceding the first instance where the load decreases to below 0.9 times of the maximum load, and 2) the final point at which the load begins to monotonically decline.

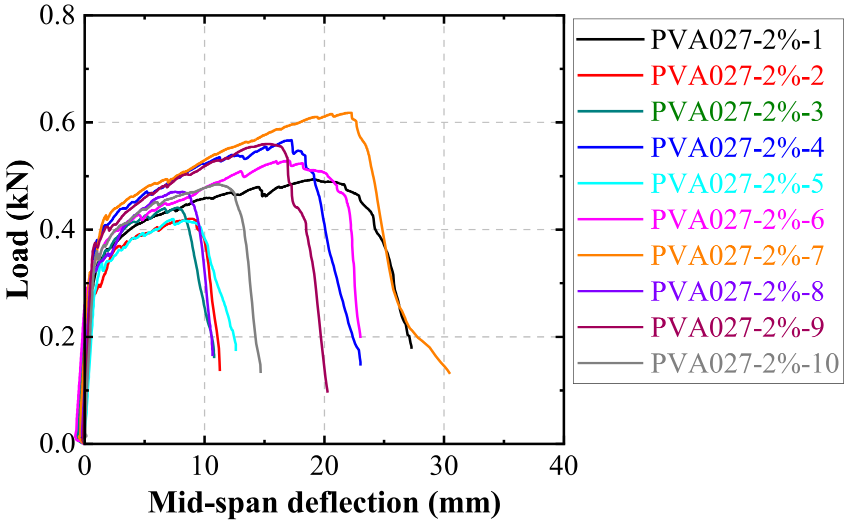

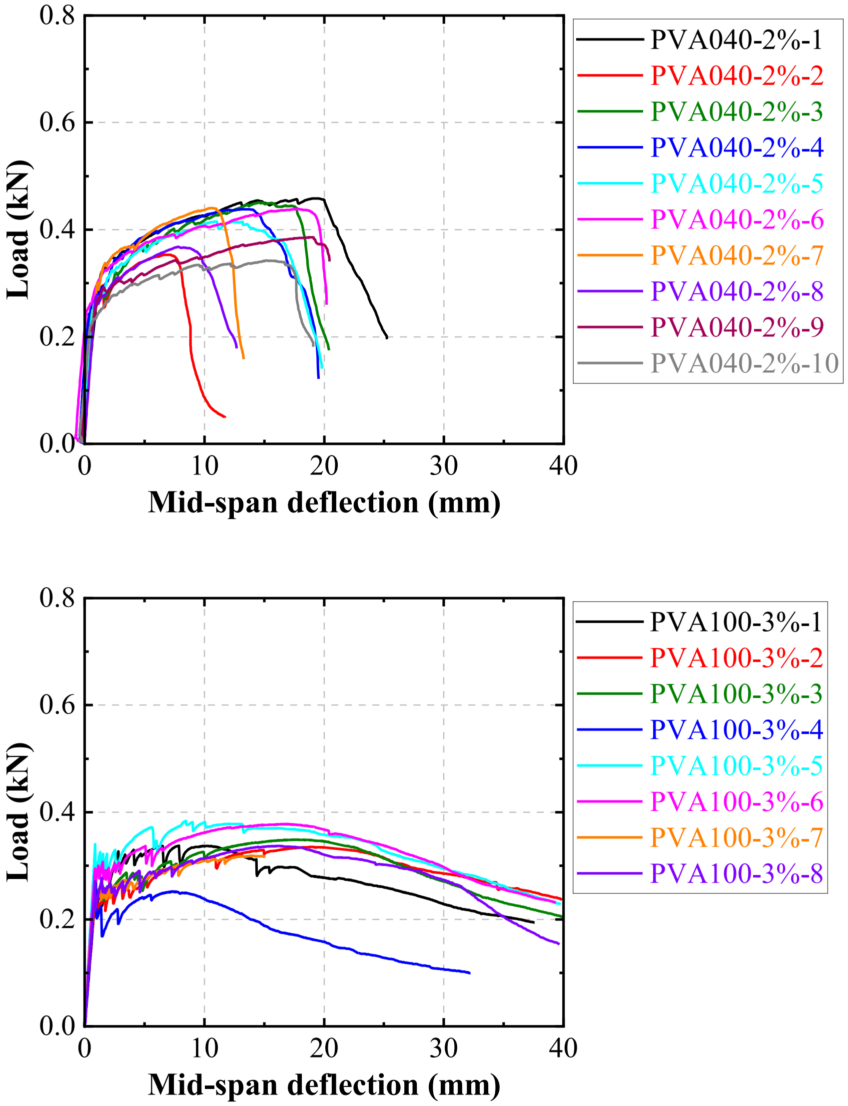

Figure 4-7 Load-mid-span deflection relationship

4.4 Crack characteristics of thin plate SHCC by image analysis

4.4.1 Image processing procedure

An image processing measurement was adopted to identify and obtain statistical data of crack widths and crack spacings. Lu et al. [4-16] developed an image processing method based on a dual-threshold algorithm, which more accurately and conveniently determines the crack width obtained from UTTs. Due to different experiment conditions and non-open-access of the fore-mentioned improved image processing method, the following image processing method was adopted in this study. An open-source image processing software commonly used in the biological research field named *ImageJ* [4-17], is adopted to process the selected photos of each stage based on the definition and classification in section 4.3.2. The image processing steps are as follows: First, the selected photos of each stage were converted from RGB format to grayscale. Then, the threshold of black and white was adjusted to a suitable value to show all the crack characteristics and binarize the grayscale image into only contained black and white pixels. Next, set the target length of the red line drawn in the experiment preparation to a scale of 100 mm. Finally, use the "Measure" function of the software to measure the pixels crossing crack widths and the crack spacings of selected photos within the former setting scale.

4.4.2 Statistics and distribution

The objective of this study is to investigate the crack characteristics—including the number of cracks, crack width, and crack spacing—of each series of PVA-FRCC specimens at each target stage of loading. The statistical results are summarized in Table 4-4 and Table 4-5. The crack widths for each specimen series at both the maximum-load stage and ultimate stage were categorized into bins of 0.04 mm, and histograms were illustrated as shown in Figure 4-8. Similarly, the crack spacing data were categorized into bins of 2 mm, with the corresponding histograms illustrated in Figure 4-9. The probability density of each specimen series was calculated according to Eq. (4-1), which adopted a *bin* width of 0.04 mm for crack width recommended by [4-18].

$$P_i = \frac{f_i}{N \times Bin} \qquad \text{Eq. (4-1)}$$

P_i: Probability density of $Bin\ i$

f_i: Frequency of $Bin\ i$

Bin: 0.04 mm

N: Total sample size

Both normal and log-normal probability density distributions were fitted to the experiment data. The fitting results indicate that the lognormal distribution provided a superior representation of the experimental data for both crack width and crack spacing across all stages, consistent with the right-skewed characteristics of distribution. The results of Kolmogorov-Smirnov test shown in Table 4-6 and Table 4-7 also support this conclusion, since the significance value D constructed for lognormal distribution showed a smaller result than the p-value at all stages.

For the PVA027-2% specimens, most crack widths were below 0.50 mm at all stages. At the stage of deflection of 5 mm, the majority of crack widths were concentrated between 0.04 mm and 0.20 mm, with a small proportion of those ranging from 0.20 mm to 0.60 mm, meanwhile the median values located in the left-hand side of the mean value, exhibiting a clear right-skewed-tail characteristic of typical log-normal distributions. With increasing deflection, existing cracks gradually widened while new cracks continued to open at the same time, resulting in an increase in average crack width. The crack width distribution of the PVA040-2% specimens was similar to that of the PVA027-2% specimens, whereas that of the PVA100-3% specimens exhibited a similar shape but differed in the concentration range and average crack width at each stage.

In contrast, the distribution pattern of crack spacing was opposite to that of crack width. At the early stage (deflection = 5 mm), the crack spacing values were widely distributed. As deflection increased, the crack spacing of all specimen series became progressively more concentrated within a narrower range. At each stage, the median values were generally located in the left-hand side of the mean value, and the crack spacing distribution also exhibited a right-skewed-tail characteristic consistent with a lognormal distribution. These findings confirm that with increasing deflection, the formation of additional cracks and the widening of existing ones within the same gauge length led to a reduction in average crack spacing.

The statistical average values of crack number, crack width, and crack spacing for each specimen series at the maximum load and ultimate stages are illustrated in the

Figure 4-10.

During the maximum load stage, the average number of cracks for the PVA027-2% and PVA040-2% series specimens remained nearly constant at approximately 30, which was approximately twice that of the PVA100-3% specimens. Regarding the average crack width, the PVA027-2% and PVA040-2% specimens—both containing finer-diameter fibers—showed similar values, but these were significantly smaller than those of the PVA100-3% specimens containing coarser fibers and a higher fiber volume fraction, indicating a tendency that the crack widths increase as the increase of fiber diameters. The standard deviation of crack width across all three series ranged around 41%-60% of the mean, indicating a relatively higher degree of statistical dispersion.

In terms of crack spacing, the PVA027-2% and PVA040-2% specimens again showed similar behavior, with average values considerably smaller than those of the PVA100-3% series. The variability in crack spacing was more pronounced: the standard deviations for the PVA027-2% and PVA040-2% specimens were nearly equal to their respective means (76% and 91%), whereas that of the PVA100-3% specimens was approximately half the mean (48%). This suggests a higher degree of spatial irregularity in crack distribution for specimens with finer diameter of fibers.

The qualitative tendencies observed at the ultimate stage were generally consistent with those at the maximum load stage. Compared with the maximum load stage, the average number of cracks at the ultimate stage increased by approximately 3% for the PVA027-2% and PVA040-2% specimens, while the PVA100-3% specimens exhibited an increase of approximately 8%, indicating that new cracks continued to open beyond the maximum load stage. This finding suggests that defining the maximum load point and the corresponding deflection as the end of the strain-hardening stage or deflection-hardening stage may underestimate the real cracking capacity of this material. Furthermore, compared with the maximum load stage, the average crack widths and standard deviations of the PVA027-2% and PVA040-2% specimens remained nearly unchanged at ultimate stage, whereas those of the PVA100-3% specimens increased more slightly. The average crack spacings slightly decreased for

PVA027-2% and PVA040-2% series from the maximum load stage to the ultimate stage, consistent with the fore-mentioned conclusion of average crack widths that the additional formation of new cracks and widening of existing crack widths within the same gauge length would lead to narrower crack spacings. For the PVA100-3% series, several specimens reached the maximum load stage at relatively small mid-span deflections, after which additional cracks continued to develop. As the number of cracks increased and the crack spacing decreased during this process, the crack spacing at the ultimate stage became larger than that measured at the maximum load stage.

Overall, these results confirm that as fiber diameter increases, the number of fibers per unit volume under the same volume fraction decreases, which leads to a reducing of the total bridging capacity provided by the fibers. Consequently, specimens incorporating finer diameter of PVA fibers (27 μm and 40 μm) exhibited a larger number and finer in width of cracks after reaching the cracking stress of matrix, while those with coarser fibers in diameter (100 μm) developed fewer numbers but wider in width of cracks. This confirms that finer-diameter fibers are more effective in promoting multiple cracking and enhancing the strain-hardening behavior of PVA-FRCC.

Table 4-4 Statistic of crack width

PVA027-2%

Subject	Stage			
	5mm	**10mm**	**Max.**	**Ult.**
Avg. crack width (mm)	0.16	0.19	0.20	0.19
Avg. crack number	14.0	25.9	29.6	30.5
Standard deviation of crack width (mm)	0.10	0.10	0.12	0.12
COV	0.63	0.53	0.60	0.63
Max. crack width (mm)	0.57	0.95	1.24	1.24
Min. crack width (mm)	0.03	0.03	0.06	0.03
Median (mm)	0.14	0.17	0.19	0.18

PVA040-2%

Subject	Stage			
	5mm	**10mm**	**Max.**	**Ult.**
Avg. crack width (mm)	0.15	0.18	0.19	0.19
Avg. crack number	14.2	24.3	30.1	31.1
Standard deviation of crack width (mm)	0.07	0.11	0.11	0.12
COV	0.47	0.61	0.58	0.63
Max. crack width (mm)	0.42	0.79	0.77	0.79
Min. crack width (mm)	0.05	0.05	0.03	0.03
Median (mm)	0.14	0.14	0.17	0.16

PVA100-3%

Subject	Stage			
	5mm	**10mm**	**Max.**	**Ult.**
Avg. crack width (mm)	0.23	0.29	0.27	0.37
Avg. crack number	11.3	15.4	15.5	16.8
Standard deviation of crack width (mm)	0.08	0.12	0.11	0.18
COV	0.35	0.41	0.41	0.49
Max. crack width (mm)	0.54	0.97	0.65	1.34
Min. crack width (mm)	0.06	0.09	0.06	0.06
Median (mm)	0.18	0.21	0.26	0.29

Table 4-5 Statistic of crack spacing

PVA027-2%

Subject	**Stage**			
	5mm	**10mm**	**Max.**	**Ult.**
Avg. crack spacing (mm)	12.36	7.24	6.61	6.28
Avg. crack spacing number	13.0	24.9	28.6	29.5
Standard deviation of crack spacing (mm)	10.46	5.24	5.00	4.61
COV	0.85	0.72	0.76	0.73
Max. crack spacing (mm)	35.79	29.1	35.73	32.22
Min. crack spacing (mm)	0.17	0.20	0.10	0.10
Median (mm)	9.29	6.64	5.10	5.05

PVA040-2%

Subject	**Stage**			
	5mm	**10mm**	**Max.**	**Ult.**
Avg. crack spacing (mm)	13.24	8.28	7.25	7.07
Avg. crack spacing number	13.2	23.3	29.1	30.1
Standard deviation of crack spacing (mm)	12.20	7.45	6.61	6.42
COV	0.92	0.90	0.91	0.91
Max. crack spacing (mm)	60.38	44.79	41.17	41.17
Min. crack spacing (mm)	0.37	0.17	0.06	0.06
Median (mm)	8.75	5.77	4.67	4.56

PVA100-3%

Subject	**Stage**			
	5mm	**10mm**	**Max.**	**Ult.**
Avg. crack spacing (mm)	15.90	11.96	9.57	11.13
Avg. crack spacing number	10.3	14.4	14.5	15.8
Standard deviation of crack spacing (mm)	11.09	6.15	4.61	5.98
COV	0.70	0.51	0.48	0.54
Max. crack spacing (mm)	55.72	25.97	29.73	24.67
Min. crack spacing (mm)	0.15	0.15	0.12	0.15
Median (mm)	12.13	10.60	10.22	9.82

Table 4-6 K-S test result of crack width

PVA027-2%

Subject		**Stage**			
		***D* = 5mm**	***D* = 10mm**	**Max. load**	**Ult.**
Normal distribution	p-value	5.1×10-5	4.1×10-5	3.56×10-5	8.80×10-6
	D	0.19	0.17	0.14	0.14
Lognormal distribution	p-value	0.25	0.08	0.31	0.20
	D	0.08	0.16	0.06	0.06

PVA040-2%

Subject		**Stage**			
		***D* = 5mm**	***D* = 10mm**	**Max. load**	**Ult.**
Normal distribution	p-value	3.3×10-4	2.2×10-5	6.1×10-5	5.5×10-5
	D	0.17	0.16	0.13	0.13
Lognormal distribution	p-value	0.18	0.06	0.35	0.15
	D	0.09	0.09	0.05	0.06

PVA100-3%

Subject		**Stage**			
		***D* = 5mm**	***D* = 10mm**	**Max. load**	**Ult.**
Normal distribution	p-value	2.4×10-3	2.3×10-4	0.22	2.0×10-3
	D	0.19	0.19	0.09	0.16
Lognormal distribution	p-value	0.11	0.59	0.06	0.41
	D	0.12	0.07	0.73	0.08

Table 4-7 K-S test result of crack spacing

PVA027-2%

Subject		**Stage**			
		***D* = 5mm**	***D* = 10mm**	**Max. load**	**Ult.**
Normal distribution	p-value	0.07	0.07	9.5×10-4	3.9×10-3
	D	0.12	0.10	0.12	0.10
Lognormal distribution	p-value	0.88	0.51	0.13	0.17
	D	0.05	0.06	0.07	0.07

PVA040-2%

Subject		**Stage**			
		***D* = 5mm**	***D* = 10mm**	**Max. load**	**Ult.**
Normal distribution	p-value	1.2×10-5	4.4×10-5	5.5×10-6	2.4×10-6
	D	0.22	0.17	0.15	0.15
Lognormal distribution	p-value	0.07	0.45	0.56	0.50
	D	0.60	0.06	0.05	0.05

PVA100-3%

Subject		**Stage**			
		***D* = 5mm**	***D* = 10mm**	**Max. load**	**Ult.**
Normal distribution	p-value	0.13	0.21	0.26	0.32
	D	0.13	0.10	0.09	0.09
Lognormal distribution	p-value	0.88	0.90	0.98	0.97
	D	0.07	0.05	0.04	0.04

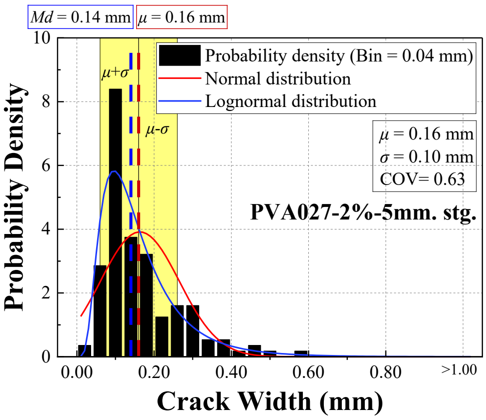
Md = 0.14 mm
μ = 0.16 mm
Probability density (Bin = 0.04 mm)
Normal distribution
Lognormal distribution
μ+σ
μ-σ
μ = 0.16 mm
σ = 0.10 mm
COV= 0.63
PVA027-2%-5mm. stg.
Probability Density
Crack Width (mm)
0
2
4
6
8
10
0.00
0.20
0.40
0.60
0.80
>1.00

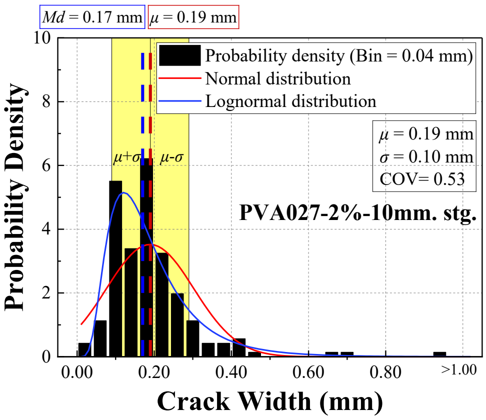
Md = 0.17 mm
μ = 0.19 mm
Probability density (Bin = 0.04 mm)
Normal distribution
Lognormal distribution
μ+σ
μ-σ
μ = 0.19 mm
σ = 0.10 mm
COV= 0.53
PVA027-2%-10mm. stg.
Probability Density
Crack Width (mm)
0
2
4
6
8
10
0.00
0.20
0.40
0.60
0.80
>1.00

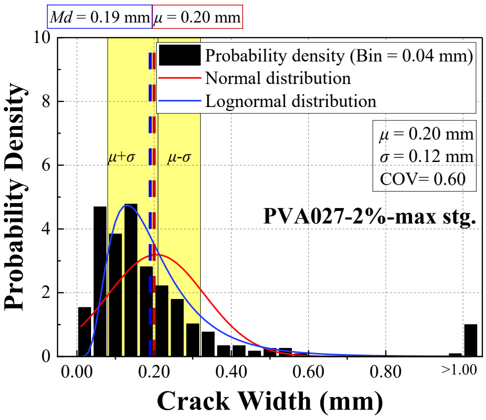
Md = 0.19 mm
μ = 0.20 mm
Probability density (Bin = 0.04 mm)
Normal distribution
Lognormal distribution
μ+σ
μ-σ
μ = 0.20 mm
σ = 0.12 mm
COV= 0.60
PVA027-2%-max stg.
Probability Density
Crack Width (mm)
0
2
4
6
8
10
0.00
0.20
0.40
0.60
0.80
>1.00

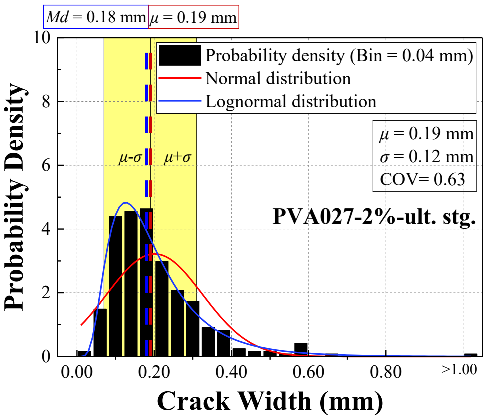
Md = 0.18 mm
μ = 0.19 mm
Probability density (Bin = 0.04 mm)
Normal distribution
Lognormal distribution
μ-σ
μ+σ
μ = 0.19 mm
σ = 0.12 mm
COV= 0.63
PVA027-2%-ult. stg.
Probability Density
Crack Width (mm)
0
2
4
6
8
10
0.00
0.20
0.40
0.60
0.80
>1.00

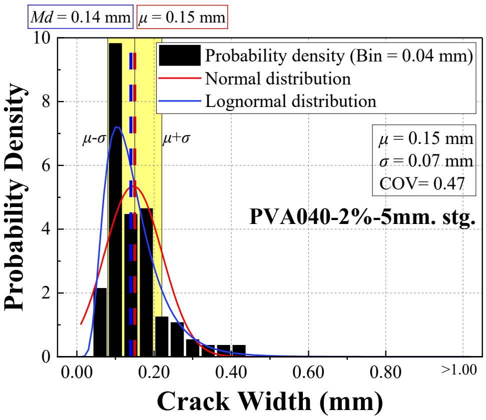
Md = 0.14 mm
μ = 0.15 mm
Probability density (Bin = 0.04 mm)
Normal distribution
Lognormal distribution
μ-σ
μ+σ
μ = 0.15 mm
σ = 0.07 mm
COV= 0.47
PVA040-2%-5mm. stg.
Probability Density
Crack Width (mm)
0
2
4
6
8
10
0.00
0.20
0.40
0.60
0.80
>1.00

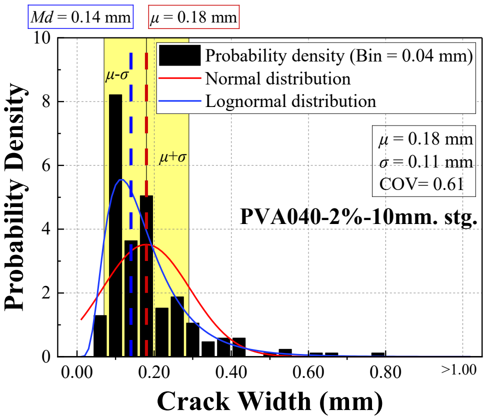
Md = 0.14 mm
μ = 0.18 mm
Probability density (Bin = 0.04 mm)
Normal distribution
Lognormal distribution
μ-σ
μ+σ
μ = 0.18 mm
σ = 0.11 mm
COV= 0.61
PVA040-2%-10mm. stg.
Probability Density
Crack Width (mm)
0
2
4
6
8
10
0.00
0.20
0.40
0.60
0.80
>1.00

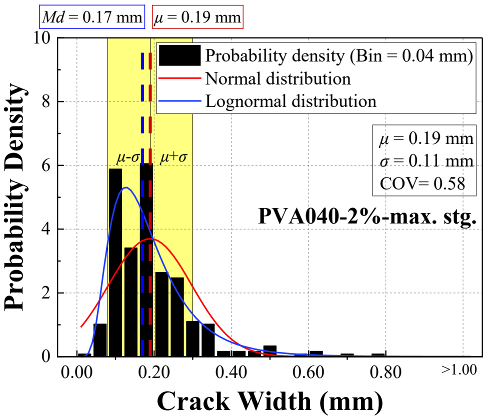
Md = 0.17 mm
μ = 0.19 mm
Probability density (Bin = 0.04 mm)
Normal distribution
Lognormal distribution
μ-σ
μ+σ
μ = 0.19 mm
σ = 0.11 mm
COV= 0.58
PVA040-2%-max. stg.
Probability Density
Crack Width (mm)
0
2
4
6
8
10
0.00
0.20
0.40
0.60
0.80
>1.00

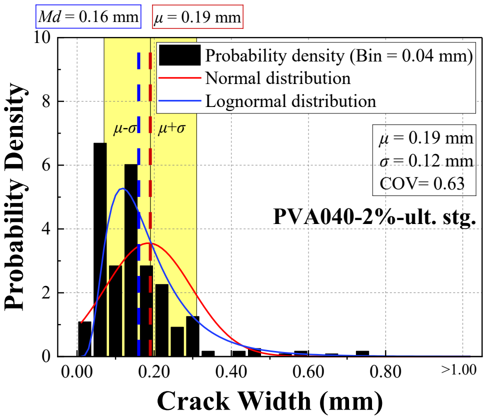
Md = 0.16 mm
μ = 0.19 mm
Probability density (Bin = 0.04 mm)
Normal distribution
Lognormal distribution
μ-σ
μ+σ
μ = 0.19 mm
σ = 0.12 mm
COV= 0.63
PVA040-2%-ult. stg.
Probability Density
Crack Width (mm)
0
2
4
6
8
10
0.00
0.20
0.40
0.60
0.80
>1.00

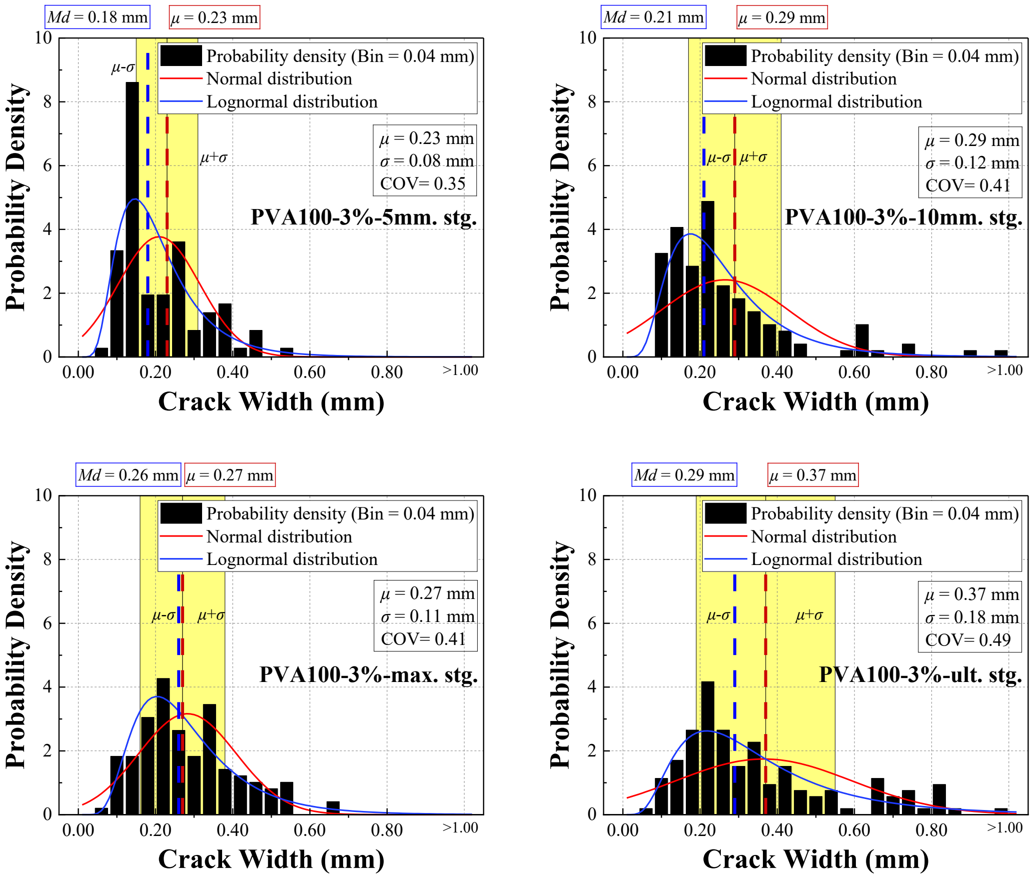

Figure 4-8 Distribution of crack widths (Bin = 0.04 mm)

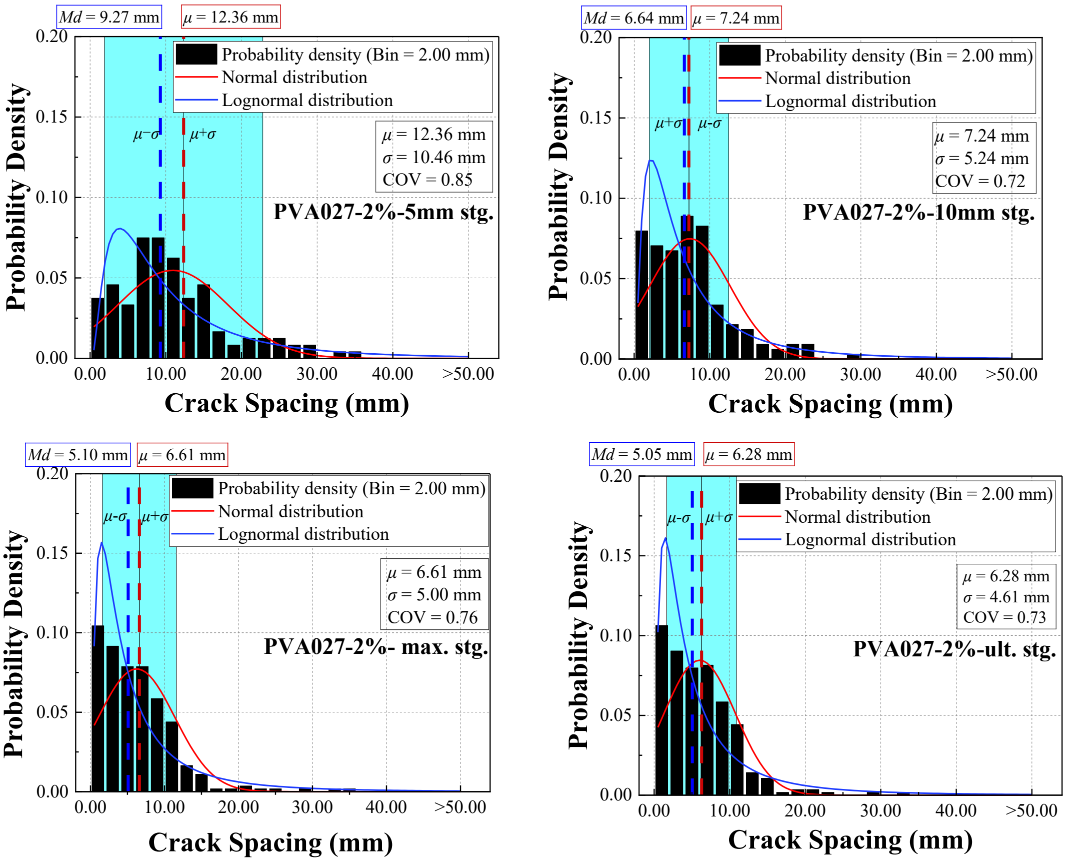

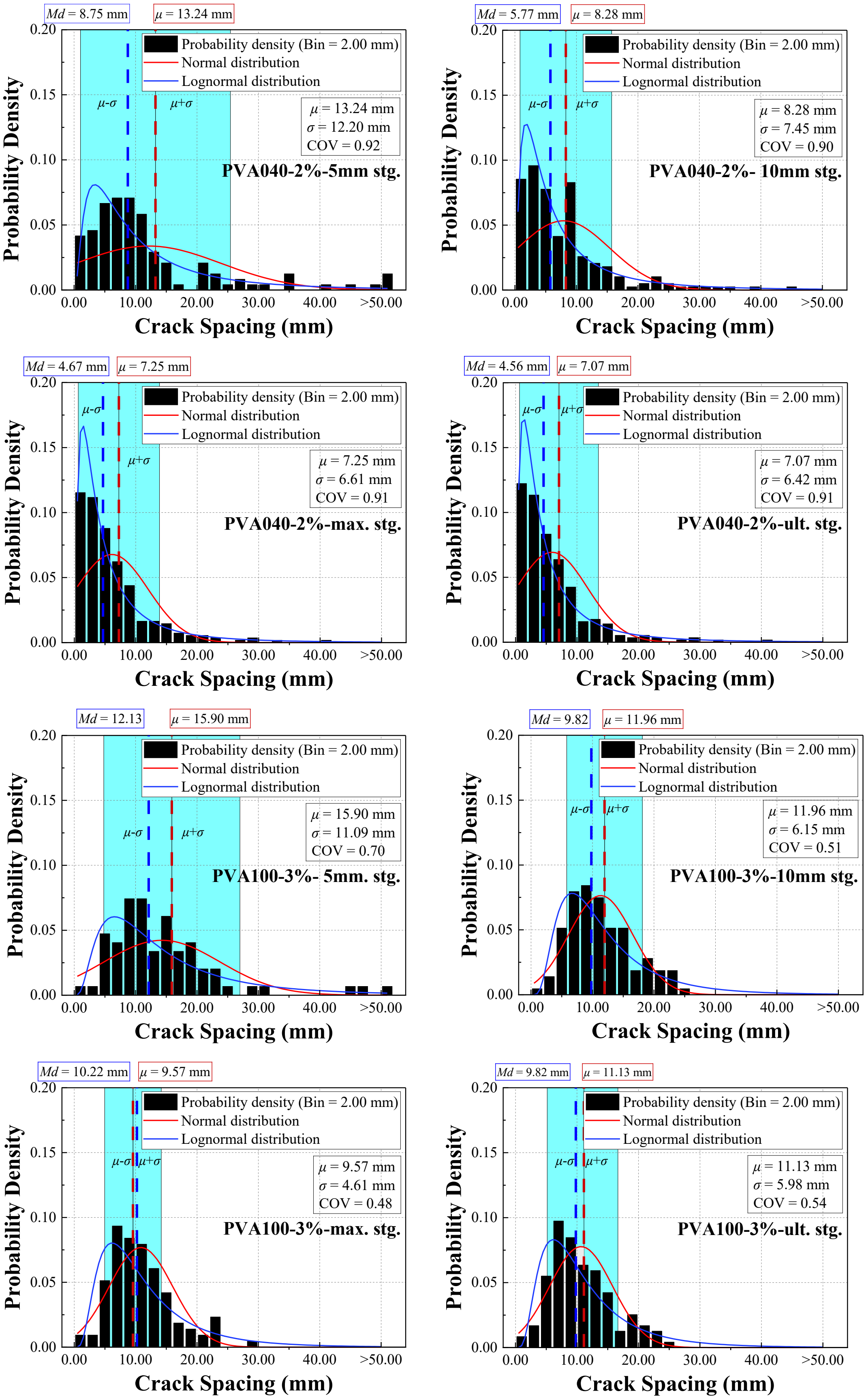

Figure 4-9 Distribution of crack spacings (Bin = 2.0 mm)

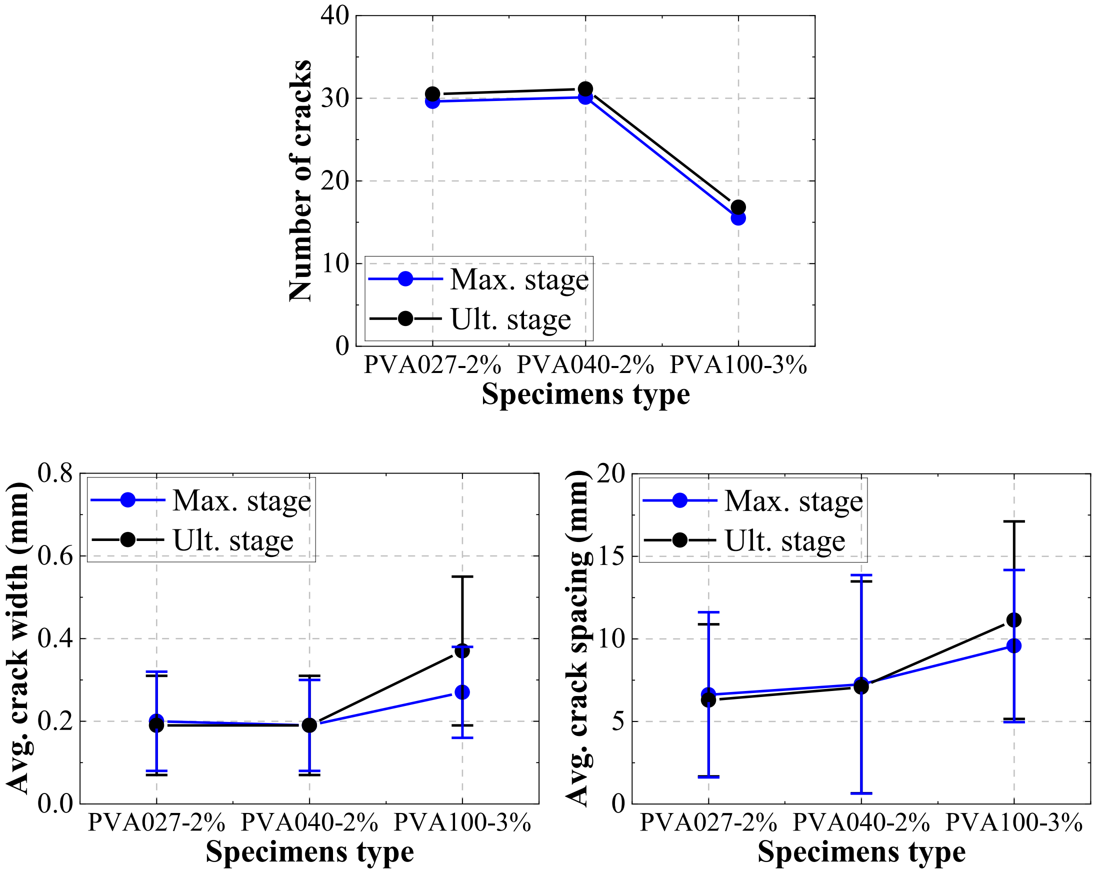

Figure 4-10 Average value of crack characteristics at max. stage and ult. stage

4.5 Summary

This study conducted four-point bending tests to investigate the crack characteristics of SHCC thin plate specimens using different dimensions of PVA fibers. Statistical fittings were employed to quantitively analyze the mathematical distributions of crack widths and crack spacings after the image processing. The results showed that:

(1) The failure pattern confirmed that all three series of SHCC specimens using different dimensions of PVA fibers demonstrated typical multi-crack characteristics. At the ultimate stage, preliminary comparisons using crack-scale measurements indicated that the majority of cracks had widths less than 0.50 mm. Furthermore, the PVA100-3% specimens displayed considerably larger crack spacings than the PVA027-2% and PVA040-2% series, highlighting the influence of fiber diameter and volume fraction on crack distribution.

(2) For the load-mid-span deflection relationship of all three series specimens, after

the appearance of the first deduction, the stiffnesses led to a decreasing firstly, then the load increased again with continuous increase of mid-span deflection, showing the typical deflection-hardening behaviors and potential strain-hardening characteristics. Compared to the PVA027-2% and PVA040-2% series specimens, which showed a creeper decrease after reaching the maximum load, the PVA100-3% specimens demonstrated a relatively deduction until failure.

(3) The lognormal distribution showed better fitting results with the statistical data of crack widths and crack spacings than normal distribution. The average crack widths and average crack spacings showed increasing tendency as the increase of the fiber diameter.

Reference

[4-1] International Standard. Test Methods for Fibre-Reinforced Cementitious Composites—Bending Moment—Curvature Curve by Four-Point Bending Test. ISO 21914:2019.

[4-2] Bastien-Masse, M., Denarié, E., & Brühwiler, E. (2016). Effect of fiber orientation on the in-plane tensile response of UHPFRC reinforcement layers. Cement and Concrete Composites, 67, 111-125.

[4-3] Lu, C., & Leung, C. K. (2017). Theoretical evaluation of fiber orientation and its effects on mechanical properties in Engineered Cementitious Composites (ECC) with various thicknesses. Cement and Concrete Research, 95, 240-246.

[4-4] Rokugo, K., Uchida, Y., Moriyama, M., & Lim, S. (2007). Direct tensile behavior and size effect of strain-hardening fiber-reinforced cement-based composites (SHCC). In Proceedings of the 6th International Conference on Fracture Mechanics of Concrete and Concrete Structures, Catania, Italy, Jun (pp. 17-22).

[4-5] Kim, D. J., Naaman, A. E., & El-Tawil, S. (2010, May). Correlation between tensile and bending behavior of FRC composites with scale effect. In Proceedings of FraMCoS-7, 7th international conference on fracture mechanics of concrete and concrete structures. Jeju Island, South Korea (p. 162).

[4-6] Zhu, J. X., Huang, B. T., Liu, W. H., Xu, L. Y., Peng, K. D., & Dai, J. G. (2025). Size effect and mechanism-based multiphase modeling of strain-hardening behavior of Ultra-High-Strength Engineered Cementitious Composites (UHS-ECC). Cement and Concrete Composites, 106424.

[4-7] Tao, Z., Qiu, M., Wille, K., Zhu, Y., Pan, R., Li, Z., & Shao, X. (2025). Effects of specimen thickness and fiber length on tensile and cracking behavior of UHPFRC: Uniaxial tensile test and micromechanical modeling. Cement and Concrete Composites, 155, 105828.

[4-8] Kang, S. T., & Kim, J. K. (2011). The relation between fiber orientation and tensile behavior in an Ultra High Performance Fiber Reinforced Cementitious Composites (UHPFRCC). Cement and Concrete Research, 41(10), 1001-1014.

[4-9] Li, V. C., & Leung, C. K. (1992). Steady-state and multiple cracking of short random fiber composites. Journal of engineering mechanics, 118(11), 2246-2264.

[4-10] Ozu, Y., Miyaguchi, M., & Kanakubo, T. (2018). Modeling of bridging law for PVA fiber-reinforced cementitious composite considering fiber orientation. J. Civ. Eng. Archit, 12, 651-661.

[4-11] Kanakubo, T., Miyaguchi, M., & Asano, K. (2016). Influence of Fiber Orientation on

Bridging Performance of Polyvinyl Alcohol Fiber-Reinforced Cementitious Composite. ACI Materials Journal, 113(2).

[4-12] Tian, W., Zhang, H., Kanakubo, T. (2024). Uniaxial Tension Test for Fiber-Reinforced Cementitious Composite with Thin Fiber, Japan Society of Civil Engineers 2024 Annual Meeting, V-389.

[4-13] Kanakubo, T. (2006). Tensile characteristics evaluation method for ductile fiber-reinforced cementitious composites. Journal of Advanced Concrete Technology, 4(1), 3-17.

[4-14] Hassan, A. M. T., Jones, S. W., & Mahmud, G. H. (2012). Experimental test methods to determine the uniaxial tensile and compressive behaviour of ultra high performance fibre reinforced concrete (UHPFRC). Construction and building materials, 37, 874-882.

[4-15] Li, L., Zheng, X., Wu, J., Du, X., & Luan, Y. (2024). Comparative study on the dynamic tensile properties of polypropylene and polyethylene fiber reinforced engineered cementitious composites under low to high strain rates. Journal of Building Engineering, 82, 108221.

[4-16] Lu, C., Yu, J., & Leung, C. K. (2016). An improved image processing method for assessing multiple cracking development in strain hardening cementitious composites (SHCC). Cement and Concrete Composites, 74, 191-200.

[4-17] Li, Z., & Leung, C. K. (2022, September). Comparison Between Experimentally Determined and Theoretical Fiber Orientation Distribution in Strain Hardening Cementitious Composites (SHCC). In International Conference on Strain-Hardening Cement-Based Composites (pp. 98-108). Cham: Springer International Publishing.

[4-18] Yokota, H., Rokugo, K., & Sakata, N. (2008, June). JSCE recommendations for design and construction of high performance fiber reinforced cement composite with multiple fine cracks. In High performance fiber reinforced cement composites (Vol. 2, pp. 761-770). Springer Tokyo, Japan.

[4-19] Rokugo, K., Uchida, Y., Moriyama, M., & Lim, S. (2007). Direct tensile behavior and size effect of strain-hardening fiber-reinforced cement-based composites (SHCC). In Proceedings of the 6th International Conference on Fracture Mechanics of Concrete and Concrete Structures, Catania, Italy, Jun (pp. 17-22).

[4-20] Pan, Z., Wu, C., Liu, J., Wang, W., & Liu, J. (2015). Study on mechanical properties of cost-effective polyvinyl alcohol engineered cementitious composites (PVA-ECC). Construction and Building Materials, 78, 397-404.

[4-21] CAI, X. R., & XU, S. L. (2010). Study on corresponding relationships between flexural load-deformation hardening curves and tensile stress-strain hardening curves of UHTCC. Engineering mechanics, 27(1), 8-016.

[4-22] Qian, S., & Li, V. C. (2007). Simplified inverse method for determining the tensile strain capacity of strain hardening cementitious composites. Journal of Advanced Concrete Technology, 5(2), 235-246.

Chapter 5 Evaluation of tensile stress-strain relationship of SHCC

5.1 Introduction

Developing an accurate tensile stress-strain model for SHCC is essential for reliably predicting its deformation capacity and load-carrying behavior. Figure 5-1 illustrates the idealized tensile stress-strain response of SHCC material.

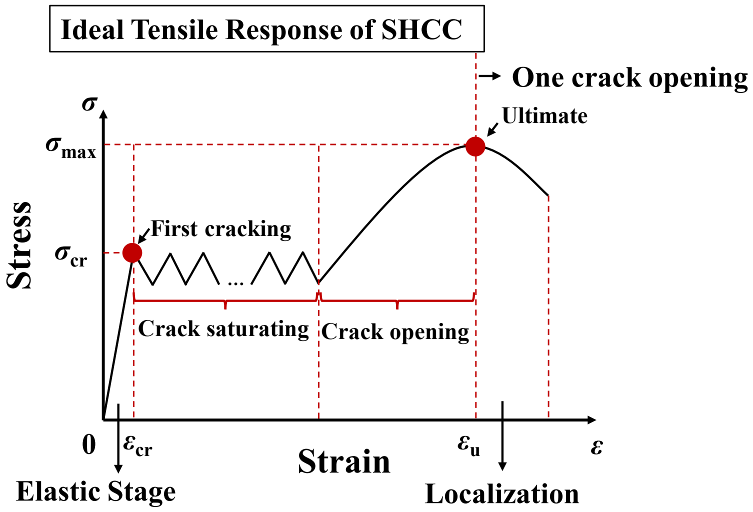

Figure 5-1 Ideal tensile response of SHCC

When the deformation induced by external loading exceeds the elastic capacity of the matrix, the first crack initiates. Immediately after crack formation, the load-carrying capacity decreases, producing a downward drop in the stress–strain curve. Following this drop, the bridging action of fibers transfers tensile force across the crack, leading to a renewed increase in tensile stress with increasing strain. Under idealized conditions, the cracking resistance of the matrix and the bridging performance of the fibers are identical at every cross-section. Consequently, each crack initiates when the bridging stress at the preceding crack reaches the matrix cracking strength, producing a symmetric cycle in which the magnitude of stress decrease equals the stress recovered thereafter. After saturating cracking, stress starts increasing because of the fiber bridging reaches its maximum, i.e., the ultimate stage is reached, one of the cracks begins to localize, its opening width grows continuously, and the stress starts to decrease.

In practice, however, SHCCs do not strictly follow this idealized pattern due to the combined effects of fiber orientation, variability in fiber–matrix interfacial bond, and inherent material heterogeneity. As illustrated in Figure 5-2, during the strain-hardening stage, the stress drop caused by the formation of a new crack may not return to the minimum level of the previous cycle, and the subsequent stress rise may exceed the previous cracking stress. This repeated process continues until the material reaches the ultimate stage. The tensile stress at this stage is defined as the ultimate stress, and the corresponding strain is called the ultimate strain. Beyond this point, the opening of a dominant crack increases without further load enhancement, resulting in localized deformation and final failure.

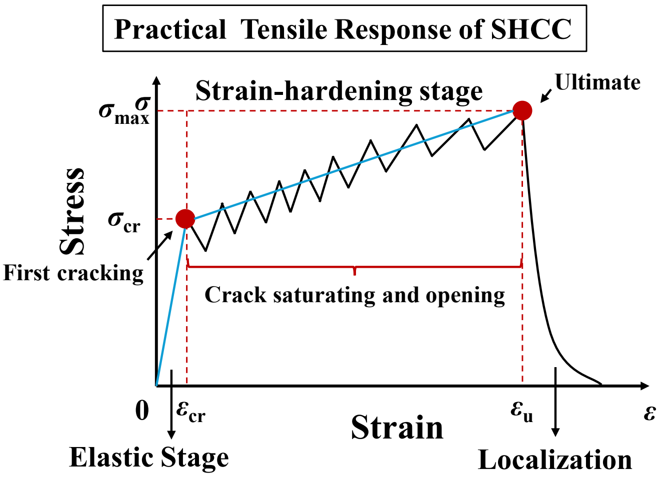

Figure 5-2 Practical tensile response of SHCC

Accordingly, the actual tensile stress–strain behavior of SHCC may be simplified as a two-segment model as the blue line consisting of 1) an initial elastic stage prior to the first cracking and 2) a post-cracking stage extending to the ultimate state. To fully define this simplified model, it is sufficient to determine the stresses and strains corresponding to the cracking and ultimate points for the curve. The cracking stress and cracking strain depend solely on the matrix properties [5-1], while Chapters 2 and Chapter 3 have presented an approach to compute the ultimate stress based on fiber orientation. Thus, the key remaining challenge is to obtain the determination of the ultimate tensile strain.

The ultimate tensile strain can be interpreted as the ratio of the sum of all crack widths to the original specimen length ignoring elastic deformation of the matrix, expressed as Eq. (5-1)

$$\varepsilon_{\mathrm{u}} = \frac{\sum_{i=1}^{n} w_i}{L_{\mathrm{specimen}}} \quad \text{Eq. (5-1)}$$

where L_{specimen} is the specimen length. If the crack spacing is denoted as s_{cr}, then

$$L_{\mathrm{specimen}} = \sum_{i=1}^{n} s_{\mathrm{cr},i} \quad \text{Eq. (5-2)}$$

Assuming that, at the ultimate stage, all crack spacings and associated crack widths are identical, the ultimate strain can be expressed [5-2~5-5] as Eq. (5-3):

$$\varepsilon_{\mathrm{u}} = \frac{w_{\max}}{s_{\mathrm{cr}}} \quad \text{Eq. (5-3)}$$

where, $w_{\max}$ is the maximum crack opening width at the ultimate stage. Therefore, determining the ultimate strain requires the statistical characteristic values of the crack width and crack spacing at the ultimate stage.

In this chapter, a tensile stress-strain model for SHCC incorporating the influence of fiber orientation and PVA fiber dimensions is established. The model is developed based on 1) the bridging laws proposed in Chapters 2 and Chapter 3 including the case of infinite fiber orientation intensity, 2) three basic assumptions to second-order derive the fundamental differential equations governing fiber–matrix bond-slip behavior, and 3) the crack characteristics obtained from the SHCC thin plate specimens using different dimensions of PVA fibers in Chapter 4.

5.2 Theoretical derivation and basic assumptions

In steel-reinforced [5-6~5-8] and FRP-reinforced [5-9,5-10] concrete structures, the bond-slip relationship between reinforcement and concrete, while neglecting the deformation of the concrete matrix and remaining the elastic behavior, can be described by a second-order differential equation of the form shown in Eq. (5-4).

$$\frac{\mathrm{d}^2 s}{\mathrm{d}x^2} = \frac{\phi_\mathrm{s}}{E_\mathrm{s} \cdot A_\mathrm{s}} \cdot \tau_\mathrm{s} \qquad \text{Eq. (5-4)}$$

where,

s, slip of reinforcement

ϕ_s, perimeter of reinforcement

E_s, elastic modulus of reinforcement

A_s, cross-sectional area of reinforcement

τ_s, bond stress between reinforcement and concrete

For SHCC materials, assuming negligible deformation of the cementitious matrix, the relationship between the fiber and the surrounding matrix can be expressed in a similar form as Eq. (5-5) [5-11], based on the force equilibrium and deformation compatibility.

$$\frac{\mathrm{d}^2 s}{\mathrm{d}x^2} = \frac{\phi_\mathrm{f}}{E_\mathrm{f} \cdot A_\mathrm{f}} \cdot \tau_\mathrm{f} \qquad \text{Eq. (5-5)}$$

s, slip of fiber

ϕ_f, perimeter of fiber

E_f, elastic modulus of fiber

A_f, cross-sectional area of fiber

τ_f, bond stress between fiber and cementitious matrix

Once the distribution of interfacial bond stress along the fiber length direction τ_f is prescribed, the slip of the fiber relative to the matrix can be solved accordingly. However, because it is practically difficult to measure the actual bond stress distribution of each single fiber, several assumptions are introduced to enable analytical modeling.

Assumption 1: The increment of pull-out force of the fiber is terminated after the second crack opened across the same single fiber.

Assumption 2: The bond stress distribution stays constant along the direction of effective anchorage length l_e.

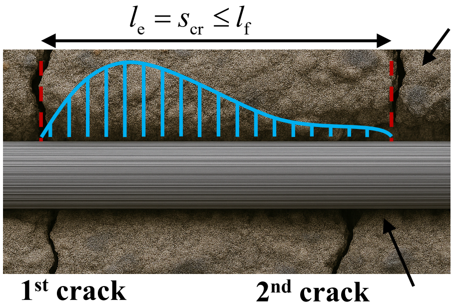

Figure 5-3 Explanation diagram of assumption 1

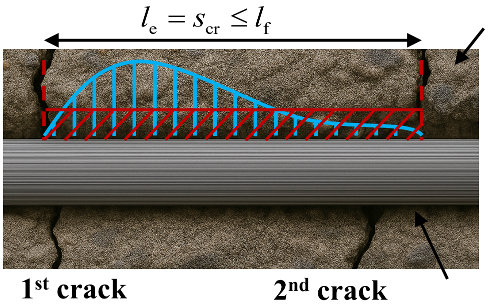

Figure 5-4 Explanation diagram of assumption 2

Regarding **Assumption 1**, as illustrated in Figure 5-3, for a single fiber that may span across multiple cracks, once the first crack forms, fiber bridging occurs, generating interfacial bond stress along the fiber due to the relative slip between the fiber and the matrix. This relative slip consists of the elastic elongation of the fiber and the pull-out displacement at the anchorage end. The macroscopic manifestation of this relative slip is the observable crack width. In this study, the elastic elongation of the fiber is neglected; thus, the pull-out displacement at the crack is directly regarded as the crack width. Just before a second crack forms along the fiber length, **Assumption 1** states that the interfacial bond stress between the fiber and the matrix is maximized under the fiber length segment between the first and the second crack. This length is defined as the effective anchorage length l_e. Consequently, the spacing between the first and second cracks—that is, the crack spacing—is equal to the effective anchorage length, which less than or equal to the fiber length.

As shown in Figure 5-4, **Assumption 2** further states that the interfacial bond stress within the effective anchorage length is constant along the fiber direction to simplify the problem, i.e., $\tau_{\mathrm{f}}=\mathrm{constant}$. Integrating the governing differential equation twice with respect to x gives an expression for the fiber slip as a function of the fiber properties and the constant bond stress as Eq. (5-6). The slip of the fiber at the ultimate stage can then be derived as Eq. (5-7).

$$\iint \frac{\mathrm{d}^2 s}{\mathrm{d}x^2} = \iint \frac{\phi_{\mathrm{f}}}{E_{\mathrm{f}} \cdot A_{\mathrm{f}}} \cdot \tau_{\mathrm{f}}$$

$$\int \frac{\mathrm{d}s}{\mathrm{d}x} = \int \frac{\phi_{\mathrm{f}}}{E_{\mathrm{f}} \cdot A_{\mathrm{f}}} \cdot \tau_{\mathrm{f}} \cdot x$$

$$s = \frac{\phi_{\mathrm{f}}}{E_{\mathrm{f}} \cdot A_{\mathrm{f}}} \cdot \tau_{\mathrm{f}} \cdot \frac{x^2}{2} \qquad \text{Eq. (5-6)}$$

$$s_{\mathrm{u}} = \frac{\phi_{\mathrm{f}}}{E_{\mathrm{f}} \cdot A_{\mathrm{f}}} \cdot \tau_{\mathrm{f}} \cdot \frac{l_e^2}{2} \qquad \text{Eq. (5-7)}$$

The fracture energy G_{fb} associated with interfacial debonding, can be obtained from Eq. (5-8).

$$G_{\mathrm{fb}} = \int_0^{l_e} \tau_{\mathrm{f}} = \tau_{\mathrm{f}} \cdot s_{\mathrm{u}} \qquad \text{Eq. (5-8)}$$

It should be emphasized that the interfacial fracture energy is determined solely by the chemical composition and surface characteristics of the fiber; therefore, for fibers of identical chemical composition, the interfacial fracture energy can be regarded as a constant [5-11].

Accordingly, the effective anchorage length l_{e} can be determined from Eq. (5-9), derived from the relationship between slip of fiber at the ultimate stage s_{u}, fiber mechanical parameters and dimensions, and interfacial fiber fracture energy G_{fb}.

$$l_{\mathrm{e}} = \sqrt{\frac{2s_{\mathrm{u}} \cdot A_{\mathrm{f}} \cdot E_{\mathrm{f}}}{\phi_{\mathrm{f}} \cdot \tau_{\mathrm{f}}} \cdot \frac{s_{\mathrm{u}}}{s_{\mathrm{u}}}} = s_{\mathrm{u}} \sqrt{\frac{2A_{\mathrm{f}} \cdot E_{\mathrm{f}}}{\phi_{\mathrm{f}} \cdot G_{\mathrm{fb}}}} \qquad \text{Eq. (5-9)}$$

Reference [8] addressing the theoretical bond behavior of reinforced concrete members established the fundamental bond-equilibrium condition based on the relationship between bond strength and bond fracture energy, thereby determining the maximum pull-out load. Building upon this framework, reference [5-11] extended the same concept to the theoretical local bond behavior between fibers and matrix in FRCC materials. By applying the basic bond–slip differential equation together with the physical and mechanical parameters of the fibers, it was concluded that the crack width is proportional to the square root of the fiber diameter, as expressed in Eq. (5-10).

$$w_{\max} \propto \sqrt{d_{\mathrm{f}}} \qquad \text{Eq. (5-10)}$$

Inspired by this result, it can be inferred that the maximum pull-out displacement of fibers at the ultimate stage should also be related to the geometric parameters of the fibers. Accordingly, the following assumption is introduced,

Assumption 3: The slip at ultimate stage of fiber is proportional to the square root of the fiber diameter.

$$s_{\mathrm{u}} \propto \sqrt{d_{\mathrm{f}}} \qquad \text{Eq. (5-11)}$$

That is,

$$s_{\mathrm{u}} = k\sqrt{d_{\mathrm{f}}} \qquad \text{Eq. (5-12)}$$

where *k* denotes a proportionality constant.

Based on this assumption, an expression relating crack spacing to the effective anchorage length can be derived as Eq. (5-13):

$$s_{\mathrm{cr}} = l_{\mathrm{e}} = \sqrt{\frac{2A_{\mathrm{f}} \cdot E_{\mathrm{f}}}{\phi_{\mathrm{f}} \cdot G_{\mathrm{fb}}}} \cdot k\sqrt{d_{\mathrm{f}}} = \mathrm{K}\sqrt{d_{\mathrm{f}}}$$ Eq. (5-13)

$$\mathrm{K} = \frac{s_{\mathrm{cr}}}{\sqrt{d_{\mathrm{f}}}} = k \cdot \sqrt{\frac{2A_{\mathrm{f}} \cdot E_{\mathrm{f}}}{\phi_{\mathrm{f}} \cdot G_{\mathrm{fb}}}}$$ Eq. (5-14)

where K denotes a proportionality constant representing the fiber mechanical properties and dimensions.

5.3 Tensile stress-strain relationship based on fiber orientation and dimensions

Using the mean values obtained from the statistical distributions of crack characteristics in Chapter 4 as listed again in Table 5-1, the relationship between crack spacing and fiber diameter is shown in Figure 5-5. The fitting result is given by Eq. (5-16).

$$s_{\mathrm{cr}} = 35.7\sqrt{d_{\mathrm{f}}}$$ Eq. (5-15)

This result indicates that, at the ultimate stage, the crack spacing is 35.7 times the square root of the fiber diameter. In this analysis, the mean values of the statistical distributions at the ultimate stage were adopted because they represent the overall average behavior. Considering the relatively large standard deviations, using extreme values may lead to overly conservative or excessively optimistic estimates of the ultimate strain. Taking into account the available PVA fiber products supplied by Kuraray Co., Ltd., this study additionally calculates three other PVA fiber types with relatively larger dimensions as supplementary cases. The parameters used in the calculations are listed in Table 5-2. Table 5-3 presents the computed tensile stress-strain responses for different fiber types based on the proposed model. Figure 5-6 presents the tensile stress-strain relationships of the SHCC materials reinforced with different fiber dimensions based on the proposed model.

Table 5-1 Statistical results of the crack characteristics

Fiber type	Avg. $w_{\max}$ (mm)	SD. $w_{\max}$ (mm)	Avg. s_{cr} (mm)	SD. s_{cr} (mm)
PVA027-06	0.19	0.23	6.28	5.98
PVA040-12	0.19	0.11	7.07	6.42
PVA100-12	0.37	0.12	11.13	4.61

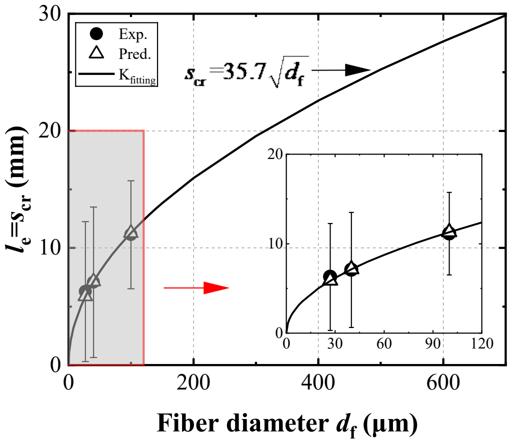

Figure 5-5 Fitting results of s_{cr} and d_f

Table 5-2 Calculate parameters

Fiber type	d_f (μm)	L_f (mm)	E_f (GPa)	A_f (mm^2)	ϕ_f (mm)	G_{fb} (N/mm)	s_{cr} (mm)
PVA027-06	27	6	28	0.00057	0.085	0.0651	6.28
PVA040-12	40	12	41	0.00126	0.126		7.07
PVA100-12	100	12	46	0.00785	0.314		11.13
PVA200-12	200	12	30	0.03142	0.628		14.87
PVA200-18	200	18	27	0.03142	0.628		14.87
PVA660-30	660	30	23	0.34212	2.073		27.01

Table 5-3 Stress and strain value at cracking and ultimate stage (k = infinity)

Fiber type	σ_{cr} (MPa)	ε_{cr} (%)	$\sigma_{\max}$ (GPa)	$w_{\max}$ (mm)	s_{cr} (mm)	ε_u (%)
PVA027-06	3.00	0.02	17.47	0.23	5.87	4.0
PVA040-12	2.52		14.32	0.28	7.14	
PVA100-12	4.22		11.46	0.45	11.29	
PVA200-12	3.16		8.40	0.64	15.97	
PVA200-18	3.26		7.93	0.64	15.97	
PVA660-30	3.28		4.04	1.16	29.00	

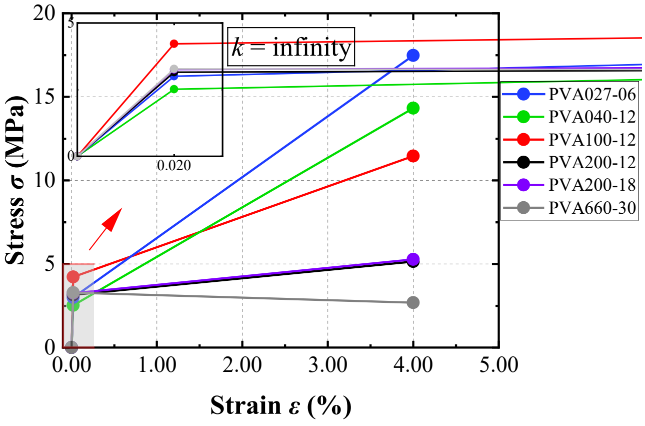

Figure 5-6 Stress-strain relationship using different dimensions PVA fibers (k = infinity)

In these calculations, the maximum crack width was determined using the model proposed in [5-11], the cracking strain of matrix was taken as 0.02%, and the cracking stress was evaluated as the product of the matrix elastic modulus and the cracking strain. The elastic modulus was taken from the experimental results reported in Table 4-3, others were taken from [5-11]. The ultimate tensile stress was obtained using the fiber-orientation-based model derived in Chapter 3. Except for the PVA100-12 series, which had a fiber volume fraction of 3%, all other fiber series are adopted by a 2% volume fraction.

For the case of infinitely large fiber orientation intensity, all fiber series except PVA660-30 exhibited strain-hardening behavior after matrix cracking, characterized by an increase in tensile stress with increasing strain. In this case, the specimens made by PVA660-30 would not meet the requirement of the SHCC definition. At the ultimate stage, the PVA027-06 series exhibited the largest value of ultimate stress, which show a tendency that decreased progressively with increasing fiber diameter. For the PVA200-12 and PVA200-18 series, the ultimate tensile stress was only slightly larger than the cracking stress. This may suggest two possible behaviors in actual specimens or structural members, where fiber orientation cannot be regard as perfectly aligned in one direction and is never truly infinite: 1) the specimen may form only one crack, and the continuous widening of this crack eventually leads to failure; or 2) limited multiple cracking may occur after the first crack, similar to SHCC materials, but due to insufficient fiber volume fraction, unfavorable fiber dimensions, inadequate interfacial bond strength, or high matrix strength, the material soon transitions into global softening dominated by the widening of a major crack. Across all fiber series, the ultimate tensile strain predicted by the proposed model was consistently 4.0%, indicating that, under the assumptions introduced, variations in fiber dimensions do not alter the ultimate tensile strain of SHCC. This conclusion is consistent with the ultimate tensile strain of 2% volume fraction reported by Zhang and Yang [5-12], where a bilinear constitutive model based on the PVA fiber volume fraction and empirical parameters predicted a similar ultimate strain for PVA-SHCC.

In addition, the ultimate tensile stresses and ultimate strains were calculated for a fiber orientation intensity $k = 1$, corresponding to a fully random fiber orientation. The results are shown in Table 5-4 and Figure 5-7. As seen in these results, the cracking stress and cracking strain, being determined solely by the matrix properties, are identical to those obtained for infinite fiber orientation. During the strain-hardening stage, similar to the infinite orientation intensity case, the PVA027-06, PVA040-12, and PVA100-12 series exhibited strain-hardening behavior with an increase in stress corresponding to increasing strain, and their ultimate strain remained 4.0%. In contrast, the PVA200-12, PVA200-18, and PVA660-30 series displayed strain-softening behavior.

Table 5-4 Stress and strain value at cracking and ultimate stage ($k = 1$)

Fiber type	σ_{cr} (MPa)	ε_{cr} (%)	σ_{max} (GPa)	w_{max} (mm)	s_{cr} (mm)	ε_u (%)
PVA027-06	3.00	0.02	12.07	0.23	5.87	4.0
PVA040-12	2.52		8.92	0.28	7.14	
PVA100-12	4.22		6.06	0.45	11.19	
PVA200-12	3.16		0.20	0.64	15.97	
PVA200-18	3.26		0	0.64	15.97	3.9
PVA660-30	3.28		0	1.16	29.00	2.2

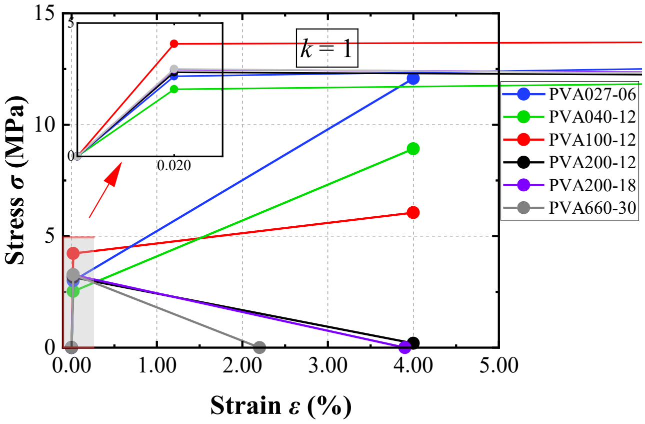

Figure 5-7 Stress-strain relationship using different dimensions PVA fibers ($k = 1$)

To validate the applicability of the proposed model, experiment results from UTTs on SHCC specimens were collected from publicly available literature, as summarized in Table 5-5. The ratio between the experiment values of ultimate strain and predicted by the proposed model were then calculated and plotted in Fig. 5-8. As shown in Fig. 5-8, the majority of the obtained ultimate strain ratios are concentrated around 1.0, indicating that the proposed model is capable of reasonably predicting the ultimate tensile strain of SHCC.

Table 5-5 Experiment results collected from references

Ref.	σ_u (MPa)	ε_u	B/W	f_c (MPa)	Fiber			
					Type	Diameter (μm)	Length (mm)	Volume fraction
[5-13]	5.4	4.5	0.20	55.6	PVA	39	12	2%
	3.3	2.2	0.30	23.3				
	2.6	4.2	0.35	14.2				
[5-14]	4.7	3.5(avg.)	0.20	-	PVA	39	12	2%
[5-15]	4.4	4.0	0.28	-	PVA	39	12	2%
[5-16]	3.7	4.4(avg.)	0.28	34.4	PVA	40	12	2%

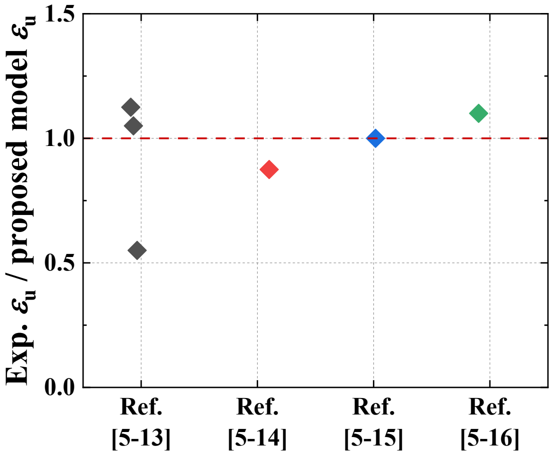

Fig. 5-8 The ratio of experiment ε_u collected from references and predicted value by proposed model

5.4 Summary

In this chapter, three fundamental assumptions were introduced based on the second-order differential equation governing fiber–matrix bond-slip behavior, leading to a theoretical derivation of the ultimate tensile strain of SHCC reinforced with PVA fibers. Using the statistical distributions of crack characteristics obtained from the bending tests in Chapter 4, the relationship between crack spacing and fiber diameter was fitted, enabling the determination of the ultimate tensile strain for SHCC incorporating fibers of different sizes. Combined with the ultimate tensile stress model derived in Chapters 2 and 3 considering fiber orientation, the complete tensile stress–strain relationships of SHCC were constructed for both infinite fiber-orientation intensity and fully random fiber orientation (fiber orientation intensity = 1). Under the introduced assumptions and based on the bond-slip differential formulation, the ultimate tensile strain for SHCC reinforced with different PVA fiber dimensions was determined to be consistently 4.0%.

Reference

[5-1] Leung, C. K., & Li, V. C. (1989, January). First-Cracking Strength of Short Fiber-Reinforced Ceramics. In A Collection of Papers Presented at the 13th Annual Conference on Composites and Advanced Ceramic Materials: Ceramic Engineering and Science Proceedings (pp. 1164-1178). Hoboken, NJ, USA: John Wiley & Sons, Inc.

[5-2] Marshall, D. B., & Cox, B. N. (1988). A J-integral method for calculating steady-state matrix cracking stresses in composites. Mechanics of materials, 7(2), 127-133.

[5-3] Li, V. C., & Wu, H. C. (1992). Conditions for pseudo strain-hardening in fiber reinforced brittle matrix composites. Applied Mechanics Reviews, 45(8), 390-398.

[5-4] Yang, E. H., Wang, S., Yang, Y., & Li, V. C. (2008). Fiber-bridging constitutive law of engineered cementitious composites. Journal of advanced concrete technology, 6(1), 181-193.

[5-5] Lin, Z., & Li, V. C. (1997). Crack bridging in fiber reinforced cementitious composites with slip-hardening interfaces. Journal of the Mechanics and Physics of Solids, 45(5), 763-787.

[5-6] Muguruma, H., Morita, S., & Tomita, K. (1967). Fundamental study on bond between steel and concrete. Transaction of Architectural Institute of Japan, 131, 1-6.

[5-7] Yasojima, A., Kanakubo, T. (2003). Study on bond splitting behavior of reinforced concrete members : Part 3 Predicting equation for bond splitting strength without lateral reinforcement. Journal of Structural and Construction Engineering (Transactions of AIJ) 68(567):117-123.

[5-8] Asano, K., Yasojima, A., & Kanakubo, T. (2008). Study on bond splitting behavior of reinforced concrete members. Part 6 Theoretical solution by the parabolic model of bond constitutive law. J. Struct. Constr. Eng. AIJ, 73, 641-646.

[5-9] Sakai, T., Kanakubo, T., Yonemaru, K., & Fukuyama, H. (1999). Bond splitting behavior of continuous fiber reinforced concrete members. Special Publication, 188, 1131-1144.

[5-10] Kanakubo, T., Wu, Z. S., & Ueda, T. (2005, March). Influence of local bond characteristics in FRP-concrete bond behavior. In 11th International Conference on Fracture, Turin (Italy), March (pp. 20-25).

[5-11] Shiferaw, H. N., Abrha, S. F., Kanakubo, T., Sivasubramanian, M. V., & Singh, S. B. (2024). Influence of fiber dimensions on bridging performance of polyvinyl alcohol fiber-reinforced cementitious composite (PVA-FRCC). Fibers, 12(8), 70.

[5-12] Zhang, C., & Yang, X. (2019). Bilinear elastoplastic constitutive model with polyvinyl alcohol content for strain-hardening cementitious composite. Construction and Building Materials, 209, 388-394.

[5-13] Yu, J., & Leung, C. K. (2014). Strength improvement of SHCC with ultra-high volumes of fly ash. In Proceedings, 3rd International RILEM Conference on Strain Hardening Cementitious Composites, Delft, The Netherlands (pp. 97-104).

[5-14] Lu, C., & Leung, C. K. (2016). A new model for the cracking process and tensile ductility of strain hardening cementitious composites (SHCC). Cement and Concrete Research, 79, 353-365.

[5-15] Li, J., Weng, J., Chen, Z., & Yang, E. H. (2021). A generic model to determine crack spacing of short and randomly oriented polymeric fiber-reinforced strain-hardening cementitious composites (SHCC). Cement and Concrete Composites, 118, 103919.

[5-16] Rokugo, K., Uchida, Y., Moriyama, M., & Lim, S. (2007). Direct tensile behavior and size effect of strain-hardening fiber-reinforced cement-based composites (SHCC). In Proceedings of the 6th International Conference on Fracture Mechanics of Concrete and

Concrete Structures, Catania, Italy, Jun (pp. 17-22).

Chapter 6 Conclusion and prospects

6.1 Conclusion

This study conducted a comprehensive investigation into the mechanisms governing fiber orientation, crack development, and tensile stress transfer in strain-hardening cementitious composites (SHCCs). By integrating visualization-based fiber orientation analysis, flexural testing of thin plate specimens, image-based crack characterization, and analytical modeling grounded in bond mechanics, a generalized tensile stress–strain constitutive model was established. The major conclusions drawn from this research are summarized as follows.

(1) Influence of placing thickness on fiber orientation and bridging performance

A visualization simulation using nylon fibers and water glass demonstrated that the placing thickness exerts a decisive influence on fiber dispersion and orientation. A smaller placing thickness promotes strong two-dimensional fiber alignment, resulting in enhanced fiber orientation intensity. Image-based quantification confirmed that higher orientation intensity leads to a more favorable bridging stress distribution. The corresponding bridging law calculations revealed that reduced placing thickness improves the peak bridging stress and overall fiber efficiency. Sectional moment–curvature analyses further validated that enhanced fiber orientation effectively improves flexural performance, even without increasing fiber volume fraction.

(2) Flexural behavior of functionally layered FRCC

The functionally layered FRCC (FL-FRCC), fabricated by stacking multiple thin layers with thicknesses smaller than the fiber length, successfully induced a pronounced two-dimensional fiber alignment. Four-point bending tests demonstrated that FL-FRCC exhibits nearly double the maximum bending capacity of homogeneous FRCC while preserving superior ductility and energy absorption. The analytical tensile model incorporating the modified bridging law gives a good prediction of the maximum bending moment.

(3) Statistical distribution of crack characteristics of SHCC thin plates

Four-point bending tests conducted on thin SHCC plates reinforced with PVA fibers of different dimensions to obtain crack characteristics data. Image-processing-based crack detection showed that all tested SHCC plates exhibited multiple fine cracks, with most crack widths below 0.5 mm. Specimens adopting smaller-diameter fibers (27 μm and 40 μm, $V_f = 2\%$) demonstrated more cracks and smaller crack spacing than the larger-diameter fibers (100 μm, $V_f = 3\%$). Statistical fitting using both normal and log-normal distributions revealed that the log-normal function provides a superior fit for crack width and crack spacing distributions, as supported by Kolmogorov–Smirnov tests. These statistical results provide essential input parameters for the tensile stress-strain modeling developed in Chapter 5.

(4) Analytical modeling of tensile stress–strain behavior of SHCC

A tensile stress-strain model was developed by integrating fiber orientation effects, fiber dimensional characteristics, and crack characteristic statistics. Starting from the differential equations governing fiber–matrix bond slip, theoretical relationships were derived among effective anchorage length, crack spacing, and fiber slip at the ultimate stage. The model relied on three physically motivated assumptions:

1) The increment of pull-out force is terminated after the second crack opened across single fiber;
2) The bond stress distribution stays constant along the direction of effective anchorage length;
3) The slip at ultimate stage of fiber is proportional to the square root of the fiber diameter.

Fitting these relationships to experimental crack data enabled the prediction of crack spacing for fibers of other dimension types. The model estimated that, under infinitely large fiber orientation intensity, the ultimate tensile strain of SHCC approaches approximately 4.0%, regardless of fiber diameter.

Collectively, the results of this research provide a deeper mechanistic understanding of how fiber orientation, fiber dimensions, and interfacial bond characteristics jointly govern the cracking behavior and tensile response of SHCC. The generalized constitutive model proposed herein offers enhanced predictive capability and contributes a more reliable analytical tool for the design, optimization, and structural application of high-performance SHCC materials.

6.2 Prospects for Future Research

Although this study advances the modeling and understanding of SHCC behavior, several areas deserve further investigation:

(1) Establishment of standardized uniaxial tension test methods and conversion frameworks with flexural tests

Given the current lack of a unified standard for uniaxial tension test, this study employed flexural testing to evaluate crack characteristics and related parameters after considering the practical challenges associated with uniaxial tension experiments. Nevertheless, discrepancies between flexural and uniaxial tension responses are inevitable. From the perspective of experimental feasibility and broader applicability, future research should aim to develop standardized procedures for uniaxial tension test as well as systematic conversion frameworks that enable reliable correlation between flexural test results and true uniaxial tensile behavior.

(2) Influence on matrix strength

In SHCCs, the matrix strength governs the first-cracking stress and the energy balance between matrix cracking and fiber bridging. Future studies should systematically vary the matrix compressive and tensile strength while keeping fiber parameters constant, in order to derive a quantitative correlation between matrix strength and σ–ε response.

(3) Situation of $l_e > l_f$

It should be noted that the present study is limited to cases where the effective anchorage length l_e is shorter than the fiber length l_f. Future work is therefore required to examine conditions in which the effective anchorage length becomes larger than the fiber length through comprehensive experimental and theoretical investigations.

Acknowledgment

I would like to give my superior gratitude to my academic supervisor, Professor Kanakubo Toshiyuki. Over the past four and a half years, Professor Kanakubo Toshiyuki has provided invaluable guidance to my research through his extensive experimental expertise and forward-looking academic vision. What impressed me most was his thorough involvement in every stage of the research process—from the planning of experimental programs, the fabrication of molds, to specimen preparation and testing—always offering detailed and patient guidance. At the same time, he respected and carefully considered our own ideas regarding experimental approaches, encouraging independent thinking toward experimental observations and results. When I made mistakes due to a lack of comprehensive planning, he patiently explained the issues and devoted considerable effort to improving the experimental procedures. During times when I encountered unavoidable personal difficulties, he showed understanding and offered support whenever possible. Throughout my years of study in Japan, Professor Kanakubo Toshiyuki has been the Japanese scholar with whom I communicated most frequently; his unique creativity provided me with constant inspiration, and our daily conversations allowed me to gain a deeper appreciation of Japanese culture. Above all, what I admire most is his unwavering passion and boundless energy toward research and work. My only regret is that I may not have fully met his expectations.

I would like to express my sincere gratitude to my vice-supervisors, Professor Matsushima and Professor Yasojima, for their continuous support of my research, their assistance in experimental work, and their many constructive comments and insightful suggestions on this dissertation. Through their guidance, I was also given valuable opportunities to engage in academic exchanges with researchers from different countries, whose enthusiasm for research has greatly motivated my academic journey.

I am also deeply grateful to Professor Shoji and Professor Tajima, members of my dissertation examination committee, for their valuable comments and suggestions, which provided important direction for improving my research.

My heartfelt thanks go to all former and current members of the Kanakubo Laboratory for creating a friendly and mutually supportive research environment. I would like to especially thank Kobayashi Hiroya, Li Sicong, Ms. Selamawit Fthanegest Abrha, Ms. Helen Negash Shiferaw, Tian Weichao, Biao Qian, Sasaki Hideto, Li Keyi, Nitta Martha, and Maruko Haruki for their assistance during the experiments. I am also grateful to Dr. Amadou Sakhir Syll, doctoral student Helen Negash Shiferaw, and Dong Tianwen for their mutual encouragement and companionship throughout this academic journey. I would like to extend my deepest respect and gratitude to the late technical staff member Mr. Kojima, who sadly passed away due to illness and who had generously supported my experiments.

I am profoundly thankful to my family for their unwavering support throughout my studies. In particular, I would like to thank my mother, who supported my decision to study abroad from the very beginning and provided unconditional encouragement throughout these years.

I would also like to thank the members of the University of Tsukuba Badminton Doukoukai, who allowed me to enjoy badminton alongside my research life and provided opportunities to interact with undergraduate and master’s students from various academic fields.

My sincere appreciation goes to the governments of China and Japan for their financial support, which enabled me to complete my doctoral studies and to experience the academic cultures and living environments of both countries. I am also grateful to the teachers of the NENU Preparatory School for Chinese Students to Japan for their Japanese language training prior to my departure, and for giving me the opportunity to meet many outstanding doctoral students of the MEXT program. Although the time spent there lasted only ten months, it remains one of the most unforgettable and joyful periods of my twenties.

I would like to thank Professor Yang Lufeng and Professor Chen Zheng of Guangxi University for their support in helping me pursue my studies abroad.

Thanks to myself.

Looking back on these four and a half years, I experienced the global outbreak of COVID-19 and witnessed numerous world changes closely related to everyday life like AI development. Living abroad exposed me to diverse streams of information, both genuine and misleading, which broadened my perspective. I am deeply grateful for the education I have received, which has guided me to make rational judgments based on facts.

May peace prevail in the world.

Publications arising from the thesis

Reviewed paper

1) Zhang, H., & Kanakubo, T. (2023). Flexural Characteristics of Functionally Layered Fiber-Reinforced Cementitious Composite with Polyvinyl Alcohol Fibers. Journal of Composites Science, 7(7), 293.
2) Zhang, H., & Kanakubo, T. (2022, September). Influence of Placing Thickness on Fiber Orientation and Bridging Law of FRCC. In International Conference on Strain-Hardening Cement-Based Composites (pp. 91-97). Cham: Springer International Publishing.

Proceeding

1) Hang Zhang, Toshiyuki Kanakubo: Bending Test of Polyvinyl Alcohol Fiber-Reinforced Cementitious Composite Plates, Japan Society of Civil Engineers 2025 Annual Meeting, 12PM2-Oe-04, 2025.9
2) Kanakubo Toshiyuki, Li Sicong, Zhang Hang: Tensile Characteristics of Fiber-Reinforced Cementitious Composite with Recycled Carbon Fiber, Japan Society of Civil Engineers 2024 Annual Meeting, V-380, 2024.9
3) 朴謙, 張航, 金久保利之: アラミド繊維補強セメント複合材料の引張試験と架橋則の検討, 土木学会年次学術講演会講演概要集, 部門 V-383, 2024.9
4) Tian Weichao, Zhang Hang, Kanakubo, Toshiyuki: Uniaxial Tension Test for Fiber-Reinforced Cementitious Composite with Thin Fiber, Japan Society of Civil Engineers 2024 Annual Meeting, V-389, 2024.9